

# **DESIGN AND NUMERICAL SIMULATION OF HYBRID-SYSTEM OF BEARINGS**

**Thesis submitted by**

**MINTU KARMAKAR**

**Doctor of Philosophy (Engineering)**

**Department of Mechanical Engineering,  
Faculty Council of Engineering & Technology  
Jadavpur University  
Kolkata, India**

**2024**



**1. Title of the Thesis:**

**DESIGN AND NUMERICAL SIMULATION OF HYBRID-SYSTEM OF BEARINGS**

**2. Name, Designation and Institution of the Supervisors:**

**Dr. SUSENJIT SARKAR**

Professor,  
Department of Mechanical  
Engineering, Jadavpur  
University, Kolkata – 700032,  
India.

**Dr. SAMAR CHANDRA MONDAL**

Professor,  
Department of Mechanical  
Engineering, Jadavpur  
University, Kolkata – 700032,  
India

**3. List of Publications:**

- I. M. Karmakar and S. Sarkar, "Non-dimensional analysis of axially polarized passive magnetic bearings," SN Appl. Sci., vol. 2, p. 987, 2020.  
<http://dx.doi.org/10.1007/s42452-020-2809-x>.
- II. M. Karmakar and S. Sarkar, "Semi-Analytical Finite Element Approach for 6-DOF Characterizations of PMB Load," in IEEE Transactions on Magnetics, vol. 58, no. 7, pp. 1-10, July 2022, Art no. 8001510.  
<http://dx.doi.org/10.1109/tmag.2022.3174449>.



**4. List of Patents:** Nil

**5. List of Presentations in National / International / Conferences / Workshops:**

- I. M. Karmakar, S. Tudu, S. Sarkar, and S. C. Mondal, "Comparison of errors in calculating the journal force of a short cylindrical oil film bearing," presented at the 1st International Conference on Contemporary Issues in Computing, July 25, 2020. <http://dx.doi.org/10.26480/cic.01.2020.59.63>.



## Statement of originality

I, **MINTU KARMAKAR** registered on **May 08, 2018** with registration number **1021811023**, do hereby declare that this thesis entitled **“DESIGN AND NUMERICAL SIMULATION OF HYBRID-SYSTEM OF BEARINGS”** contains literature survey and original research work done by the undersigned candidate as part of Doctoral studies.

All information in this thesis have been obtained and presented in accordance with existing academic rules and ethical conduct. I declare that, as required by these rules and conduct, I have fully cited and referred all materials and results that are not original to this work.

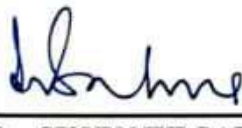
I also declare that I have checked this thesis as per the “Policy on Anti Plagiarism, Jadavpur University, 2024”, and the level of similarity as checked by iThenticate software is 4%.

*Mintu Karmakar*

**Signature of MINTU KARMAKAR:**

**Date:** 19.03.2024

**Certified by Supervisors:**

 19/03/24

**Dr. SUSENJIT SARKAR**

Professor,

Department of Mechanical

Engineering, Jadavpur

University, Kolkata – 700032,

India.

*Professor*

*Dept. of Mechanical Engineering  
Jadavpur University, Kolkata-32*

 19/03/24

**Dr. SAMAR CHANDRA MONDAL**

Professor,

Department of Mechanical

Engineering, Jadavpur

University, Kolkata – 700032,

India.

*Professor*

*Dept. of Mechanical Engineering  
Jadavpur University, Kolkata-32*






## Certificate from the supervisors

This is to certify that the thesis entitled “**DESIGN AND NUMERICAL SIMULATION OF HYBRID-SYSTEM OF BEARINGS**” submitted by **Shri Mintu Karmakar**, who got his name registered on **May 08, 2018** with registration number 1021811023 for the award of Ph. D. (Engineering) degree of Jadavpur University is absolutely based upon his own work under the supervision of Prof. & **Dr. Susenjit Sarkar** and Prof. & **Dr. Samar Chandra Mondal** and that neither his thesis nor any part of the thesis has been submitted for any degree / diploma or any other academic award anywhere before.


### THESIS SUPERVISORS

 19/03/2024.

**Dr. SUSENJIT SARKAR**

Professor,  
Department of Mechanical  
Engineering, Jadavpur  
University, Kolkata – 700032,  
India.

*Professor*  
*Dept. of Mechanical Engineering*  
*Jadavpur University, Kolkata-32*

 19/03/24

**Dr. SAMAR CHANDRA MONDAL**

Professor,  
Department of Mechanical  
Engineering, Jadavpur  
University, Kolkata – 700032,  
India.

*Professor*  
*Dept. of Mechanical Engineering*  
*Jadavpur University, Kolkata-32*



## Acknowledgments

I would like to express my deepest gratitude to my thesis guides, Professor & Dr. Susenit Sarkar and Professor & Dr. Samar Chandra Mondal, for his unwavering support and guidance throughout my research journey. His expertise, patience, and encouragement were instrumental in helping me to overcome challenges and achieve my goals.

I am also grateful to the members of my Research Advisory Committee (RAC), Professor Amit Karmakar, Head and Chairman of RAC, Professor Gautam Majumdar, earlier Head and Chairman of RAC, Professor Sumanta Neogy, Mech. Engg. JU, and Professor Arghya Nandi, Mech. Engg. JU, for their valuable insights and feedback. Their guidance helped me to refine my research questions, methodology, and findings.

I would like to thank the staffs of the Mechanical Department and Faculty Council of Engineering & Technology for their assistance and support throughout my studies.

I am also grateful to my family for their unwavering support and encouragement throughout my studies

*I would like to dedicate this thesis to:*

My family for loving and supporting me

*Mintu Karmakar*  
19.03.2024  
**Mintu Karmakar**



# Table of Contents

<b>Thesis Information</b>	I
<b>Statement of originality</b>	III
<b>Certificate from the supervisors</b>	IV
<b>Acknowledgments</b>	V
<b>Table of Contents</b>	VI
<b>Preface</b>	VIII
<b>List of Abbreviations</b>	IX
<b>Nomenclature</b>	X
<b>List of figures</b>	XII
<b>List of tables</b>	XVI
<b>1. Introduction</b>	<b>1</b>
1.1 Research motivations	1
1.2 Thesis outline	1
<b>2. Literature review</b>	<b>3</b>
2.1 Oil film bearing simulation methods	3
2.2 Permanent magnet bearing and simulation	6
2.3 Hybridization of permanent magnet bearing and oil film bearing	8
2.4 Summary	9
<b>3. Solver study and methods</b>	<b>10</b>
3.1 Introduction	10
3.2 Journal force expression from Reynold's equation	11
3.3 FDM approach	12
3.4 FEM approach	14
3.5 Input parameters	15
3.6 Results and statistical analysis	15
3.7 Summary	21
<b>4. Stiffness study of journal bearing using FEM approach</b>	<b>22</b>
4.1 Introduction	22
4.2 Details of the proposed method	22



4.3	Validation of some stiffness parameters of journal bearing	24
4.4	Results of proposed method	27
4.5	Summary	31
<b>5.</b>	<b>Non dimensional numerical study of 3-DOF PMBs</b>	<b>32</b>
5.1	Introduction	32
5.2	Configuration details for the proposed model	33
5.3	Validation of the proposed model	42
5.4	Simulation of non-dimensional proposed model	46
5.5	Summary	51
<b>6.</b>	<b>Semi-analytical FEM approach for studying 6-DOF PMB</b>	<b>53</b>
6.1	Introduction	53
6.2	Details of the proposed model	53
6.3	Sensitivity analysis of error and computational time on mesh density	61
6.4	Validation of the proposed model	62
6.5	Simulation results for magnetic moment and stiffness characteristics using proposed method	66
6.6	Summary	71
<b>7.</b>	<b>Numerical study of hybrid-system of bearings</b>	<b>72</b>
7.1	Introduction	72
7.2	Details of the proposed model	72
7.3	Validation of model for static load	85
7.4	Comparison results and characteristics study of hybrid system of bearings	86
7.5	Summary	99
<b>8.</b>	<b>End conclusion and future scope of work</b>	<b>100</b>
8.1	Conclusions	100
8.2	Suggestions for potential future work	100
	<b>References</b>	<b>102</b>
	<b>AppendixA</b>	<b>111</b>
A.1	Bearing force derivation	111
A.2	Sommerfeld number relationship with journal bearing force	111





# **Preface**

This thesis addresses the critical challenge of enhancing the bearing study of a shaft-disc system. To achieve this, a comprehensive theoretical investigation of both oil film and permanent magnet bearings is undertaken. This research introduces a novel semi-analytical FEM approach for simultaneously identifying stiffness properties and other characterizations of these bearings. Furthermore, the research delves into exploring the mixed behavior of both systems by analyzing their interaction within a hybrid system configuration of permanent magnet and oil film bearings. This in-depth exploration provides valuable insights for designers.



## **List of Abbreviations**

FEM	Finite Element Method
CFD	Computational Fluid Dynamics
FDM	Finite Difference Method
PDE	Partial Differential Equation
PMB	Passive Magnet Bearing
AMB	Active Magnet Bearing
DOF	Degree of Freedom
ANOVA	Analysis of Variance
RMS	Root Mean Square
3D	Three-Dimensional
2D	Two-Dimensional



# Nomenclature

$F_{sr}$ : Magnetic force between stator and rotor (N);  
 $\mu_0$ : Absolute permeability ( $4\pi \times 10^{-7} \frac{N}{A^2}$  or  $\frac{H}{m}$  or  $\frac{Tm}{A}$ );  
 $q_s$ : Magnetic pole strength of stator magnet (Wb or Am);  
 $q_r$ : Magnetic pole strength of rotor magnet (Wb or Am);  
 $r_{sr}$ : Distance between stator and rotor magnetic pole (m);  
 $\sigma_s$ : Stator magnetic surface charge density (T);  
 $\sigma_r$ : Rotor magnetic surface charge density (T);  
 $S_s$ : Stator magnetic pole surface area per pole ( $m^2$ );  
 $S_r$ : Rotor magnetic pole surface area per pole ( $m^2$ );  
 $Br_1$ : Residual magnetism of rotor magnetic material (T);  
 $Br_2$ : Residual magnetism of stator magnetic material (T);  
 $r_1$ : Radial distance of rotor small elemental area  $dS_r$  from rotor axis (m);  
 $r_2$ : Radial distance of stator small elemental area  $dS_s$  from stator axis (m);  
 $x$ : Radial displacement of rotor centroid from stator centroid (global origin) along x axis (m);  
 $y$ : Radial displacement of rotor centroid from stator centroid (global origin) along y axis (m);  
 $z$ : Axial displacement of rotor centroid from stator centroid (global origin) along z axis (m);  
 $u$ : Radial displacement of rotor small elemental area  $dS_r$  from stator small elemental area  $dS_s$  along x axis (m);  
 $v$ : Radial displacement of rotor small elemental area  $dS_r$  from stator small elemental area  $dS_s$  along y axis (m);  
 $z_1$ : Displacement of small elemental area  $dS_r$  of rotor's South Pole from small elemental area  $dS_s$  of stator's North Pole along z axis (m);  
 $z_2$ : Displacement of small elemental area  $dS_r$  of rotor's North Pole from small elemental area  $dS_s$  of stator's South Pole along z axis (m);  
 $z_3$ : Displacement of small elemental area  $dS_r$  of rotor's North Pole from small elemental area  $dS_s$  of stator's North Pole along z axis (m);  
 $z_4$ : Displacement of small elemental area  $dS_r$  of rotor's South Pole from small elemental area  $dS_s$  of stator's South Pole along z axis (m);  
 $L_s$ : Stator length along stator z axis (m);  
 $L_r$ : Rotor length along stator z axis (m);  
 $\delta$ : Maximum radial clearance between rotor and stator cylindrical axis (m);  
 $F_{ref}$ : Reference force of rotor and stator magnets (N);  
 $F_x$ : Magnetic force along x axis (N);  
 $F_0$ : External radial force per bearing applied on journal having rotor (N);  
 $R_1$ : Inner radius of rotor magnet (m);  
 $R_2$ : Outer radius of rotor magnet (m);



$R_3$ : Inner radius of stator magnet (m);  
 $R_4$ : Outer radius of stator magnet (m);  
 $k$ : Magnetic stiffness ( $\frac{N}{m}$ );  
 $\omega$ : Frequency (rad/s);  
 $t$ : Time (s);  
 $\omega_{ref}$ : Reference natural frequency (rad/s);  
 $a_r$ : Frequency that governs growth of vibration (rad/s);  
 $\omega_r$ : Natural frequency (rad/s);  
 $P_a$ : Atmospheric pressure (Pa);  
 $B_n$ : Journal Bearing Number;  
 $h$ : Fluid film thickness in m;  
 $U$ : Fluid film layer (near journal surface) linear speed in m/s;  
 $\mu$ : Coefficient of viscosity of fluid in Pa s (Pascal second);  
 $s$ : Circular circumference of the journal bearing section perpendicular to its rotational axis in m;  
 $R$ : Fluid film journal bearing radius in m;  
 $r$ : Journal radius in m;  
 $D$ : Fluid film journal bearing diameter in m;  
 $L$ : Length of the journal bearing;  
 $\omega$ : Angular spin speed of journal/ rotor;  
 $H$ : Non dimensional thickness of the fluid film defined as the ratio of  $h$  is to maximum radial clearance ( $R-r$ ) between journal and bearing;  
 $\theta$ : Angular length of circumference of the journal bearing section perpendicular to its rotational axis in radian;  
 $\phi$ : Angular position of journal center in radian;  
 $e$ : dimensional eccentricity or radial distance (in polar coordinate) of journal center from bearing center in m;  
 $\epsilon$ : nondimensional eccentricity or nondimensional radial distance (in polar coordinate) of journal defined as  $e$  is to maximum radial clearance ( $R-r$ ) between journal and bearing;





## List of figures

- Fig. 1 Triangular FEM 2D mesh generation of bearing oil film area
- Fig. 2 Minimum absolute error comparisons plot for different computation method
- Fig. 3 Schematic of journal bearing
- Fig. 4 Variation of stiffness coefficients with comparison of analytical [20] for short bearing
- Fig. 5 Variation of direct stiffness coefficients with comparison of previous work [20] for  $L/D = 1$
- Fig. 6 Variation of direct stiffness coefficients with comparison of previous work [20] for  $L/D = 4$
- Fig. 7 Non-dimensional relative pressure distribution along circumference ( $\varepsilon = 0.5$ ,  $\bar{z} = 0.5$ )
- Fig. 8 Non-dimensional relative pressure distribution along the bearing surface ( $\varepsilon = 0.5$ ,  $L/D = 1$ )
- Fig. 9 Contour plot of non-dimensional relative pressure distribution ( $\varepsilon = 0.5$ ,  $L/D = 1$ )
- Fig. 10 Polar plot of attitude angle variation
- Fig. 11 Non-dimensional force variation
- Fig. 12 Variation of non-dimensional stiffness coefficients with eccentricity for  $L/D = 1$
- Fig. 13 Variation of non-dimensional stiffness coefficients with Sommerfield number for  $L/D = 1$
- Fig.14a Partial exploded view of permanent magnetic bearing set up
- Fig.14b A schematic representation for analytical derivation
- Fig. 15 Comparison of axial force computed by proposed model and ref. Lemarquand and Lemarquand [37]
- Fig. 16 Comparison of axial stiffness computed by proposed model and ref. Lemarquand and Lemarquand [37]
- Fig. 17 Comparison of radial force computed by proposed model and ref. Muzakkir et al. [26]
- Fig. 18 Comparison of radial stiffness computed by proposed model and ref. Bekinal et al. [38]
- Fig. 19 Contour plot of non-dimensional radial force



Fig. 20 Contour plot of non-dimensional axial force

Fig. 21 Contour plot of non-dimensional stiffness ( $K_{xx}$ )

Fig. 22 Contour plot of non-dimensional stiffness ( $K_{yy}$ )

Fig. 23 Contour plot of non-dimensional stiffness ( $K_{zz}$ )

Fig. 24 Contour plot of non-dimensional stiffness ( $K_{zx}$ )

Fig. 25 Plot of non-dimensional stiffness v/s radial eccentricity at particular axial eccentricity position

Fig. 26 Plot of non-dimensional stiffness v/s axial eccentricity at particular radial eccentricity position

Fig. 27 Contour plot of non-dimensional 2nd mode natural frequency

Fig. 28 Contour plot of non-dimensional 3rd mode natural frequency

Fig. 29 Schematic of PMB rotor and stator magnet

Fig. 30 Triangular mesh plot of magnets

Fig. 31 Orientation of axis angles and projection angles

Fig. 32 Schematic of mathematical model of PMB load

Fig. 33 Flowchart of the program of the proposed model

Fig. 34 Relative errors and computation time variation with mesh density

Fig. 35 3D Mesh plot of magnets in a commercial software

Fig. 36 Variation of magnetic axial force on rotor magnet with the variation of axial shift of rotor magnet from stator magnet for validation of present model with the existing model

Fig. 37 Variation of magnetic radial force on rotor magnet with the variation of radial shift of rotor magnet from stator magnet for validation of present model with the existing model

Fig. 38 Variation of magnetic moment about centroidal Y axis of rotor magnet for validation of present model with a commercial software

Fig. 39 Magnetic moment with subsequent prediction error bar distribution along axial shift for three different radial shifts differentiating by three colors of blue, magenta and red accordingly

Fig. 40 2D contour plot of magnetic moment about centroidal Y axis distributed over XZ plane

Fig. 41 Magnetic moment with subsequent prediction error bar distribution over tilts about centroidal Y axis of the rotor magnet for three different axial shifts differentiating by three colors of blue, magenta and red accordingly



Fig. 42 2D Contour plot of magnetic moment about centroidal Y axis of rotor magnet distributed over variation of tilt and rotor magnet length

Fig. 43 Schematic front view of hybrid system of bearings

Fig. 44 Schematic end view of hybrid system of bearings

Fig.45 Validation of trajectory of the journal center position of plain cylindrical short bearing

Fig.46 Trajectory of the journal center position of both plain fluid film cylindrical short bearing pair and hybrid system of bearings

Fig.47 Eccentricity of the journal center position of both plain fluid film cylindrical short bearing pair and hybrid system of bearings

Fig.48 Attitude angle of the journal center position of both plain fluid film cylindrical short bearing pair and hybrid system of bearings

Fig.49 Polar plot of attitude angle variation with non-dimensional eccentricity for different characteristic constant of hybrid system of bearings

Fig.50 Contour plot of attitude angle variation for hybrid system of bearings ( $C_m = 2$ )

Fig. 51 Contour plot of bearing load capacity ratio of hybrid system of bearings to double fluid film short bearings system over non-dimensional speed and eccentricity for a typical hybrid system of bearings ( $C_m = 2.4$ , mass ratio = 1.44)

Fig. 52 Contour plot of magnetic force to total load ratio variation over non-dimensional speed and eccentricity for hybrid system of bearings ( $C_m = 2.4$ , mass ratio = 1.44)

Fig. 53 Force components ratio comparisons for various characteristics mixing of fundamental bearings to hybrid system of bearings ( $C_m = 1.2$  and mass ratio = 1.44)

Fig. 54 Variation of non-dimensional natural frequency with respect to non-dimensional spin speed of journal/ rotor

Fig. 55 Variation of non-dimensional growth coefficients with respect to non-dimensional spin speed of journal

Fig. 56 Borderline of stability and start up curve comparisons between hybrid system of bearings over two fluid film bearings system

Fig. 57 Non-dimensional boundary speed variation over characteristic's constants of hybrid systems of bearing

Fig. 58 Minimum eccentricity variation over characteristic's constants of hybrid systems of bearing occurred at boundary speed

Fig. 59 Absolute vertical non-dimensional receptance of both system of bearings for



vertical harmonic force

Fig. 60 Absolute horizontal non-dimensional receptance of both system of bearings  
for vertical harmonic force





## **List of tables**

- Table 1 Data used for journal force calculation
- Table 2 Analytical solution of non-dimensional journal forces of short bearing
- Table 3 Output data of computation time and errors of journal force using FDM with iteration
- Table 4 Output data of computation time and errors of journal force using FDM matrix formation
- Table 5 Output data of computation time and errors of journal force using PDE tool
- Table 6 Grouping variables with their levels
- Table 7 ANOVA table for computation cost
- Table 8 ANOVA table for absolute error
- Table 9 ANOVA table for relative error
- Table 10 Consolidated data of minimum absolute errors in different methods
- Table 11 Algorithm for the proposed model
- Table 12 Data used for force validation
- Table 13 Data used for axial stiffness validation
- Table 14 Data used for radial stiffness validation
- Table 15 Data used for optimization
- Table 16 Optimization results
- Table 17 Physical parameters for validation
- Table 18 Mesh and other parameters for validation
- Table 19 Magnetic stiffness coefficients for equal length of rotor and stator magnet
- Table 20 Magnetic stiffness coefficients for increased length of rotor magnet from stator
- Table 21 Data used for validation
- Table 22 Data used for hybrid system of bearings



# 1. Introduction

This chapter introduces the research work and provide a roadmap for the entire study. The research study aims to enhance the bearing load capacity of a shaft-disc system by investigating three basic problem areas: hydrodynamic bearing, passive magnetic bearing, and hybrid system of bearings. Hence, the scope of the research work is to investigate the three problem areas mentioned above and provide a detailed analysis of each area. The outlines are as objectives of the research work in Section 1.2, which are specific statements that break down the aim into several key sections of the overall research. Finally, it provides a roadmap in the introduction part detailing how each chapter contributes to achieving these objectives and demonstrating the overall scope of the study.

## 1.1 Research motivations

The aim of the research is

To improve the bearing load of a shaft-disc system.

The specific objectives are

- To study the oil film bearings.
- To study the permanent magnet bearings
- To investigate alternative approaches for identifying stiffness properties of permanent magnet bearings
- To investigate the mixed behaviors of oil film bearing and permanent magnet bearing

## 1.2 Thesis outline

- In consistent of the goals and objectives of the thesis as mentioned above in this chapter, the following outline covers here.
- In Chapter 2, the following brief literature review appears.
  - Oil film bearings: Important for machines with rotating shafts. Research is ongoing to improve them.
  - Permanent magnet bearings: A new type of bearing with advantages and disadvantages. More research is needed.
  - Hybrid bearings: Combine the best of both worlds. Researchers are working on them.
- In persuasion of the first objective from Chapter 1 and realization of Chapter

2, Chapter 3 compares different methods for estimating the force acting on an oil film bearing. This chapter concludes that the best way depends on the desired accuracy and the available computational time.

- As an extension of Chapter 3, Chapter 4 presents a method to calculate the journal force of a finite-length hydrodynamic journal bearing using the FEM approach. The author compares his methodology to other methods and find it more accurate and less complex. The author also suggests that his way could be used to study dynamic journal bearings. The outcome of this chapter can also add value to the last objective.
- In persuasion of the second and third objectives from Chapter 1 and also realization from Chapter 2, Chapter 5 presents a new approach based on non-dimensional modelling.  
The new approach is more general, easier to use, and more accurate.  
The author validates his method by comparing it to previous research data. The new approach could be a valuable tool for characterizing permanent magnetic bearings.
- In the extension of Chapter 5, Chapter 6 presents a new approach using FEM to calculate the force and moment on a permanent magnet bearing. In addition to non-dimensional features, the latest simulation method is more accurate and faster than older numerical methods to find the 6-DOF bearing characteristics. It can also be used to study how the bearing works with other things, like fluids. The outcome of this chapter can add value to the last objective as mentioned to the next Chapter.
- In persuasion of the fourth objective from Chapter 1 and realization of Chapter 2, Chapter 7 covers the following outline  
The hybrid system of bearings can combine the advantages of permanent magnet bearings and fluid film bearings.  
This work presents an analytical non-dimensional model of a hybrid system of bearings consisting of a passive magnetic bearing and a fluid film plain cylindrical short bearing.  
An analytical study of a hybrid system of bearings can help designers choose design parameters and check feasibility.
- Chapter 8 discusses the overall conclusions and potential future work attractions.

## 2. Literature review

This chapter discusses a brief literature review on oil film bearing simulation methods, permanent magnet bearing characteristics, analysis approaches, advantages and limitations of PMB, and hybrid systems with magnet bearing and oil film bearing. The intention of this review to find the research gap in pursue with the objectives as mentioned in Chapter 1.1.

### 2.1 Oil film bearing simulation methods

Oil film bearing may be considered incompressible fluid film bearing to tell its more generic form. A hydrodynamic journal bearing is a sliding contact bearing operating with hydrodynamic lubrication. In the radial hydrodynamic journal bearing, if the journal revolves in a forward direction, the journal does pump action on the lubricant flowing all over the bearing in the direction of rotation. If no force is exerted on the journal, its position will remain concentric on the bearing position. However, a loaded journal moves out from the concentric location, creating a nonuniform gap between the bearing and journal surfaces. The pumping phenomena of the journal force the oil to squeeze through the wedge-shaped gap, thus generating pressure. The pressure falls to the cavitation pressure (closest to atmospheric pressure) in the diverging gap zone where cavitation starts. The oil pressure produces a separating force, pushing the journal from the bearing surface. The force of oil pressure and the hydrodynamic friction force balance the external load  $F$ . The equilibrium among these forces determines the final position of the journal. Journal bearing can work in any of three lubrication regimes, thick-film lubrication, thin-film lubrication and boundary lubrication. Hydrodynamic journal bearing is also called self-acting bearings. It depends entirely on the relative motion of the journal to the bearing to make film pressure for load support.

E. Kramer [1] presented the derivation of the classical Reynolds equation clearly and distinctly. The formulation and calculation of stiffness and damping coefficients for short cylindrical bearings were explained using the short bearing approximation of the Reynolds equation. The empirical relation was established between the attitude angle, eccentricity, and static equilibrium curves for different bearings.

Sarkar et al. [2] discussed the finite element analysis of misaligned rotors on short oil-film bearings of various types. Lagrange multipliers modelled the angular misalignment. The static equilibrium position of the journal was found by the iterative non-linear static finite element method. Finally, the orbit of the rotor around the static equilibrium was determined using a time-integration scheme.

Machado and Calvacla [3] presented the solution of the Reynolds equation for pressure field using the finite difference method. It gave pressure distribution for different types of bearings.

Faria [4] presented the application of the finite element method with the development of computational procedures for hydrodynamic elliptical journal bearing. The finite

element formulation for the classical Reynolds equation was made, and the pressure field was calculated. The methods used here to calculate load capacity and stability formulation were unique. Other researchers validated the results obtained for the finite element method.

Rowe and Chang [5] used the finite difference method for calculating the pressure field from the Reynolds equation based on which non-dimensional linearized dynamic coefficients. Finite difference and perturbation techniques were used to predict dynamic coefficients. Both analyses considered the classical Reynolds equation with a flow source, film rupture and iso-viscous fluid. This paper gave a clear picture of dynamic coefficients and a detailed flowchart.

Hirani [6] presented the derivation Reynolds equation from Navier stokes equation using certain assumptions. The boundary conditions viz. Full Sommerfeld and half Sommerfeld boundary conditions were studied. Different types of bearings were studied, such as hydrostatic bearings, squeeze film bearings, and elasto-hydrodynamic bearings. The finite difference method to solve the Reynolds equation and derivation of film thickness was done.

Sarkar et al. [7] described a non-linear finite element analysis of a statically determinate shaft-disc system connected to short oil film bearing of various types (cylindrical, pocket, symmetrical and unsymmetrical three-lobed). At first, they determined the static position of the journal by using an iterative non-linear static analysis, where the journal force at the location of the bearing was balanced with the bearing force. The non-linear transverse forces of the journal were expanded in Taylor's series in two variables, and finally, they computed the locus of the journal around the static equilibrium position.

Chapra [8] discussed the finite difference techniques for solving different partial differential equations. Other numerical tools like the finite element and finite volume methods and their applicability were studied. The Gauss seidel over relaxation method was studied and used in the present work.

Stachowiak and Batchelor [9] presented the formulation and derivation of the Reynolds equation. The misalignment parameter was considered in the expression of film thickness in the Reynolds equation. The solution of the classical Reynolds equation was done using the finite difference method using the Vogelpohl parameter. The pressure field and dynamic coefficients were calculated using the Vogelpohl parameter for partial and grooved bearings.

Budynas and Nisbett [10] showed the pattern of journal movement as a function of speed and viscosity eccentricity ratio. A comparative study was done between the texts learnt from Bhandari and Sigley. The Raimondi Boyd solution was again studied. The short-bearing and long-bearing approximations were discussed. The working of a journal in loaded and unloaded condition was investigated.

Sfyris and Chasalevris [11] presented a picture of the solution of the Reynolds equation by using an exact analytic solution. It used different mathematical tools and techniques like the Bessel function and the Sturm-Liouville problem for the eigenvalues power series method. They used the 3-D CFD method for solving numerical validation. They

also validated the results with the finite difference method.

Bhandari [12] and Tiwari [13] described the classification of different fluid film bearings such as hydrostatic and squeeze film bearings, which were made very clear. The finite difference solution of the Reynolds equation was done. The empirical relation was made for calculating the Sommerfeld number and dynamic coefficients. The numerical method for finding the stiffness and damping coefficients was discussed.

Raimondi and Boyd [14] presented three papers in a series which explain the iteration technique to solve the Reynolds equation for a finite width bearing. It considers the coefficient of friction variable, side leakage and temperature rise to give the solution of the Reynolds equation.

Lund [15] presented the idea of representing the rotor system as a spring mass damper system and how the determination of dynamic coefficients of the bearing makes a crucial contribution to the field of rotor dynamics. It gives the idea of short and long-bearing approximations.

Zhou et al. [16] described the finding of dynamic coefficients of a fluid film bearing and determined the static equilibrium position, which is the most important and inevitable step. It gives an idea of the superliner iteration method for calculating the stable equilibrium position of the journal in finite length bearing.

Lund and Thomson [17] described how to calculate the stiffness a damping coefficient of oil lubricated using a numerical method. It took the film rupture into account. It gave a brief idea of how pressure integration gives rise to load-carrying capacity, four stiffness and four damping coefficients.

Ebrat et al. [18] discussed the solution of the Reynolds equation, including the journal's elastic deformation. It used the finite difference method for solving the equation. The squeeze effect was considered, and a superposition of wedging action and squeeze effect was taken. It considered the bearings with grooves for analysis. The perturbation technique and the successive over-relaxation algorithm calculated the dynamic coefficients.

Huang [19] discussed different types of bearings. The formulation of the Reynolds equation was studied. How the Reynolds equation governs the fluid flow in various bearings was analyzed. The algorithm to solve the modified Reynolds equation for different types of bearings with Fortran code was studied.

Chasalevris and Sfyris [20] analyzed the exact analytical solution of the Reynolds equation of the finite-length plain journal bearing. They evaluated the journal forces of the fluid film in closed form analytically. Also, they estimated the design parameters such as eccentricity ratio, stiffness, damping coefficients and location of the minimum film thickness.

Causton and Mingham [21] described the finite difference method (FDM), which is used to solve partial differential equations (PDEs). Also, they presented specific FDM details, boundary conditions, validation and general concept such as stability and grid independence, which are necessary to solve PDEs using other numerical methods.

## 2.2 Permanent magnet bearing and simulation

This section reviews permanent magnet bearing types, characteristics, design simulation methods, limitations and applications.

### 2.2.1 Permanent magnet bearing

A permanent magnet bearing consists of more than equals two permanent magnets. The most primitive types of permanent magnet bearings are two concentric cylindrical ring types. They are oriented so that the inner ring permanent magnet can bear a load for its stiffness property. Lower magnetic strength and instability of permanent magnetic bearings kept the researchers in abeyance for further development. In the recent past, there have been fewer available research papers on permanent magnetic bearings compared to active magnetic bearings. Research on permanent magnetic bearings was started using the preliminary study of permanent magnets for radial and axial forces [22]. Yung et al. [23] derived the force equation between two small magnetic dipoles smaller than their separation using Taylor expansion for the first non-zero term by vector differential and path integral derivation approaches. In their paper, Simon et al. [24] discussed the spin stabilization of a magnetic levitating top on a magnetic base. Gyroscopic precession around the local magnetic field was considered to predict a maximum stable spin speed of the top. Tan et al. [25] discussed the hybrid bearing. They used permanent magnetic bearing in the experimental test rig of hydrodynamic journal bearing to study the magnetic forces during starting and stopping of the machine. Muzakkir et al. [26] hybridized a magnetic arrangement in a conventional journal-bearing system to perform a feasibility study in heavy and low-speed conditions. They calculated magnetic levitation force theoretically to find the reasons for mechanical contact between rotor and stator magnets.

Different components of hybrid magnetic bearing models were presented by Mukhopadhyay et al. [27]. Vertical instability of repulsive type magnetic bearing system was controlled by using micro-controllers. Azukuzawa and Yamamoto [28] considered a pair of ring-shaped axially polarised permanent magnets as a magnetic top levitating on a giant ring-shaped permanent magnet resting at the bottom. They investigated design parameters for levitation and simulated the behaviour of levitating magnetic top. The optimisation of repulsive forces was carried out for multi-layered permanent magnets by Moser et al. [29]. There was also relevant research on flux density produced by axially polarized permanent magnetic bearings [30]. Methods of estimation of forces and stiffness of permanent magnetic bearings (both radially and axially polarized types) were proposed by many researchers [31-42]. Janssen et al. [43] derived analytical force and stiffness expressions for the cases where the conventional analytical expressions are difficult to solve. They also proposed the analytical stiffness matrix, which is necessary for designing and analysing such magnetic bearings. Another relevant research on the demagnetising field [44] and diamagnetic levitation [45] also advances magnetic bearing research. Some researchers also reviewed the comparison of magnetic bearings over ball bearings [46] and suggested the



improvement of the performance of permanent magnetic bearings using experimental investigation. To achieve less computational time for calculating force between the rotor and stator of permanent magnetic bearing, some researchers tried various statistical approaches, like the Monte Carlo integration technique, in recent years [47-49].

### **2.2.2 Methods for design simulation**

Past researchers have done numerous works on load calculation considering various methods, models and combinations of both. These methods are mainly related to the analytical integral [23, 30, 31, 33, 37, 42, 50-53] statistical Riemann sum and Monte Carlo integration [47, 49, 54], general division approach [48], magnetic scalar and vector potential volume integral [55, 56], magnetic dipole method [23, 36, 50], Taylor's expansion [23], power series expansion [57], surface current model [32, 58, 59], surface charge model or Coulomb model [32, 35, 39, 40, 60, 61], Gauss and Maxwell stress tensor model [62-65], Finite element method [63], semi-analytical [34, 38, 41, 66], and considering cuboid structure [51, 62, 66, 67]. Most of the above approaches have validations among themselves. Some of these papers also have shown practical validation of force only.

There are few articles on the theoretical moment calculation of ring-shaped axially magnetized PMB. Also, no validation plot of PMB moment with the experimental data or other simulation models is found in the literature. However, partly similar work [38] is carried out by Bekinal et al. to characterize magnetic moments without showing validation or comparing results.

### **2.2.3 Advantage and limitation of permanent magnet bearing**

Permanent magnet bearings (PMBs) offer a number of advantages over traditional bearings, including no friction or wear, relatively high stiffness for low speed, damping during pairing with another active magnetic system, wide speed range, low noise and vibration low maintenance, etc.

However, PMBs also have some limitations. The main limitation of permanent magnet bearing is its instability behaviour. Passive magnetic bearing using ferromagnetic material has lesser application due to failing of stability together in all degrees of freedom. Earnshaw theorem [25] always censures its stability simultaneously in all translation axes. Here is some explanation of limitation.

Limited load capacity: PMBs are limited in the amount of load they can support. This is because the magnetic force between the magnets and the rotor is proportional to the air gap between them. If the load is too heavy, the air gap will decrease, which will reduce the magnetic force and cause the rotor to fall.

Susceptibility to external magnetic fields: PMBs can be affected by external magnetic fields, such as those produced by electric motors and transformers. If the external magnetic field is strong enough, it can cause the PMB to malfunction. For example, the

rotor may be unable to levitate properly, or it may vibrate excessively.

**Complex design:** PMBs are more complex to design and manufacture than traditional bearings. This is because the PMB must be designed to precisely control the magnetic field and air gap. Additionally, the PMB must be able to withstand the high temperatures and pressures that can occur in some applications.

**High cost:** PMBs are more expensive than traditional bearings because of their complex design and manufacturing process. Additionally, PMBs typically use high-quality magnets, which are also expensive.

#### **2.2.4 Application of permanent magnet bearing**

Despite their limitations, PMBs are a valuable technology for applications where high performance and low maintenance are required. PMBs are used in a variety of applications, including aerospace, medical devices, semiconductor manufacturing, robotics, wind turbines, the significant limitation is discussed. Hence passive magnetic bearing is generally used with other supporting systems or electromagnets [25, 26, 36, 46, 68-74]. Some PMB designs with such support also got patents [68-70, 74]. The old example of an application was to reduce friction only. The University of Toledo and NASA Glenn Mechanical Components Branch had investigated around 2002 for low friction efficient energy storage devices for use on unmanned, low earth orbit satellites.

### **2.3 Hybridization of permanent magnet bearing and oil film bearing**

Hybridizing magnet and oil film bearing come from cross-fertilizing good properties of magnet bearing and oil film bearing. In this section, there are discussions mainly about how the previous researcher approaches the hybridization concept in the above subject domain.

The interest of a hybridization system of bearings is to obtain good performance characteristics over a system of similar bearings. Different types of the hydrodynamic journal and magnetic bearings have different favourable and unfavourable characteristics. Some well-known characteristics are that fluid film plain cylindrical short bearing has low stiffness at a lower spin speed of journal and becomes zero at zero spin speed. Hence, it cannot take any load at zero or a significantly less typical speed. Whereas permanent magnetic bearing stiffness generally does not depend upon the spin speed of the journal. The permanent magnetic bearing generally does not have its damping phenomenon, which is essential for stability. Fluid film bearing has a damping phenomenon depending on the various spin speed of the journal. Hence, the hybridization of good characteristics is always very interesting to the designer and researcher. The fundamental analysis of the feasibility and optimization of ring-type permanent magnet bearings is investigated experimentally and theoretically in many old and recent researches [22, 28-42, 47-49, 53, 65, 73, 75] The plain fluid film cylindrical bearing also has well-known fundamental characteristics, which are

available in many past research and studies [15, 16, 20, 76-99]. There has been much experimental investigation of the hybrid bearings system but in compact and integrated shapes as one bearing. Some are based on permanent magnets and hydrodynamic or fluid film bearing for investigating design feasibility, force optimization, performance, and failure analysis [25, 26, 100-103]. A similar type of many studies has been carried on for a hybridization system of active magnetic bearing and hydrodynamic bearing [104, 105]. Permanent magnets are also used with active magnetic bearing as hybridization [106-109], where fluid film bearing is not used. Some other hybridization concepts with permanent magnet bearings are also studied for different areas of application, like rotary blood pump application [110] and infrastructure engineering application [111]. The interest and conclusions found in previous research [25, 26, 100-105] indicate that the hybrid bearings system has feasibility and advantages. It is also seen that there needs to be a more focused area in theoretical study, especially in the non-dimensional characterization of such a system of bearings. In theory, only one recent research showed such an approach to explain the behaviour of the hybrid bearing, which is combined with fluid film, plain cylindrical bearing and electromagnetic bearing [105].

## **2.4 Summary**

In Chapter 2.1, it is seen from the literature review there have many establish a method to simulate oil film bearings, but there may need to have a proper choice of solver to have the desired simulation of bearing force and characteristics.

In Chapter 2.2, the literature review clearly indicates that the permanent magnet bearings have some special properties that always attract academic and industrial researchers for further investigations. The stiffness coefficients are the key properties of such bearings, which needs to be explored with six degrees of freedom. Further, the researcher tried many methods for simulating permanent magnet bearings. So, there is a requirement for such a method that is suitable to simulate 6-DOF stiffness coefficients with easiness. The most important thing is that the ring shape passive permanent magnet bearing always needs some other coupling or support parameters to have stable characteristics.

In Chapter 2.3, it is seen from the literature review there has a trend of study of cross-fertilization of active magnet bearing and hydrodynamic journal bearing. But there is a gap in the hybridization of passive permanent magnet bearing and incompressible fluid film bearing.

### 3. Solver study and methods

To address the first objective of the research and the gap realized from the literature review of Chapter 2.1, as also expressed in Chapter 2.4, The following works become essential. This chapter introduces three approaches to analyses the errors for calculating the journal force of a short cylindrical oil film journal bearing. The pressure distribution in oil film short journal bearing has been determined with the help of Reynold's equation. Fluid is assumed incompressible and steady. This work investigates three different computation methods, FDM conventional, FDM matrix formation and FEM using PDE solver, for calculating journal force. The results show that the absolute error percentage for force calculation in the short cylindrical bearing is minimal using the FEM PDE solver compared to the other two methods. Also, a vivid statistical analysis is carried out with the help of the ANOVA tool to understand the dependency of the method, step or element size and eccentricity on computational time and errors.

#### 3.1 Introduction

From the literature in Chapter 2.1, the basic idea about the solution of the Reynolds equation was gained. Different numerical methods like FDM, FEM, and analytical methods were understood. It was evident from the literature that solving the Reynolds equation is necessary.

A rotor system is always supported by bearings that may be sliding or ball, or roller bearings. A general idea about the bearings is of utmost importance to study the pressure and force characteristics. In most heavy-duty works, sliding bearings are used, of which fluid film bearing is the most critical category.

Finding the pressure distribution of the fluid film bearing has very high importance in the field of journal bearing. The Reynolds equation governs the flow of lubricant in the fluid film bearing by O. Reynolds. The analytical solutions are readily available for very short or very long bearings approximations, called Somerfield's solution. However, the analytical solutions are hardly possible for a real finite width bearing, so they are less appreciable. So, numerical methods such as finite difference methods and finite elements take hold over analytical ones. Solving the Reynolds equation is an inevitable step for the design of a natural bearing. After solving the same, it is possible to find the load-carrying capacity, friction coefficient, lubricant flow rate, static equilibrium positions and a

Lot more. Many researchers have made heroic attempts to solve the Reynolds equation using various analytical and numerical methods in the last four to five decades. Here is an attempt to solve the Reynolds equation for oil film short journal bearings using the finite difference method, FDM Matrix and FEM PDE solver. The solution of the Reynolds equation is used to find load carrying capacity and the attitude angle. After calculating the journal forces, a graph is developed between errors of force and eccentricity in the different computational methods. The eccentric position, as well as the attitude angle, gives the equilibrium position of the journal bearing.

### 3.2 Journal force expression from Reynold's equation

Differential expression of Reynolds equation is considered as below,

$$\frac{\partial}{\partial s} \left( \frac{h^3}{\mu} \frac{\partial p}{\partial s} \right) + \frac{\partial}{\partial z} \left( \frac{h^3}{\mu} \frac{\partial p}{\partial z} \right) = 6U \frac{\partial h}{\partial s} + 12 \frac{\partial h}{\partial t} \quad (1)$$

Non-dimensional differential expression of Reynolds equation is

$$\frac{\partial}{\partial \theta} \left( H^3 \frac{\partial \bar{P}}{\partial \theta} \right) + \left( \frac{1}{4L_d^2} \right) \frac{\partial}{\partial \bar{z}} \left( H^3 \frac{\partial \bar{P}}{\partial \bar{z}} \right) = \frac{\partial H}{\partial \theta} + \frac{2}{\omega} \frac{dH}{dt} \quad (2)$$

$$\text{Where, } \bar{P} = \frac{p}{P_{ref}}, P_{ref} = \frac{6U\mu R}{(R-r)^2}, \bar{z} = \frac{z}{L}, L_d = \frac{L}{D}, \varepsilon = \frac{e}{(R-r)}, \omega = \frac{U}{R} \quad (3)$$

$$H = 1 - \varepsilon \cos(\theta - \phi) \quad (4)$$

$$\frac{\partial H}{\partial \theta} = \varepsilon \sin(\theta - \phi), \quad (5)$$

$$\frac{dH}{dt} = -\varepsilon \sin(\theta - \phi) \dot{\phi} - \dot{\varepsilon} \cos(\theta - \phi) \quad (6)$$

For steady analysis non-dimensional differential expression of Reynolds equation is generally considered as

$$\frac{\partial}{\partial \theta} \left( H^3 \frac{\partial \bar{P}}{\partial \theta} \right) + \left( \frac{1}{4L_d^2} \right) \frac{\partial}{\partial \bar{z}} \left( H^3 \frac{\partial \bar{P}}{\partial \bar{z}} \right) = \frac{\partial H}{\partial \theta} \quad (7)$$

For short bearing non-dimensional differential expression eqn. (7) reduces to

$$\left( \frac{1}{4L_d^2} \right) \times \frac{\partial}{\partial \bar{z}} \left( H^3 \frac{\partial \bar{P}}{\partial \bar{z}} \right) = \frac{\partial H}{\partial \theta} \quad (8)$$

In this theory pressure variation with respect to circumference is considered zero, thus  $\partial p / \partial s = 0$ . And it gives the analytical relative pressure distribution function as mentioned below

$$\bar{P} = 2 \times L_d^2 \times \frac{\varepsilon}{H^3} \times (\bar{z}^2 - \bar{z}) \times \sin(\theta - \phi) \quad (9)$$

Where  $\theta$  ranges at circumferential direction from 0 to  $2\pi$  and  $\bar{z}$  ranges axially from 0 (one side of journal end) to 1 (opposite side of journal end). Here,  $\bar{z}$  and  $z$  is nondimensional and dimensional location of the journal bearing along the axis of the journal bearing and applicable to Chapter 3 and 4 only.

And non-dimensional analytical journal force for short bearing can be found by conventional method [112] and expressed as mentioned below

$$\bar{F} = \left( \frac{\pi}{6} L_d^2 \right) \times \frac{\varepsilon}{(1-\varepsilon^2)^2} \times \sqrt{1 - \varepsilon^2 + \left( \frac{4}{\pi} \varepsilon \right)^2} \quad (10)$$

The author has calculated the same force in three different methods in this work. The first method is the Finite difference method using iteration. The second is the finite difference method using matrix formation, and the third is the FEM using PDE solver.

### 3.3 FDM approach

Using FDM approach equation (7) can be written following similar way as presented by Huang [113]

$$A_i \bar{P}_{i-1,j} + B_i \bar{P}_{i,j-1} + C_i \bar{P}_{i,j} + D_i \bar{P}_{i+1,j} + E_i \bar{P}_{i,j+1} = F_i \quad (11)$$

where,

$$A_i = H_{i-\frac{1}{2}}^3, B_i = \alpha^2 H_i^3, D_i = H_{i+\frac{1}{2}}^3, C_i = -(A_i + D_i + 2B_i), E_i = B_i \quad (12)$$

$$F_i = s^2 \left[ \varepsilon \sin(\theta_i - \varphi) - \frac{2}{\omega} \{ \varepsilon \dot{\varphi} \sin(\theta_i - \varphi) + \dot{\varepsilon} \cos(\theta_i - \varphi) \} \right] \quad (13)$$

#### 3.3.1 Conventional FDM method using iteration

In finite difference method with iteration [113] equation (11) is written in the form of equation (14) as follows.

$$\bar{P}_{i,j} = \frac{F_i - A_i \bar{P}_{i-1,j} + B_i \bar{P}_{i,j-1} + D_i \bar{P}_{i+1,j} + E_i \bar{P}_{i,j+1}}{C_i} \quad (14)$$

In this method, three following assumptions are considered to obtain the pressure from equation (14). Initial pressure at all nodes of the grid of inside fluid film is considered 0.5 during the iterative solution of pressure. Modification of pressure as per the algorithm [113] is considered using relaxation coefficients of 0.3 for present pressure and 0.7 for pressure calculated just before that step of the iteration. The minimum fractional relative error of pressure is considered at every iteration step to its earlier iteration step. The maximum number of iterations is considered 30000.

#### 3.3.2 FDM method using matrix formation

This method is little bit similar as presented by Causon and Mingham [5].

Using this method equation (11) can be written as matrix form shown in equation (15).

$$[LC] \times [Nodalpressure] = [RC] \quad (15)$$

Where, [LC] is sparse matrix as shown in equation (16).

$$\begin{bmatrix}
 C_1 & D_1 & & & A_1 & E_1 & & & \\
 A_2 & C_2 & D_2 & & & E_2 & & & \\
 & A_3 & \ddots & \ddots & & & \ddots & & \\
 & & \ddots & \ddots & C_{N-1} & D_{N-1} & & E_{N-1} & \\
 D_N & & & A_{N-1} & A_N & C_N & & E_N & \\
 B_1 & & & & & & A_1 & E_1 & \\
 & B_2 & & & C_1 & D_1 & D_2 & & \\
 & & \ddots & & A_2 & C_2 & \ddots & & \\
 & & & B_{N-1} & & A_3 & \ddots & \ddots & \\
 & & & & B_N & D_N & & & \\
 & & & & & B_1 & \ddots & & \\
 & & & & & & B_2 & \ddots & \\
 & & & & & & & \ddots & \\
 & & & & & & & & D_{N-1} \\
 & & & & & & & & A_N \\
 & & & & & & & & C_N
 \end{bmatrix}_{MN \times MN} \quad (16)$$

$$[RC] = \begin{bmatrix} F_1 \\ F_2 \\ \vdots \\ \vdots \\ F_{N-1} \\ F_N \\ F_1 \\ F_2 \\ \vdots \\ \vdots \\ \vdots \\ F_{N-1} \\ F_N \end{bmatrix}_{MN \times 1} \quad (17)$$

$$[Nodalpressure] = \begin{bmatrix} \bar{P}_{1,1} \\ \bar{P}_{2,1} \\ \vdots \\ \vdots \\ \bar{P}_{N-1,1} \\ \bar{P}_{N,1} \\ \bar{P}_{1,2} \\ \bar{P}_{2,2} \\ \vdots \\ \vdots \\ \vdots \\ \bar{P}_{N-1,M} \\ \bar{P}_{N,M} \end{bmatrix}_{MN \times 1} \quad (18)$$

Here along the circumferential axis, N numbers of nodes and along the length of the journal, M numbers of nodes are considered. Hence MN numbers of equations are formed in square matrix format. As relative pressure outside these nodes along journal length is zero, the following relation is used for boundary condition.

$$\bar{P}_{1, \dots, N, 0} = 0 \quad (19)$$

$$\bar{P}_{1, 1, \dots, M} = 0 \quad (20)$$

$$\bar{P}_{1, \dots, N, M+1} = 0 \quad (21)$$

After calculating nodal pressure, same standard conventional algorithm [113] is used to calculate journal force. For short bearing Ai, Di will be zero in eqn. (11), (14) and (16) when eqn. (8) is referred to FDM method.

### 3.4 FEM approach

In this proposed method PDE tool for solving eqn. (7) and (8) can be used. Triangular mesh elements are created in this method as shown in Fig 1.

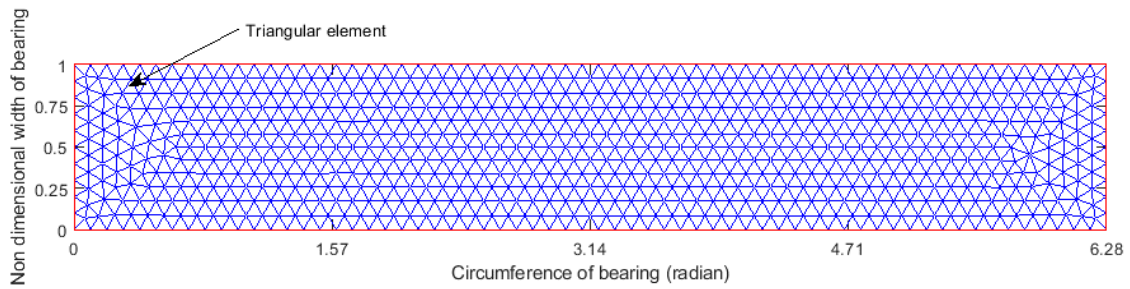


Fig. 1. Triangular FEM 2D mesh generation of bearing oil film area

For short fluid film bearing Eqn. (8) is solved using the PDE tool function to calculate the pressure at all nodal points. The author has derived pressure at the centroids of each triangular mesh using linear interpolation of the nodal pressure of each triangle. After that, journal force components and resultant journal force are calculated using Eqn. (22), (23) and (24).

$$\bar{F}_x = \sum_{i=1}^T \bar{P}_i \times S_i \times \cos x_i \quad (22)$$

$$\bar{F}_y = \sum_{i=1}^T \bar{P}_i \times S_i \times \sin x_i \quad (23)$$

$$\bar{F}_b = \sqrt{(\bar{F}_x^2 + \bar{F}_y^2)} \quad (24)$$

Where  $\bar{F}_b$  is resultant journal force and  $\bar{F}_x$ , and  $\bar{F}_y$  are the journal force orthogonal components along radial plane perpendicular to journal rotational axis.  $S_i$  and  $x_i$  are area and circumference coordinate of each mesh accordingly. T is total number of mesh element.



### 3.5 Input parameters

The input data considered for analysis is mentioned in the table 1. But for calculating non-dimensional journal force,  $L_d$  and  $\varepsilon$  are sufficient for short bearing.

Table 1. Data used for journal force calculation

Input parameters	Values (In SI units)
Coefficient of viscosity	0.25
Relative pressure outside oil film	0
Journal radius	0.025
Bearing radius	0.026
Length of the bearing	0.050
eccentricity taken	0.1, 0.3, 0.5, 0.7, 0.9
Angular velocity of journal	60000 (rpm)

### 3.6 Results and statistical analysis

The analytical solution of journal force from eqn. (10) is shown in table 2. These solutions have been used for calculating absolute errors in different method of approaches.

Table 2. Analytical solution of non-dimensional journal forces of short bearing

Eccentricity	0.1	0.3	0.5	0.7	0.9
Force	0.0495	0.1802	0.4625	1.4879	14.7967

#### 3.6.1 Computational time and errors in different methods

Solutions were found at different eccentricities and element sizes, and computational time was recorded in seconds. Absolute error is calculated in percentage concerning force data, as available in table 2. The relative error is also calculated in percentage to previous results where an element or grid size decreases in geometric progression with a factor of multiplication 0.5. The results of the above three methods are shown in Tables 3, 4 and 5, respectively.

Table 3. Output data of computation time and errors of journal force using FDM with iteration

Eccentricity (Non dimensional)	Element size (Non dimensional)	Computation cost (seconds)	Absolute error (%)	Relative error (%)
<b>0.1</b>	<b>0.112</b>	<b>0.50</b>	<b>0.93</b>	<b>49.43</b>
0.1	0.056	2.32	1.88	0.94
0.1	0.028	10.50	2.17	0.29
0.1	0.014	82.19	-1.54	-3.63
0.1	0.007	338.77	76.70	79.46
<b>0.3</b>	<b>0.112</b>	<b>0.27</b>	<b>0.88</b>	<b>49.62</b>
0.3	0.056	1.35	1.87	0.98
0.3	0.028	7.53	2.17	0.30
0.3	0.014	86.09	-1.72	-3.80
0.3	0.007	322.22	30.86	33.15
<b>0.5</b>	<b>0.112</b>	<b>0.13</b>	<b>0.77</b>	<b>50.13</b>
0.5	0.056	0.76	1.84	1.06
0.5	0.028	6.72	2.16	0.31
0.5	0.014	85.13	-1.76	-3.83
0.5	0.007	318.66	2.39	4.22
<b>0.7</b>	<b>0.112</b>	<b>0.12</b>	<b>0.49</b>	<b>51.44</b>
0.7	0.056	0.73	1.76	1.27
0.7	0.028	8.03	2.13	0.36
0.7	0.014	84.38	-1.79	-3.84
0.7	0.007	330.29	-8.28	-6.61
<b>0.9</b>	<b>0.112</b>	<b>0.12</b>	<b>-0.96</b>	<b>59.41</b>
0.9	0.056	0.75	1.41	2.38
0.9	0.028	9.13	2.04	0.62
0.9	0.014	89.89	-1.83	-3.79
0.9	0.007	320.24	-10.87	-9.21

Table 4. Output data of computation time and errors of journal force using FDM matrix formation

Eccentricity (Non dimensional)	Element size (Non dimensional)	Computation cost (seconds)	Absolute error (%)	Relative error (%)
0.1	0.112	0.01	85.03	-21.73
0.1	0.056	0.03	39.83	-24.43
0.1	0.028	0.39	20.16	-14.06
0.1	0.014	4.33	6.77	-11.14

<b>0.1</b>	<b>0.007</b>	<b>179.75</b>	<b>4.61</b>	<b>-1.37</b>
0.3	0.112	0.00	84.95	-21.63
0.3	0.056	0.04	39.81	-24.40
0.3	0.028	0.28	20.16	-14.06
0.3	0.014	4.10	6.77	-11.14
<b>0.3</b>	<b>0.007</b>	<b>177.07</b>	<b>4.61</b>	<b>-1.36</b>
0.5	0.112	0.00	84.74	-21.36
0.5	0.056	0.03	39.78	-24.34
0.5	0.028	0.25	20.15	-14.04
0.5	0.014	4.26	6.77	-11.14
<b>0.5</b>	<b>0.007</b>	<b>175.75</b>	<b>4.61</b>	<b>-1.36</b>
0.7	0.112	0.01	84.23	-20.68
0.7	0.056	0.02	39.68	-24.18
0.7	0.028	0.24	20.13	-13.99
0.7	0.014	4.20	6.77	-11.13
<b>0.7</b>	<b>0.007</b>	<b>175.66</b>	<b>4.61</b>	<b>-1.36</b>
0.9	0.112	0.01	81.58	-16.50
0.9	0.056	0.03	39.19	-23.35
0.9	0.028	0.25	20.03	-13.77
0.9	0.014	4.29	6.74	-11.07
<b>0.9</b>	<b>0.007</b>	<b>174.29</b>	<b>4.60</b>	<b>-1.36</b>

Table 5. Output data of computation time and errors of journal force using PDE tool

Eccentricity (Non dimensional)	Element size (Non dimensional)	Computation cost (seconds)	Absolute error (%)	Relative error (%)
0.1	0.112	2.24	0.34	-0.96
0.1	0.056	6.73	0.08	-0.25
0.1	0.028	24.02	0.02	-0.06
0.1	0.014	86.08	0.01	-0.02
<b>0.1</b>	<b>0.007</b>	<b>274.50</b>	<b>0.00</b>	<b>0.00</b>
0.3	0.112	1.84	0.35	-0.96
0.3	0.056	6.65	0.09	-0.26
0.3	0.028	25.67	0.02	-0.06
0.3	0.014	88.85	0.01	-0.02
<b>0.3</b>	<b>0.007</b>	<b>276.77</b>	<b>0.00</b>	<b>0.00</b>
0.5	0.112	1.84	0.38	-0.96
0.5	0.056	6.58	0.10	-0.28
0.5	0.028	23.92	0.03	-0.07
0.5	0.014	85.99	0.01	-0.02

<b>0.5</b>	<b>0.007</b>	<b>276.30</b>	<b>0.00</b>	<b>0.00</b>
0.7	0.112	1.96	0.43	-0.86
0.7	0.056	6.79	0.11	-0.31
0.7	0.028	24.53	0.03	-0.08
0.7	0.014	86.18	0.01	-0.02
<b>0.7</b>	<b>0.007</b>	<b>280.44</b>	<b>0.00</b>	<b>-0.01</b>
0.9	0.112	2.05	0.61	0.40
0.9	0.056	6.74	0.18	-0.42
0.9	0.028	24.20	0.05	-0.13
0.9	0.014	86.37	0.01	-0.03
<b>0.9</b>	<b>0.007</b>	<b>273.09</b>	<b>0.00</b>	<b>-0.01</b>

### 3.6.2 Analysis of results

The data from table 3, table 4 and table 5 is analysed using the analysis of variance (ANOVA) statistical tool. The analysis is to understand the effect of the method, grid or mesh size and eccentricity on the error and computation time. Three groups of source variables, method, eccentricity and element size, are considered, as shown in Table 6.

Table 6. Grouping variables with their levels

Method	Eccentricity (Non dimensional)	element size (Non dimensional)
FDM with iteration	0.1	0.112
FDM matrix	0.3	0.056
PDE tool	0.5	0.028
	0.7	0.014
	0.9	0.007

To study three response vectors: computation cost, absolute error and relative error, we conducted three ways ANOVA with two factors interaction tests. The ANOVA output tables are shown in table 7, table 8 and table 9 for response vectors of computation cost, absolute error and relative error accordingly.

Table 7. ANOVA table for computation cost

Source	Sum Square	Degree of	Mean Square	F ratio	Probability> F ratio
method	34871.80	2	17435.90	3328.44	<b>0.00</b>
Eccentricity	27.74	4	6.93	1.32	0.28
element size	732287.3	4	183071.85	34947.6	<b>0.00</b>
method: eccentricity	43.45	8	5.43	1.04	0.43
method: element size	47108.51	8	5888.56	1124.10	<b>0.00</b>

eccentricity: element	142.66	16	8.92	1.70	0.10
Error	167.63	32	5.24		
Total	814649.1	74			

In table 7, the probability value of 0.28 indicates that the mean computation cost responses for different eccentricity levels are not that significant. However, methods and element sizes have strong evidence of an effect on computation cost as corresponding probability values are zero in two decimals round off. Lastly, their entries in the probability column of table 7 are the probability value of the null hypothesis for the two-way interactions. The interaction between methods and element sizes is significant as the probability value is zero in two decimals rounded off. The interaction between method and eccentricity is insignificant as the probability value is 0.43, which is comparatively much higher than others. The interaction between eccentricity and element sizes is very little significance, as the probability value shows 0.10.

Table 8. ANOVA table for absolute error

Source	Sum Square	Degree of freedom	Mean Square	F ratio	Probability> F ratio
method	14144.22	2	7072.11	79.07	<b>0.00</b>
eccentricity	393.37	4	98.34	1.10	0.37
element size	6241.58	4	1560.39	17.45	<b>0.00</b>
method: eccentricity	728.66	8	91.08	1.02	0.44
method: element size	16518.70	8	2064.84	23.09	<b>0.00</b>
eccentricity: element	1405.98	16	87.87	0.98	0.50
Error	2862.14	32	89.44		
Total	42294.65	74			

The probability value of 0.37 in table 8 indicates that the mean responses of absolute error for levels of eccentricity are not significantly different. However, methods and element size strongly influence an absolute error as corresponding probability values are zero in two decimals rounded off. The interaction between method and element size is significant as the probability value is zero in two decimals round off. Also, the interaction between method and eccentricity is not significant as a probability value of 0.44. Similarly, the interaction between eccentricity and element size is also significant as the probability value shows 0.50, which is comparatively higher than others.

Table 9. ANOVA table for relative error

Source	Sum Square	Degree of freedom	Mean Square	F ratio	Probability> F ratio
method	9957.97	2	4978.99	52.49	0.00
eccentricity	295.10	4	73.78	0.78	0.55
element size	3761.65	4	940.41	9.91	0.00

method: eccentricity	670.76	8	83.85	0.88	0.54
method: element size	8522.24	8	1065.28	11.23	0.00
eccentricity: element	1611.30	16	100.71	1.06	0.43
Error	3035.64	32	94.86		
Total	27854.67	74			

Similarly, from table 9, it can be interpreted that methods and element sizes both have strong evidence of an effect on relative error while eccentricity remains dormant. The interaction between the method and element size is significant as the probability value is close to zero. The interactions in method-eccentricity and eccentricity-element size are insignificant as probability values are significant.

The levels of absolute minimum errors in different methods at different eccentricities are presented in table 10. Table 10 is prepared with bold-faced rows from tables 3, 4 and 5, which are at a minimum value of absolute errors at different eccentricities. For all cases, the computational cost is less than 300 seconds.

Table 10. Consolidated data of minimum absolute errors in different methods

Method	Eccentricity (Non dimensional)	Grid/element length (Non dimensional)	Computation cost (seconds)	Absolute error (%)	Relative error (%)
FDM with iteration	0.1	0.112	0.50	0.93	49.43
FDM with iteration	0.3	0.112	0.27	0.88	49.62
FDM with iteration	0.5	0.112	0.13	0.77	50.13
FDM with iteration	0.7	0.112	0.12	0.49	51.44
FDM with iteration	0.9	0.112	0.12	-0.96	59.41
FDM matrix	0.1	0.007	179.75	4.61	-1.37
FDM matrix	0.3	0.007	177.07	4.61	-1.36
FDM matrix	0.5	0.007	175.75	4.61	-1.36
FDM matrix	0.7	0.007	175.66	4.61	-1.36
FDM matrix	0.9	0.007	174.29	4.60	-1.36
FEM PDE tool	0.1	0.007	274.50	0.00	0.00
FEM PDE tool	0.3	0.007	276.77	0.00	0.00
FEM PDE tool	0.5	0.007	276.30	0.00	0.00
FEM PDE tool	0.7	0.007	280.44	0.00	-0.01
FEM PDE tool	0.9	0.007	273.09	0.00	-0.01

The absolute error data of table 10 is rounded off up to two decimals points. The same data is plotted in Fig 2.

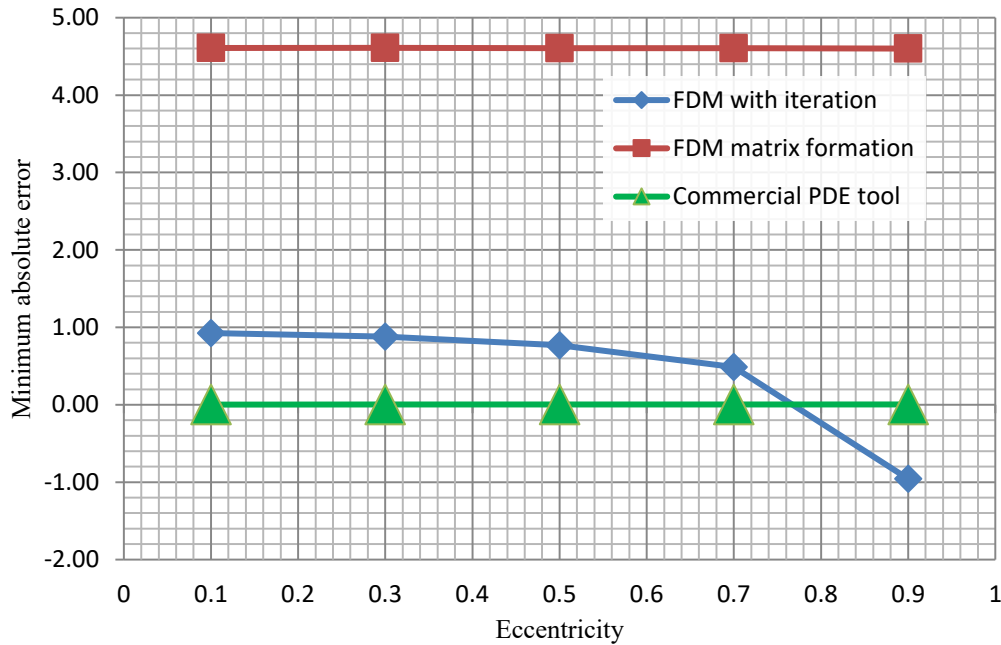


Fig. 2. Minimum absolute error comparisons plot for different computation method

It is seen that the method using FEM PDE tool shows minimum error, almost zero, after rounding off up to two decimal points and remains unchanged with the variation of eccentricity.

### 3.7 Summary

This work presents statistical and graphical comparisons of errors and computational time on non-dimensional journal force estimation for short cylindrical bearings. It is concluded with more than 99.99% confidence that the absolute error, relative error and computational time are affected strongly by the changes in methods and element or grid sizes. It is also seen that eccentricity has much less contribution to errors and computational time compared to methods and element sizes. The FDM Matrix method shows a steady and consistent trend in absolute error with higher computational time (refer to table 4). So, the FDM Matrix method may be a better choice than the conventional FDM on consistency and stability. However, because of the absolute error in short computational time and typical significant size step consideration, the FDM conventional is better than the FDM Matrix method. FEM PDE tool method is much more accurate, consistent and stable in estimating journal force when the problem is allowed reasonable computational time. In this method, Computational time and accuracy increase further as element size decreases. This work shows a way to choose a method and subsequent step or element size depending on the degree of error margin and constraint on computational time. The knowledge of Chapter 3 helps to explore the first objective of the research and transfer to the next Chapter for its fulfilment.

## 4. Stiffness study of journal bearing using FEM approach

In pursuit of the realisation from Chapter 3, this chapter presents the work for the first objective of the research. In this chapter, we use the FEM approach, as realised in Chapter 3, to solve a simplified Reynolds equation to simulate the finite-length oil film-bearing characteristics. Chapter 4 estimates static journal-bearing characteristic parameters, including stiffness coefficients. The present scope of study and investigation is for the cylindrical type of incompressible fluid film journal bearing. Here, the bearings have a finite length of short, medium and long type length to diameter ratio. The estimation of coefficients of stiffness-bearing parameters with this method is validated with previous research. The results of bearing characteristic parameters are shown in a different plot style to interpret the same wisely.

### 4.1 Introduction

This work mainly focuses on calculating the journal force of a hydrodynamic journal bearing using the FEM approach. The pressure distribution in hydrodynamic bearing has been determined with the help of the Reynolds equation. We assume that the fluid is incompressible and steady.

From the literature reviews of Chapter 2.1, it is understandable about the basic idea of the solution of the Reynolds equation. It is noticeable that for calculating the pressure distribution problem in a journal bearing the Reynolds equation is very necessary to understand. Furthermore, from the solution of Reynolds equations, the different types of static journals bearing characteristic parameters, including stiffness coefficients, can be estimated very accurately. There are many methods like FDM, FEM and analytical method also to solve Reynold's equations, but these methods have more complexity and are restricted to some research areas only. However, using FEM approach with FEM PDE solver [114], the Reynolds partial differential equation is solved very quickly and effectively for cylindrical fluid film journal bearing.

### 4.2 Details of the proposed method

This chapter presents the numerical method with a journal-bearing set-up configuration.

#### 4.2.1 Journal and bearing setup

The radius  $R$  journal is considered to rotate with a constant anti-clockwise rotational speed. Journal centre  $C_j$  is located at a point of eccentricity  $e$  to the geometric centre  $C_b$  of the bearing of radius  $R$  and length  $L$ . The journal is subjected to a virtual external



applied force  $F_a$ . The external force is balanced by Reynold's force  $F_b$ . The Reynolds force is developed for the variable pressure distribution on the internal bearing surface. The pressure distribution is generated due to the fluid film variable thickness  $h$  and film tangential velocity along the circumference of the journal's circular cross-section. The schematic layout of the setup is shown in Fig. 3. Half Sommerfield boundary condition is considered for evaluating fluid film pressure distribution. The common assumption is that the fluid is Newtonian, incompressible and flows under laminar, iso-viscous, and isothermal conditions.

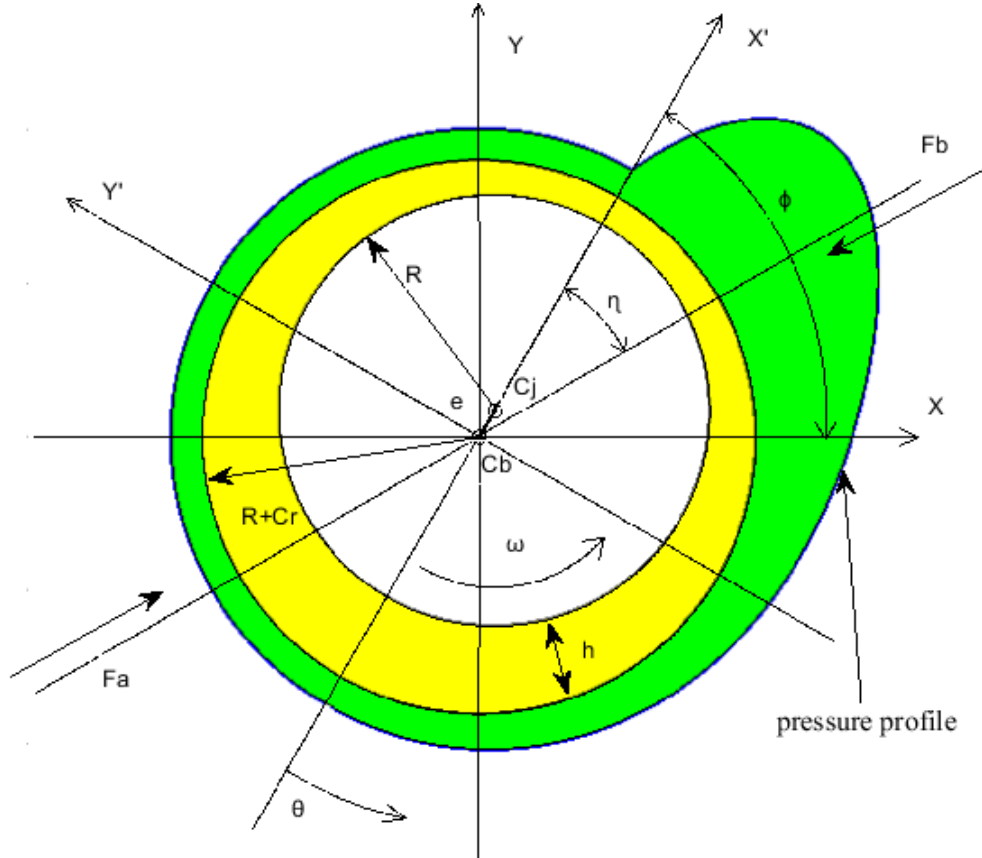


Fig. 3: Schematic of journal bearing

#### 4.2.2 Finite element discretization of fluid film

The fluid film shape is similar to the cylindrical bearing curved surface, which is considered a flat rectangular area for discretization purposes. The surface is discretized using triangular mesh. A discretization plot is shown in Fig. 1 in Chapter 3.4. All nodal point pressure is evaluated using FEM PDE solver for solving (7). The boundary condition at the edges is considered as zero relative pressure.

Summerfield no. expression is considered as

$$S = \left(\frac{1}{2\pi}\right) \times \frac{r^2}{(R-r)^2} \times \frac{\mu L \omega D}{F} \quad (25)$$

Where,

$$D = 2R, \bar{F} = |\bar{F}_a| = |\bar{F}_b| \quad (26)$$

The bearing force can be estimated as below steps and derived in Appendix A.1

$$F_b = \int_0^{2\pi R} \int_0^L P dx dz \quad (27)$$

Where,

$$x = R\theta, z = \bar{z}L \quad (28)$$

Hence, relation (29) can be obtained from relation (26), (27) and (28) in terms of non-dimensional form. The symbol ‘ $\bar{\phantom{x}}$ ’ stands for non-dimensional presentation.

$$F_b = \int_0^{2\pi} \int_0^1 PRL d\theta d\bar{z} \quad (29)$$

Further, from relation (3), (25), (26) and (29) Sommerfeld number relationship with non-dimensional force can be found as below and derived in Appendix A.2

$$S_m = \frac{1}{2\pi L_d^2 \bar{F}} \quad (30)$$

### 4.3 Validation of some stiffness parameters of journal bearing

The FEM PDE solver method for solving PDE is one of the best-validated methods than other conventional methods [114]. The maximum edge length of the mesh is taken at 0.028. The stiffness is calculated using a central finite difference of evaluated force. The results using this proposed method are validated with the available past validated data. An image viewer is used to extract the data in quantified pixel format to get reference data from previous research work in image format. The pixel value is then mapped to the available axis unit. Details of the image data extraction method are described in [53].

#### 4.3.1 The stiffness coefficients validation for short bearing

The stiffness coefficients for short bearing are validated with the data from direct analytical expression [20]. The length-into-diameter ratio for the short bearing is considered 0.1. Non-dimensional eccentricity range is taken from 0.05 to 0.95 at 0.01 increment. The R.M.S errors of Kxx, Kxy, Kyy and Kyx are estimated at 0.0140, 0.0311, 0.2489 and 0.0634, respectively. Here, stiffness coefficients follow a standard suffix notation. For example, Kxy represents the partial derivative of the x-component of the Reynolds force vector with respect to the y-component of the journal position vector. The stiffness analysis for short and finite-length bearings is not discussed in detail in the text but is presented graphically. The RMS errors of stiffness coefficients are calculated using analytic data from Fig. 4 to evaluate and justify the performance of the current FEM PDE model compared to existing models from past research. The comparison plot of the variation of stiffness coefficients for the short bearing is shown in Fig. 4. The conventional analytical method for short bearing does not consider partial pressure derivative terms to circumference in (1). However, all terms in (1) are considered using the proposed method. It has also been observed that the error converges to zero while considering the length diameter ratio much lesser than 0.1.

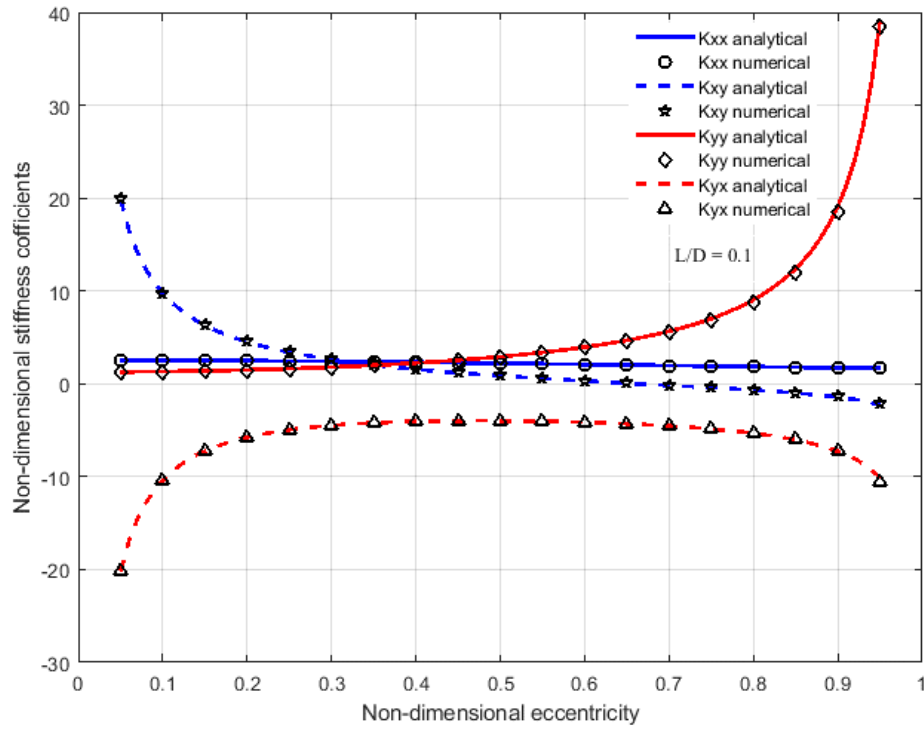


Fig. 4: Variation of stiffness coefficients with comparison of analytical [20] for short bearing

#### 4.3.2 The stiffness coefficients validation of finite length bearing

The direct stiffness coefficients for finite length bearing are validated with previously validated data [20]. A comparison plot of the variation of stiffness coefficients for length diameter ratio one is shown in Fig. 5. The average data of previous research of various methods are considered for estimating R.M.S. error as the previously validated data from another research have significant variance. A total 21 number of points from Summerfield, numbers 0.01 to 10, are taken for error evaluation purposes. The R.M.S. error of  $K_{xx}$  and  $K_{yy}$  is estimated at 0.2482 and 2.0032, respectively. Similarly, the comparison plot of the variation of the same stiffness coefficients for length diameter ratio four is shown in Fig. 6. Total of 21 points from Summerfield numbers 0.01 to 10 are taken for error evaluation purposes. The R.M.S. error of  $K_{xx}$  and  $K_{yy}$  is estimated at 0.0647 and 0.8310, respectively. Results have been observed from Fig. 5 and Fig. 6 that the present study closely matches the previous analytical and numerical data presented by Chasalevris and Sfyris [20]. The currently proposed method also shows a good average estimation of past data in different mentioned methods.

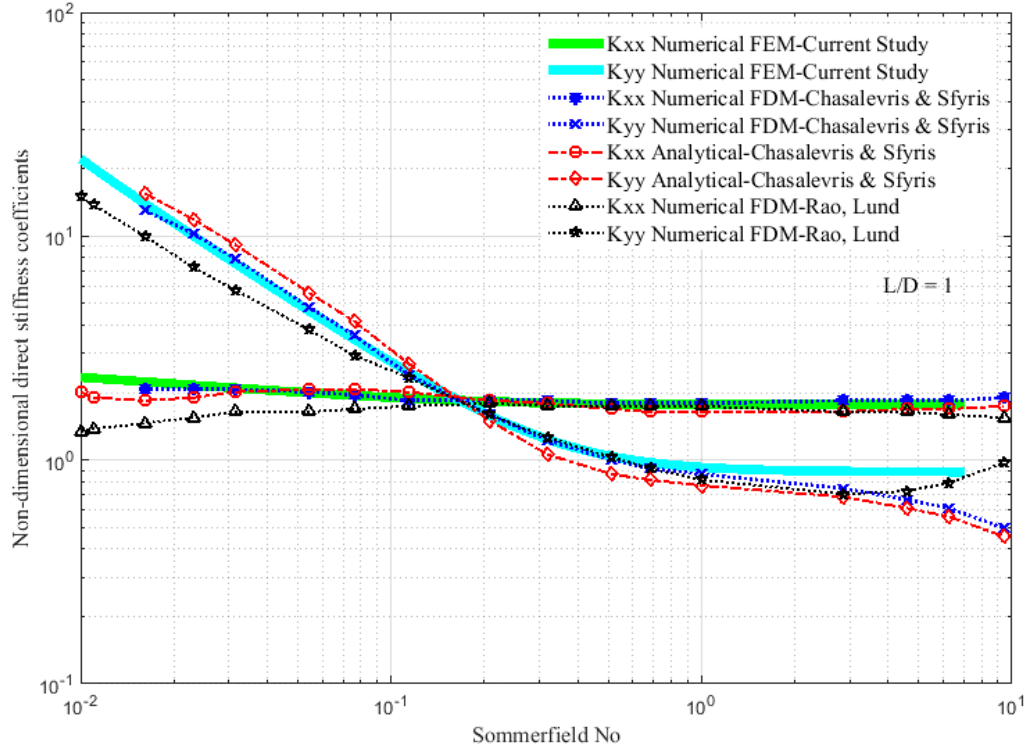


Fig. 5: Variation of direct stiffness coefficients with comparison of previous work [20] for  $L/D = 1$

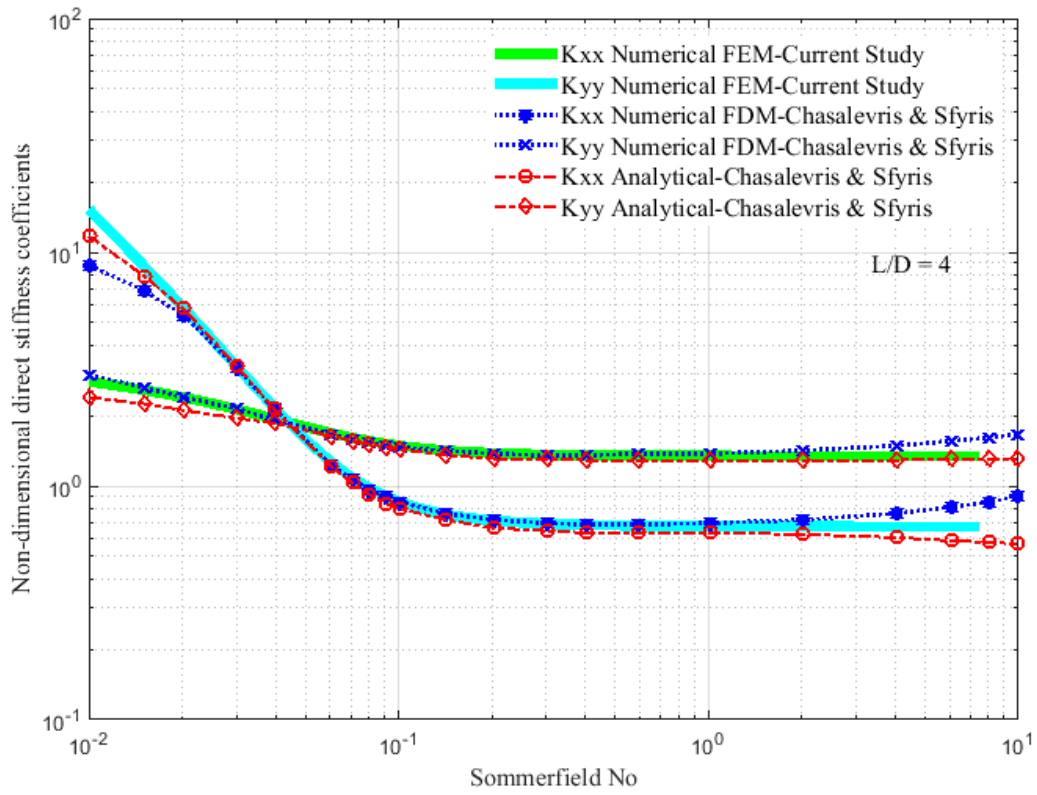


Fig. 6: Variation of direct stiffness coefficients with comparison of previous work [20] for  $L/D = 4$

## 4.4 Results of proposed method

The results of the currently proposed method are presented graphically for various output parameters, including stiffness coefficients for different length diameter ratios of journal bearing.

### 4.4.1 Pressure distribution

Non-dimensional relative pressure variation against the circumference of the bearing is shown in Fig. 7. Pressure variation comparison is also observed for different length-to-diameter ratios in the same figure at the middle line of the axial length of the bearing. The pressure profile becomes high while increasing the length-to-diameter ratio against the same non-dimensional eccentricity.

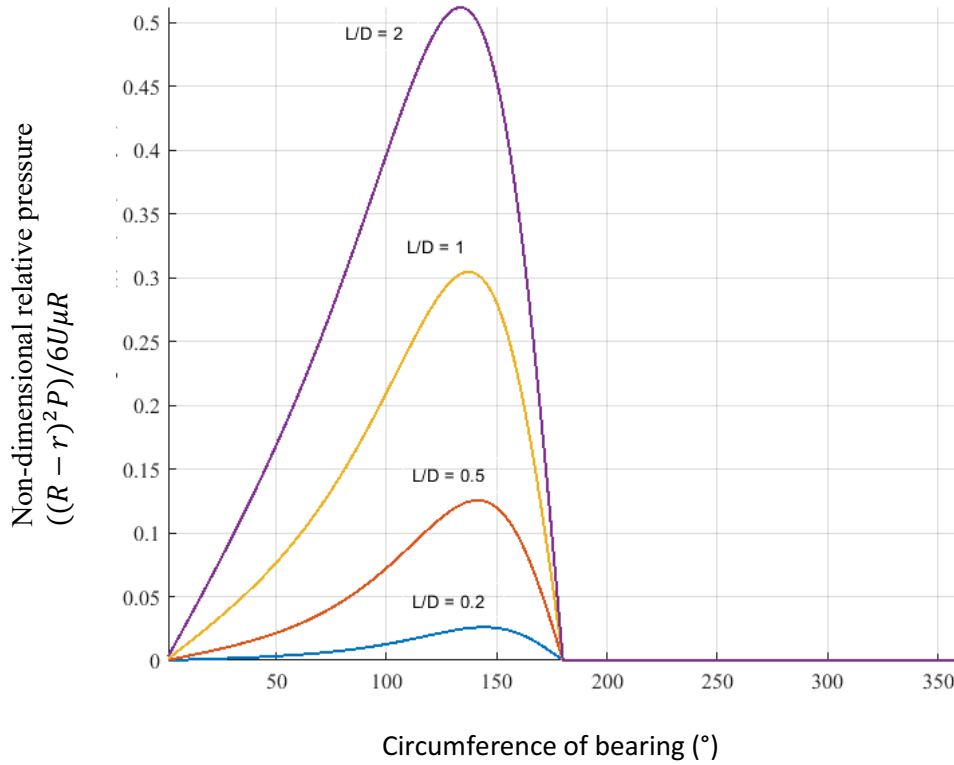


Fig. 7: Non-dimensional relative pressure distribution along circumference ( $\epsilon = 0.5$ ,  $\bar{z} = 0.5$ )

A similar pressure distribution is also shown in Fig. 8 and Fig. 9 in 3D and 2D contour plots. These plots are for length-to-diameter ratio one and non-dimensional eccentricity 0.5 over the entire bearing area. The subsequent colour scale bar in Fig. 8 and Fig. 9 quantifies non-dimensional relative pressure.

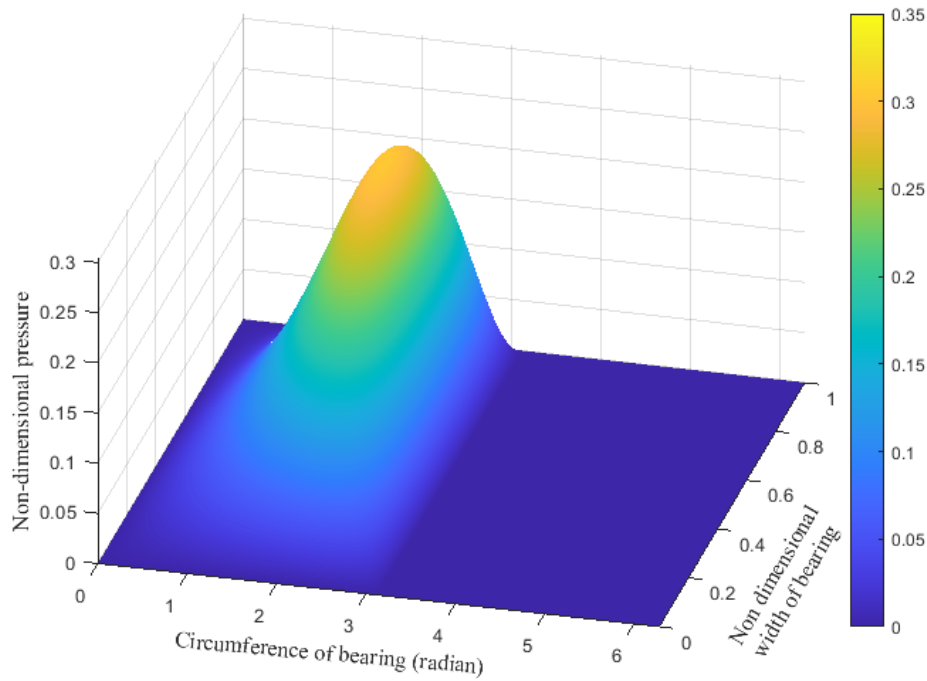


Fig. 8: Non-dimensional relative pressure distribution along the bearing surface ( $\epsilon=0.5$ ,  $L/D=1$ )

Constant pressure lines are visible in the black contour line in Fig. 8. Due to the half Sommerfield boundary condition, relative pressure is zero at half of the locations of the bearing circumference area, as shown in Fig. 8 and Fig. 9.

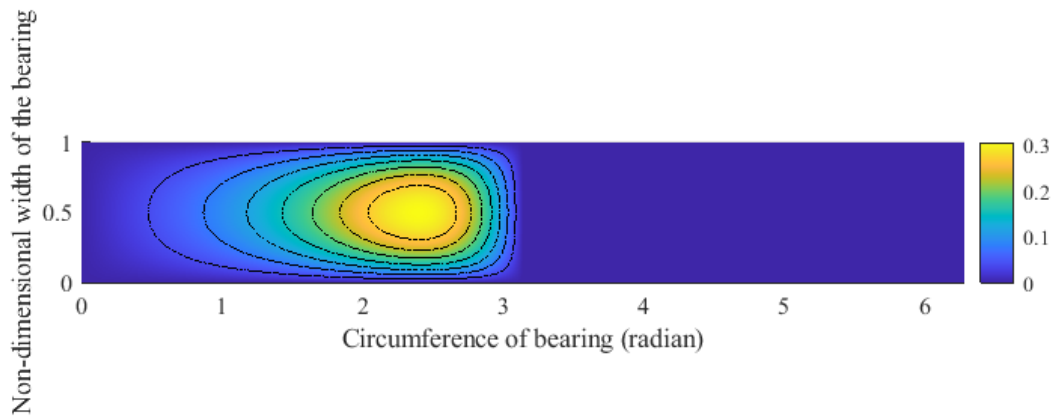


Fig. 9: Contour plot of non-dimensional relative pressure distribution ( $\epsilon=0.5$ ,  $L/D=1$ )

#### 4.4.2 Attitude angle variation

Attitude angle variation with different non-dimensional eccentricities is shown in Fig. 10 as a polar plot. Eccentricity in this plot is considered along the radial direction. The same variations with eccentricity for different length-to-diameter ratios are also shown

in identical Fig. 10.

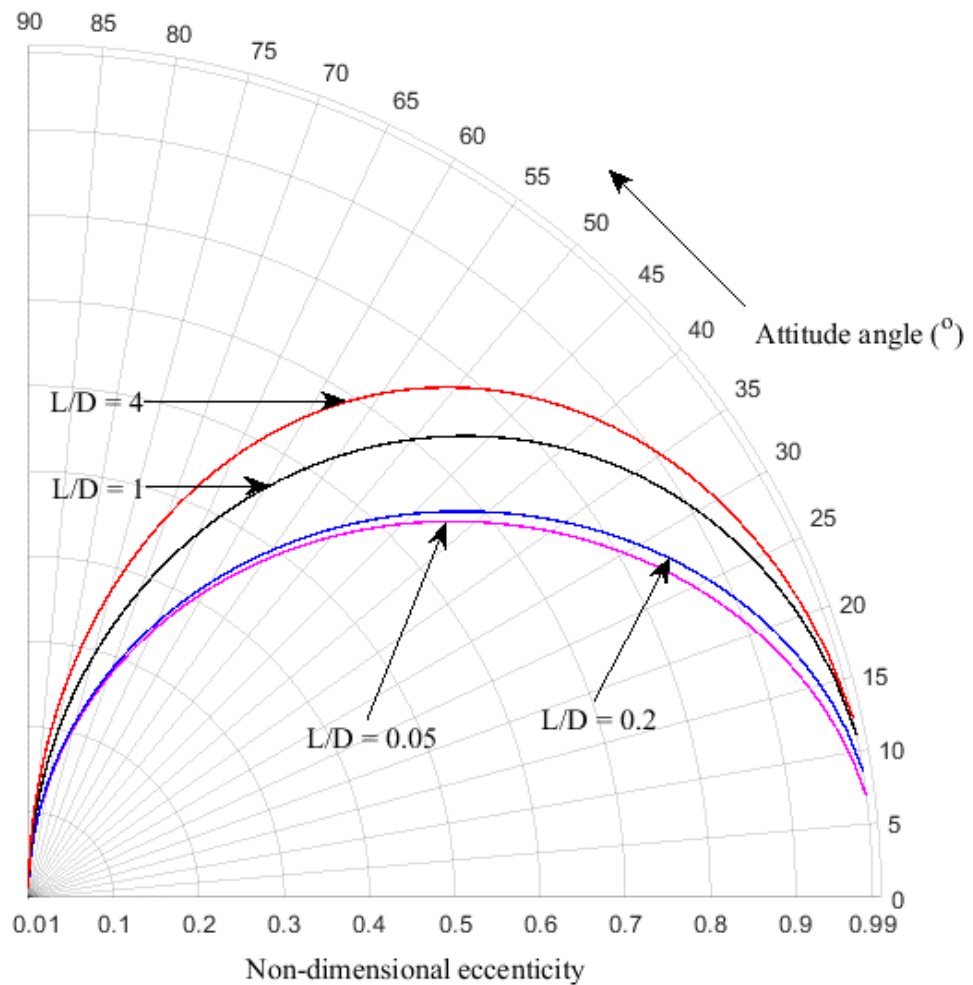


Fig. 10: Polar plot of attitude angle variation

It is clearly observed that the Attitude angle is increasing while increasing the length-to-diameter ratio or decreasing non-dimensional eccentricity, or both.

#### 4.4.3 Force variation

The variation plot of non-dimensional Reynolds static force against non-dimensional eccentricity is shown in Fig. 11, which shows how the non-dimensional static force increases in a non-linear fashion. Also, the same force increases due to the increase in the value of the length-to-diameter ratio of the bearing.

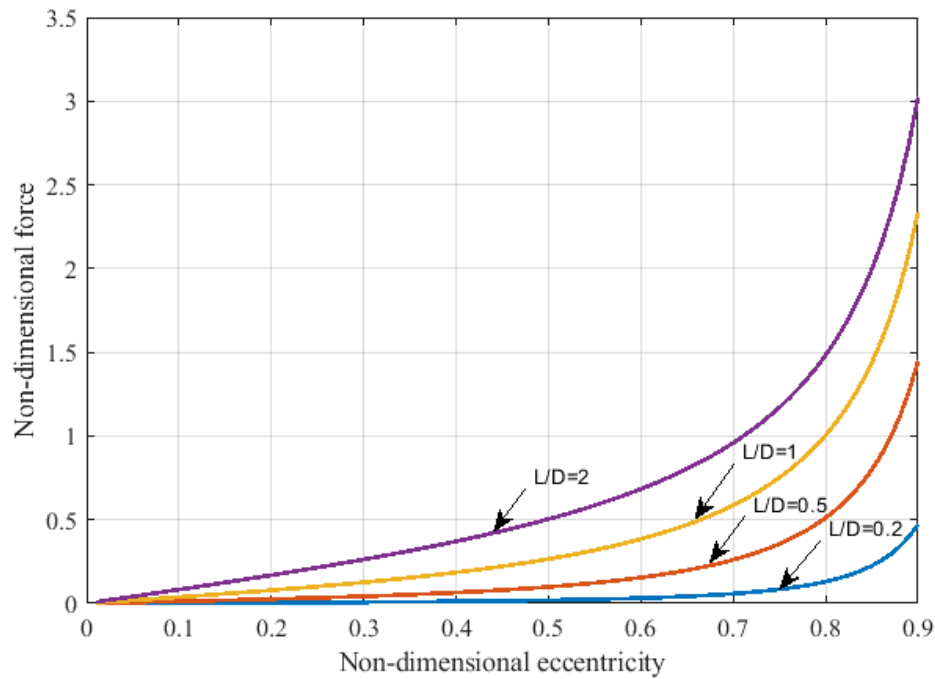


Fig. 11: Non-dimensional force variation

#### 4.4.4 Non-dimensional stiffness coefficients variation

Non-dimensional stiffness coefficient variation is estimated with the variation of non-dimensional eccentricity and Sommerfeld number separately. Non-dimensional stiffness coefficient variation is shown in Fig. 12 and fig. 13 in linear and logarithm scales, respectively.

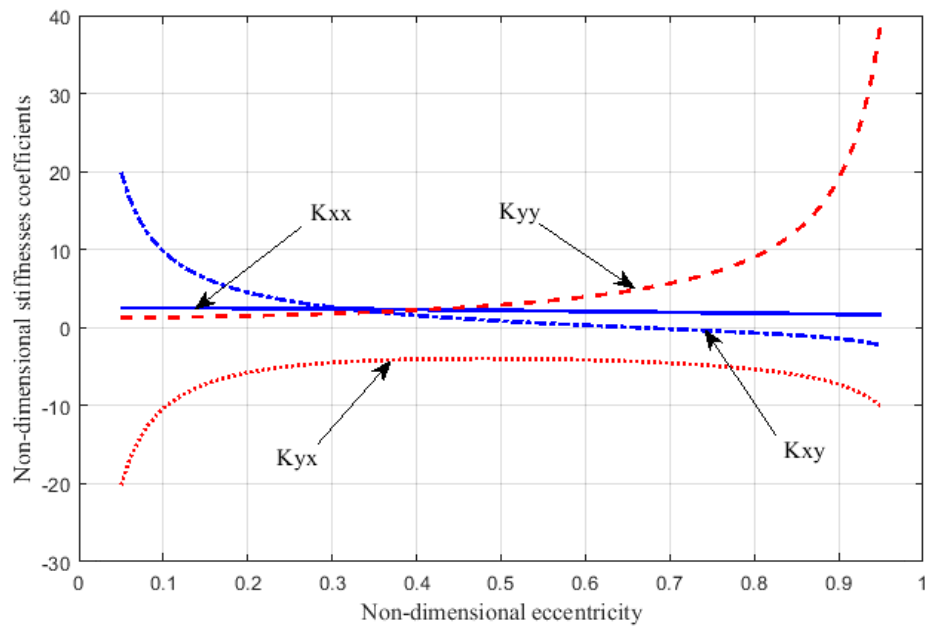


Fig. 12: Variation of non-dimensional stiffness coefficients with eccentricity for  $L/D = 1$



The absolute value of the non-dimensional stiffness coefficient is significantly different at a non-dimensional eccentricity value of less than 0.1 or more than 0.9.

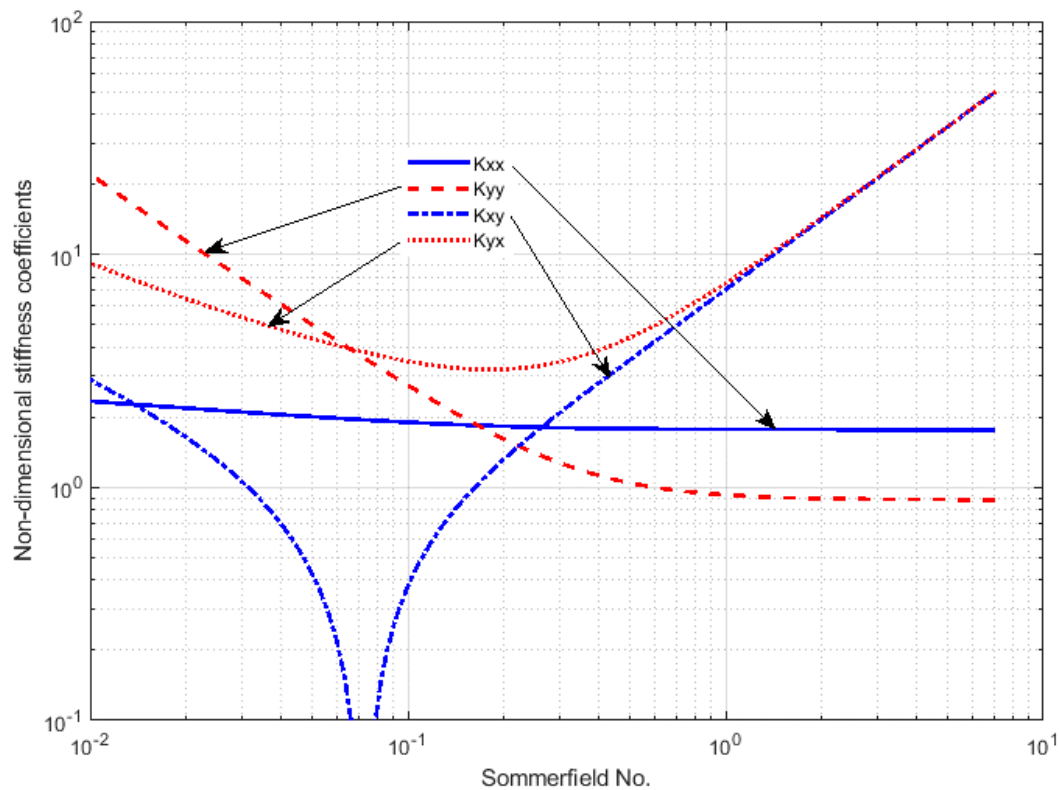


Fig. 13: Variation of non-dimensional stiffness coefficients with Sommerfield number for  $L/D = 1$

## 4.5 Summary

This chapter presents a way of estimating hydrodynamic journals bearing characteristic parameters while the journal is under static equilibrium. With this proposed method using FEM PDE solver tool helps to find a more accurate solution than another method with minimum complexity. The solution can be more accurate if the maximum element size of the triangular mesh is considered 0.007 or less. However, computation cost will grow further with less element size. This method also invites further investigation scope for dynamic study and related characteristic parameter estimation.

Now this knowledge from this chapter can add value to the work for the fourth objective of the research work as shown in Chapter 7.

## **5. Non dimensional numerical study of 3-DOF PMBs**

In pursuance of the second and third objectives of the research and also realization from Chapter 2.2, Chapter 5 presents a new approach based on non-dimensional modelling. This chapter presents a non-dimensional approach with additional parameters like all coefficients of stiffness and natural frequency. The model is considered for static analysis of axially polarized ring-shaped magnets for both stator and rotor parts in three degrees of freedom with three linear translations in a 3D Cartesian coordinate system. The significance of this non-dimensional method to the designer is that parameters like maximum force on the rotor of passive magnetic bearing, and natural frequency, can be easily estimated by simple conversion without doing separate numerical simulations for different parameters every time. The analysis of additional parameters like non-dimensional natural frequency can be the input for non-dimensional dynamic analysis. This chapter also provides a way to maximize radial force with the optimized solution of physical dimensions of passive magnetic bearing as the inner radius of stator and outer radius of rotor magnet while keeping others as input parameters. The proposed model is validated with data available for radial and axial forces, and radial and axial stiffnesses are found in existing literature for similar problems.

### **5.1 Introduction**

It is found from previous literature that with the progress of research, the non-dimensional model approach for calculating forces and stiffness of axially polarized ring-type passive magnetic bearing has yet to be exploited. The non-dimensional analysis is essential to reduce the dependency on the parameters and units of the parameters. Once the non-dimensional generalized relationship is found, it is easy and fast to calculate a customized set of parameters and unit system. This work adopts a non-dimensional modelling approach to determine the optimized design parameters of the rotor and stator part of the bearing. The non-dimensional model is validated after converting it into a dimensional model and comparing it with previous research data already reported in various research papers. The non-dimensional natural frequency of the passive magnetic bearing system is also simulated in this model. Here ring-shaped magnets are used in the rotor and stators. The stator magnet is attached to the static frame of the bearing house, while the rotor magnet is attached to the axial end of the journal. Stator magnet has zero degrees of freedom. However, the rotor magnet can rotate or translate with the shaft, but with no relative motion between them. Force, stiffness, natural frequency, and stability are essential for static and dynamic analyses.

## 5.2 Configuration details for the proposed model

In this chapter, we consider three degrees of freedom configurations of passive permanent magnet bearings to present the non-dimensional approach for finding the non-dimensional characteristics with numerical examples.

### 5.2.1 Permanent magnetic bearing set up

Two pairs of permanent ring-type stator and rotor magnets are attached to the bearing house of fixed reference and journal axial end, respectively. The assembly setup and schematic representations for analytical derivation purposes are shown in fig. 14a and fig. 14b.

In fig. 14a partially exploded view of the model is shown in a simple form where ring types of bushes are shown with the rotor magnet. This view shows axial shift alignment with the stator position. The stator magnet is assumed stationary at the bearing house arrangement by any fixed joining with the housing. The rotor magnet is also assumed to be fixed with the journal shaft, so there is no relative rotation or translation between the magnet and the journal shaft. In fig. 14b, the schematic representation for analytic derivation is shown. An almost Lijesh and Hirani [42] and Santra et al. [47-49] have reported similar sketches. In this fig. 14b the relative axial shift of rotor magnet by  $z$  unit is shown in sections A-A. The section line passing through the centre of the rotor is drawn from the exact figure in side view B. For example,  $z = 15$  unit is considered for the axial shift of the rotor magnet.

Similarly, other values of different parameters are assumed for reference purposes only. The radial shift can be shown in view B of the same fig. 14b. Outer and inner radii for the rotor and stator are shown in this view B in the exact figure. The radial shift of the rotor centre in the direction of  $x$  and  $y$  with respect to cylindrical stator axes are shown in enlarged scale in detail C of fig. 14b. Small arbitrary elemental area in the rotor cross section at radius and angle measured from the rotor centre in a counterclockwise direction is shown in detail C, which is cropped from view B of the same fig. 14b. Similarly, in detail C of fig. 14b, there is another elemental area from the stator cross-section at the radius and angle measured from the stator axis in the counterclockwise direction. Relative displacement of rotor small elemental area and stator small elemental area in  $x$  and  $y$  direction are shown as  $X$  and  $Y$ .

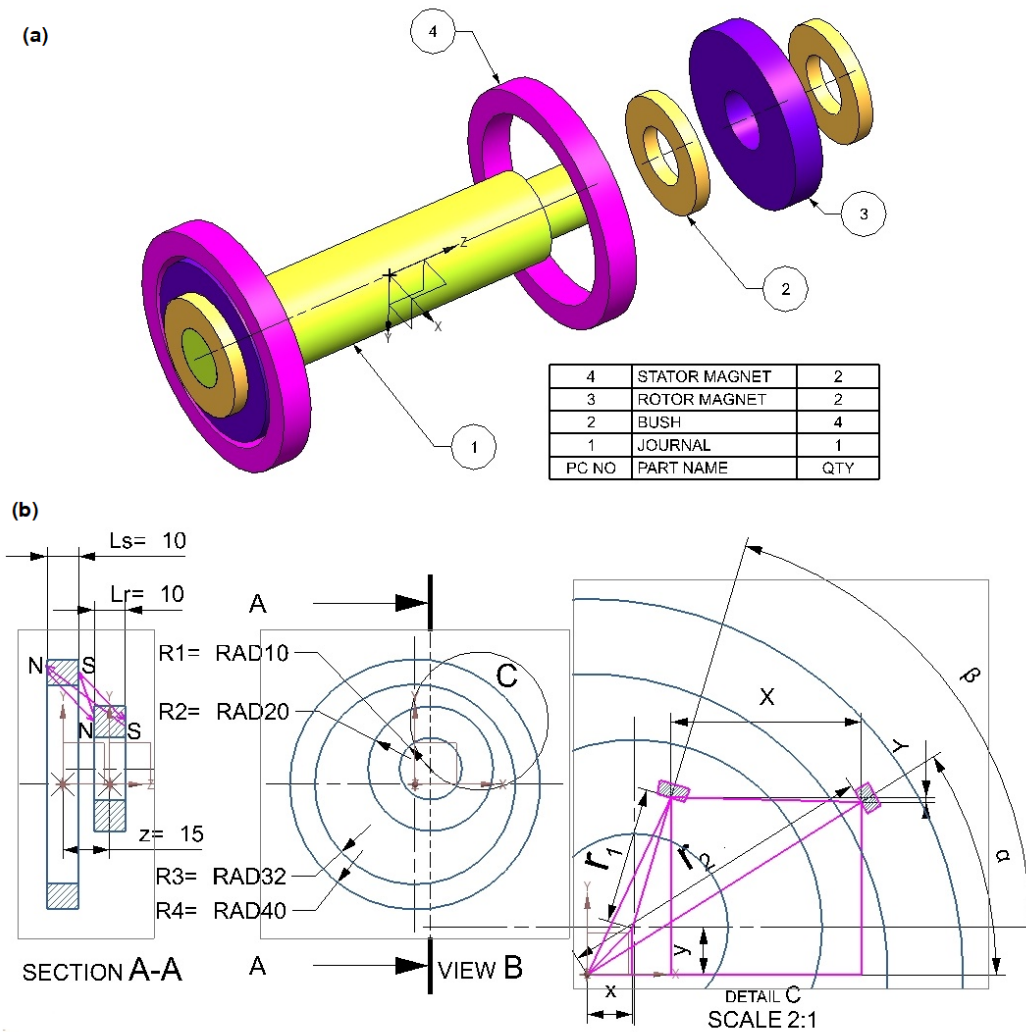


**Fig.14 a** Partial exploded view of permanent magnetic bearing set up, **b** A schematic representation for analytical derivation

### 5.2.2 General assumption and consideration

The following assumption is considered for the proposed model.

- i. Both stator and rotor magnet pair are axially magnetized ring magnet.
- ii. Stator magnets are aligned with the common bearing axis of fixed reference.
- iii. The magnet material is stiff, ferromagnetic and isotropic.
- iv. The present analysis is static.
- v. Demagnetization is not considered.
- vi. The shaft is rigid and massless.
- vii. The nominal mass of the rotor/ disc is considered for analysis.
- viii. A finite division approach has been taken care of for this method.

- ix. A combination of Riemann summation and triple integral is considered for fourth-dimensional integration.
- x. Flat surface magnetic charge density is considered constant over the flat surface of both magnets.
- xi. Horizontal X and vertical Y are radial directions, and the axial Z translation of the rotor magnet is considered for the analysis.
- xii. The rotors have a common angular spin velocity with respect to their axis, which is also aligned with the journal axis along the Z direction.
- xiii. The Columbian model for the evaluation of magnetic force is considered.

### 5.2.3 Columbian model of magnetic force

The magnetic force of the Columbian model described by Santra et al. [47-49] is rearranged below as

$$\overrightarrow{dF_{sr}} = \frac{\mu_0}{4\pi} \times \frac{q_s \times q_r}{r_{sr}^3} \overrightarrow{r_{sr}} \quad (31)$$

$$q_s = \sigma_s dS_s, q_r = \sigma_r dS_r, \sigma_r = \frac{Br_1}{\mu_0} \sigma_s = \frac{Br_2}{\mu_0} \quad (32)$$

$$dS_s = r_2 \times d\alpha \times dr_2, dS_r = r_1 \times d\beta \times dr_1 \quad (33)$$

$$\overrightarrow{dF_{sr}} = \frac{Br_1 \times Br_2}{4\pi\mu_0} \times \frac{r_1 r_2 dr_1 dr_2 d\alpha d\beta}{r_{sr}^3} \overrightarrow{r_{sr}} \quad (34)$$

The equation (34) also can be written in the following form.

$$\overrightarrow{dF_{sr}} = \frac{Br_1 \times Br_2}{4\pi\mu_0} \times \frac{A_r A_s}{r_{sr}^3} \overrightarrow{r_{sr}} \quad (34b)$$

$$\overrightarrow{dF_{sr}} = \frac{Br_1 \times Br_2}{4\pi\mu_0} \times \frac{A_r \times \delta^2 \times A_s \times \delta^2}{r_{sr}^3 \delta^3} \overrightarrow{r_{sr}} \delta \quad (34c)$$

$$\overrightarrow{dF_{sr}} = \frac{Br_1 \times Br_2 \times \delta^2}{4\pi\mu_0} \times \frac{A_r \times A_s}{r_{sr}^3} \overrightarrow{r_{sr}} \quad (34d)$$

Where,  $\alpha$  is angular displacement of stator small elemental area  $dS_s$  about stator axis measured from x axis (radian),  $\beta$  is angular displacement of rotor small elemental area  $dS_r$  about rotor axis measured from x axis (radian)

### 5.2.4 Non-dimensional approach of parameters

All parameters have been converted to non-dimensional ones by dividing by maximum radial clearance ( $\delta$ ). The maximum radial clearance ( $\delta$ ) is a geometric parameter of the rotor and the stator magnet, which is evaluated by subtraction of the outer radius of the rotor magnet ( $R_2$ ) from the inner radius of the stator magnet ( $R_3$ ). These two radii are also geometric parameters of the bearing system. From the sketch detail C of fig. 14b, we can write

$$u = x + r_1 \cos\beta - r_2 \cos\alpha \quad (35)$$

$$v = y + r_1 \sin\beta - r_2 \sin\alpha \quad (36)$$

$$z_1 = z + 0.5 \times (L_s + L_r) \quad (37)$$

$$z_2 = z - 0.5 \times (L_s + L_r) \quad (38)$$

$$z_3 = z + 0.5 \times (L_s - L_r) \quad (39)$$

$$z_4 = z - 0.5 \times (L_s - L_r) \quad (40)$$

Where  $u$ ,  $v$ ,  $z_1$ ,  $z_2$ ,  $z_3$  and  $z_4$  are relative displacements of rotor elemental area from that of stator one. Refer to the notations in the Nomenclature section of the thesis for further understanding.

Dividing the above equations (35 to 40) by maximum radial clearance ( $\delta = R_3 - R_2$ ), we have

$$\bar{u} = \bar{x} + \bar{r}_1 \cos \beta - \bar{r}_2 \cos \alpha \quad (41)$$

$$\bar{v} = \bar{y} + \bar{r}_1 \sin \beta - \bar{r}_2 \sin \alpha \quad (42)$$

$$\bar{z}_1 = \bar{z} + 0.5 \times (\bar{L}_s + \bar{L}_r) \quad (43)$$

$$\bar{z}_2 = \bar{z} - 0.5 \times (\bar{L}_s + \bar{L}_r) \quad (44)$$

$$\bar{z}_3 = \bar{z} + 0.5 \times (\bar{L}_s - \bar{L}_r) \quad (45)$$

$$\bar{z}_4 = \bar{z} - 0.5 \times (\bar{L}_s - \bar{L}_r) \quad (46)$$

Above parameters are non dimensionalized and represented with a bar ‘-‘above the usual notations.

Again, reference force in rotor and stator magnets is written as

$$F_{ref} = \frac{Br_1 \times Br_2 \times \delta^2}{4\pi\mu_0} \quad (47)$$

By dividing magnetic force along x-axis ( $F_x$ ) by reference force ( $F_{ref}$ ) we have non dimensionalized magnetic force

$$\bar{F}_x = \frac{F_x}{F_{ref}} \quad (48)$$

Assembling eqn. (48) for all combinations, Eq. (47) provides the fundamental basis for the reference force expression, while the non-dimensional expressions in Eqs. (48) and (49) are derived from Eqs. (31) to (34).

$$\bar{F}_x = \int_{\bar{R}_3}^{\bar{R}_4} \int_{\bar{R}_1}^{\bar{R}_2} \int_0^{2\pi} \int_0^{2\pi} \bar{r}_1 \times \bar{r}_2 \times \bar{u} \times \left[ \frac{-1}{(\bar{u}^2 + \bar{v}^2 + \bar{z}_1^2)^{\frac{3}{2}}} - \frac{1}{(\bar{u}^2 + \bar{v}^2 + \bar{z}_2^2)^{\frac{3}{2}}} + \frac{1}{(\bar{u}^2 + \bar{v}^2 + \bar{z}_3^2)^{\frac{3}{2}}} + \frac{1}{(\bar{u}^2 + \bar{v}^2 + \bar{z}_4^2)^{\frac{3}{2}}} \right] \times d\bar{r}_1 \times d\bar{r}_2 \times d\alpha \times d\beta \quad (49)$$

Similarly, we can get other non-dimensional forces  $\bar{F}_y$  and  $\bar{F}_z$  as

$$\bar{F}_y = \int_{\bar{R}_3}^{\bar{R}_4} \int_{\bar{R}_1}^{\bar{R}_2} \int_0^{2\pi} \int_0^{2\pi} \bar{r}_1 \times \bar{r}_2 \times \bar{v} \times \left[ \frac{-1}{(\bar{u}^2 + \bar{v}^2 + \bar{z}_1^2)^{\frac{3}{2}}} - \frac{1}{(\bar{u}^2 + \bar{v}^2 + \bar{z}_2^2)^{\frac{3}{2}}} + \frac{1}{(\bar{u}^2 + \bar{v}^2 + \bar{z}_3^2)^{\frac{3}{2}}} + \frac{1}{(\bar{u}^2 + \bar{v}^2 + \bar{z}_4^2)^{\frac{3}{2}}} \right] \times d\bar{r}_1 \times d\bar{r}_2 \times d\alpha \times d\beta \quad (50)$$

and

$$\bar{F}_z = \int_{\bar{R}_3}^{\bar{R}_4} \int_{\bar{R}_1}^{\bar{R}_2} \int_0^{2\pi} \int_0^{2\pi} \bar{r}_1 \times \bar{r}_2 \times \left[ \frac{-\bar{z}_1}{(\bar{u}^2 + \bar{v}^2 + \bar{z}_1^2)^{\frac{3}{2}}} - \frac{\bar{z}_2}{(\bar{u}^2 + \bar{v}^2 + \bar{z}_2^2)^{\frac{3}{2}}} + \frac{\bar{z}_3}{(\bar{u}^2 + \bar{v}^2 + \bar{z}_3^2)^{\frac{3}{2}}} + \frac{\bar{z}_4}{(\bar{u}^2 + \bar{v}^2 + \bar{z}_4^2)^{\frac{3}{2}}} \right] \times \bar{dr}_1 \times \bar{dr}_2 \times d\alpha \times d\beta \quad (51)$$

Since force from each bearing applied on journal is  $F_0$ , we can write non dimensional stiffness as

$$\bar{k}_{xx} = \frac{\delta}{F_0} \times k_{xx} \quad (52)$$

where  $(F_0/\delta)$  is reference stiffness.

Again,

$$k_{xx} = \frac{\partial F_x}{\partial x} \quad (53)$$

$$\text{or, } k_{xx} = \frac{F_{ref}}{\delta} \frac{\partial \bar{F}_x}{\partial \bar{x}} \quad (54)$$

$$\text{or, } k_{xx} = \frac{F_{ref}}{\delta} \times \bar{k}'_{xx} \quad (55)$$

$$\text{where } \bar{k}'_{xx} = \frac{\partial \bar{F}_x}{\partial \bar{x}}$$

$$\text{so, } \bar{k}_{xx} = \frac{F_{ref}}{F_0} \times \bar{k}'_{xx} \quad (56)$$

$$\text{since } k_{ref} = \frac{F_0}{\delta}$$

Again, non dimensional stiffness of second kind can be written in partial derivative form as

$$\bar{k}'_{xx} = \frac{\partial \bar{F}_x}{\partial \bar{u}} \frac{\partial \bar{u}}{\partial \bar{x}} \quad (57)$$

Therefore, using eqn. (41) and eqn. (49), we have

$$\bar{k}'_{xx} = \int_{\bar{R}_3}^{\bar{R}_4} \int_{\bar{R}_1}^{\bar{R}_2} \int_0^{2\pi} \int_0^{2\pi} \bar{r}_1 \times \bar{r}_2 \times \left\{ \frac{-1}{(\bar{u}^2 + \bar{v}^2 + \bar{z}_1^2)^{\frac{3}{2}}} - \frac{1}{(\bar{u}^2 + \bar{v}^2 + \bar{z}_2^2)^{\frac{3}{2}}} + \frac{1}{(\bar{u}^2 + \bar{v}^2 + \bar{z}_3^2)^{\frac{3}{2}}} + \frac{1}{(\bar{u}^2 + \bar{v}^2 + \bar{z}_4^2)^{\frac{3}{2}}} \right\} - 3\bar{u}^2 \times \left\{ \frac{-1}{(\bar{u}^2 + \bar{v}^2 + \bar{z}_1^2)^{\frac{5}{2}}} - \frac{1}{(\bar{u}^2 + \bar{v}^2 + \bar{z}_2^2)^{\frac{5}{2}}} + \frac{1}{(\bar{u}^2 + \bar{v}^2 + \bar{z}_3^2)^{\frac{5}{2}}} + \frac{1}{(\bar{u}^2 + \bar{v}^2 + \bar{z}_4^2)^{\frac{5}{2}}} \right\} \times \bar{dr}_1 \times \bar{dr}_2 \times d\alpha \times d\beta \quad (58)$$

Similarly other non-dimensional stiffnesses of second kind coefficients can be found as

$$\begin{aligned} \bar{k}'_{yy} = & \int_{\bar{R}_3}^{\bar{R}_4} \int_{\bar{R}_1}^{\bar{R}_2} \int_0^{2\pi} \int_0^{2\pi} \bar{r}_1 \times \bar{r}_2 \times \left[ \left\{ \frac{-1}{(\bar{u}^2 + \bar{v}^2 + \bar{z}_1^2)^{\frac{3}{2}}} - \frac{1}{(\bar{u}^2 + \bar{v}^2 + \bar{z}_2^2)^{\frac{3}{2}}} + \frac{1}{(\bar{u}^2 + \bar{v}^2 + \bar{z}_3^2)^{\frac{3}{2}}} + \right. \right. \\ & \left. \left. \frac{1}{(\bar{u}^2 + \bar{v}^2 + \bar{z}_4^2)^{\frac{3}{2}}} \right\} - 3\bar{v}^2 \times \left\{ \frac{-1}{(\bar{u}^2 + \bar{v}^2 + \bar{z}_1^2)^{\frac{5}{2}}} - \frac{1}{(\bar{u}^2 + \bar{v}^2 + \bar{z}_2^2)^{\frac{5}{2}}} + \frac{1}{(\bar{u}^2 + \bar{v}^2 + \bar{z}_3^2)^{\frac{5}{2}}} + \frac{1}{(\bar{u}^2 + \bar{v}^2 + \bar{z}_4^2)^{\frac{5}{2}}} \right\} \right] \times \\ & \bar{dr}_1 \times \bar{dr}_2 \times d\alpha \times d\beta \end{aligned} \quad (59)$$

$$\begin{aligned} \bar{k}'_{zz} = & \int_{\bar{R}_3}^{\bar{R}_4} \int_{\bar{R}_1}^{\bar{R}_2} \int_0^{2\pi} \int_0^{2\pi} \bar{r}_1 \times \bar{r}_2 \times \left[ \left\{ \frac{-1}{(\bar{u}^2 + \bar{v}^2 + \bar{z}_1^2)^{\frac{3}{2}}} - \frac{1}{(\bar{u}^2 + \bar{v}^2 + \bar{z}_2^2)^{\frac{3}{2}}} + \frac{1}{(\bar{u}^2 + \bar{v}^2 + \bar{z}_3^2)^{\frac{3}{2}}} + \right. \right. \\ & \left. \left. \frac{1}{(\bar{u}^2 + \bar{v}^2 + \bar{z}_4^2)^{\frac{3}{2}}} \right\} - 3 \times \left\{ \frac{-\bar{z}_1^2}{(\bar{u}^2 + \bar{v}^2 + \bar{z}_1^2)^{\frac{5}{2}}} - \frac{\bar{z}_2^2}{(\bar{u}^2 + \bar{v}^2 + \bar{z}_2^2)^{\frac{5}{2}}} + \frac{\bar{z}_3^2}{(\bar{u}^2 + \bar{v}^2 + \bar{z}_3^2)^{\frac{5}{2}}} + \frac{\bar{z}_4^2}{(\bar{u}^2 + \bar{v}^2 + \bar{z}_4^2)^{\frac{5}{2}}} \right\} \right] \times \bar{dr}_1 \times \\ & \bar{dr}_2 \times d\alpha \times d\beta \end{aligned} \quad (60)$$

$$\begin{aligned} \bar{k}'_{xy} = & \int_{\bar{R}_3}^{\bar{R}_4} \int_{\bar{R}_1}^{\bar{R}_2} \int_0^{2\pi} \int_0^{2\pi} 3 \times \bar{r}_1 \times \bar{r}_2 \times \bar{u} \times \bar{v} \times \left\{ \frac{1}{(\bar{u}^2 + \bar{v}^2 + \bar{z}_1^2)^{\frac{5}{2}}} + \frac{1}{(\bar{u}^2 + \bar{v}^2 + \bar{z}_2^2)^{\frac{5}{2}}} - \frac{1}{(\bar{u}^2 + \bar{v}^2 + \bar{z}_3^2)^{\frac{5}{2}}} - \right. \\ & \left. \frac{1}{(\bar{u}^2 + \bar{v}^2 + \bar{z}_4^2)^{\frac{5}{2}}} \right\} \times \bar{dr}_1 \times \bar{dr}_2 \times d\alpha \times d\beta \end{aligned} \quad (61)$$

$$\begin{aligned} \bar{k}'_{yz} = & \int_{\bar{R}_3}^{\bar{R}_4} \int_{\bar{R}_1}^{\bar{R}_2} \int_0^{2\pi} \int_0^{2\pi} 3 \times \bar{r}_1 \times \bar{r}_2 \times \bar{v} \times \left\{ \frac{\bar{z}_1}{(\bar{u}^2 + \bar{v}^2 + \bar{z}_1^2)^{\frac{5}{2}}} - \frac{\bar{z}_2}{(\bar{u}^2 + \bar{v}^2 + \bar{z}_2^2)^{\frac{5}{2}}} - \frac{\bar{z}_3}{(\bar{u}^2 + \bar{v}^2 + \bar{z}_3^2)^{\frac{5}{2}}} - \right. \\ & \left. \frac{\bar{z}_4}{(\bar{u}^2 + \bar{v}^2 + \bar{z}_4^2)^{\frac{5}{2}}} \right\} \times \bar{dr}_1 \times \bar{dr}_2 \times d\alpha \times d\beta \end{aligned} \quad (62)$$

$$\begin{aligned} \bar{k}'_{zx} = & \int_{\bar{R}_3}^{\bar{R}_4} \int_{\bar{R}_1}^{\bar{R}_2} \int_0^{2\pi} \int_0^{2\pi} 3 \times \bar{r}_1 \times \bar{r}_2 \times \bar{u} \times \left\{ \frac{\bar{z}_1}{(\bar{u}^2 + \bar{v}^2 + \bar{z}_1^2)^{\frac{5}{2}}} - \frac{\bar{z}_2}{(\bar{u}^2 + \bar{v}^2 + \bar{z}_2^2)^{\frac{5}{2}}} - \frac{\bar{z}_3}{(\bar{u}^2 + \bar{v}^2 + \bar{z}_3^2)^{\frac{5}{2}}} - \right. \\ & \left. \frac{\bar{z}_4}{(\bar{u}^2 + \bar{v}^2 + \bar{z}_4^2)^{\frac{5}{2}}} \right\} \times \bar{dr}_1 \times \bar{dr}_2 \times d\alpha \times d\beta \end{aligned} \quad (63)$$

Thus, all nine-dimensional and non-dimensional stiffness terms can be found by simple analytical differentiation. Also found that three pairs of corresponding non-dimensional cross-stiffness terms are equal as

$$\bar{k}_{xy} = \bar{k}_{yx}, \bar{k}_{yz} = \bar{k}_{zy}, \bar{k}_{zx} = \bar{k}_{xz} \quad (64)$$

and summation of diagonal non-dimensional stiffness terms is zero [115] as given

$$\bar{k}_{xx} + \bar{k}_{yy} + \bar{k}_{zz} = 0 \quad (65)$$



### 5.2.5 Calculation of natural frequency

Stiffness coefficients thus derived, used in force equation to find the natural frequencies. 3-DOF matrix equation is

$$\begin{bmatrix} m & 0 & 0 \\ 0 & m & 0 \\ 0 & 0 & m \end{bmatrix} \times \begin{bmatrix} \ddot{x} \\ \ddot{y} \\ \ddot{z} \end{bmatrix} + 2 \begin{bmatrix} k_{xx} & k_{xy} & k_{xz} \\ k_{yx} & k_{yy} & k_{yz} \\ k_{zx} & k_{zy} & k_{zz} \end{bmatrix} \times \begin{bmatrix} x \\ y \\ z \end{bmatrix} = \begin{bmatrix} 0 \\ 0 \\ 0 \end{bmatrix} \quad (66)$$

Assuming solution of x, y and z as follows

$$x = \phi_x e^{\omega t}, y = \phi_y e^{\omega t}, z = \phi_z e^{\omega t} \quad (67)$$

Putting the above the following is found as  $e^{\omega t} \neq 0, t > 0$

$$\omega^2 \begin{bmatrix} m & 0 & 0 \\ 0 & m & 0 \\ 0 & 0 & m \end{bmatrix} \times \begin{bmatrix} \phi_x \\ \phi_y \\ \phi_z \end{bmatrix} + 2 \begin{bmatrix} k_{xx} & k_{xy} & k_{xz} \\ k_{yx} & k_{yy} & k_{yz} \\ k_{zx} & k_{zy} & k_{zz} \end{bmatrix} \times \begin{bmatrix} \phi_x \\ \phi_y \\ \phi_z \end{bmatrix} = \begin{bmatrix} 0 \\ 0 \\ 0 \end{bmatrix} \quad (68)$$

$$\text{and } \begin{bmatrix} \phi_x \\ \phi_y \\ \phi_z \end{bmatrix} \neq 0 \quad (69)$$

Where,  $\phi_x$ ,  $\phi_y$  and  $\phi_z$ , are the amplitude of displacement along x, y and z axis (m) accordingly. m is the mass of the rotating system.

Hence, to find the natural frequency,

$$\begin{bmatrix} \omega^2 m + 2k_{xx} & 2k_{xy} & 2k_{zx} \\ 2k_{xy} & \omega^2 m + 2k_{yy} & 2k_{yz} \\ 2k_{zx} & 2k_{yz} & \omega^2 m + 2k_{zz} \end{bmatrix} = 0 \quad (70)$$

$$m^3 \omega^6 + 4m(k_{yy}k_{zz} - k_{xy}^2 - k_{yz}^2 - k_{zx}^2 - k_{xx}^2)\omega^2 + 24k_{xy}k_{yz}k_{zx} - 8(k_{xx}k_{yz}^2 + k_{yy}k_{zx}^2 + k_{zz}k_{xy}^2) = 0 \quad (71)$$

$$\text{Considering reference frequency [116] as } \omega_{ref} = \sqrt{\frac{2F_0}{m\delta}} \quad (72)$$

$$k_{xx} = \frac{F_{ref}}{2F_0} \times m\omega_{ref}^2 \bar{k}'_{xx} \quad (73)$$

$$\text{Let } \frac{F_0}{F_{ref}} = S \quad (74)$$

This non dimensional term S as a ratio between applied and reference force has a typical relation with other non-dimensional parameters as shown in equation (76).

$$\text{Therefore, } k_{xx} = \frac{1}{2S} \times m\omega_{ref}^2 \bar{k}'_{xx} \quad (75)$$

Similarly knowing other coefficient following expression can be formed

$$S^3\bar{\omega}^6 + S \times \left( \bar{k}'_{yy}\bar{k}'_{zz} - \bar{k}'_{xy}{}^2 - \bar{k}'_{yz}{}^2 - \bar{k}'_{zx}{}^2 - \bar{k}'_{xx}{}^2 \right) \bar{\omega}^2 + 3\bar{k}'_{xy}\bar{k}'_{yz}\bar{k}'_{zx} - \left( \bar{k}'_{xx}\bar{k}'_{yz}{}^2 + \bar{k}'_{yy}\bar{k}'_{zx}{}^2 + \bar{k}'_{zz}\bar{k}'_{xy}{}^2 \right) = 0 \quad (76)$$

The roots of the eqn. (76) have non-dimensional Eigen values. They are generally complex conjugate. Where,

$$\bar{\omega} = \bar{a}_r \pm i\bar{\omega}_r, \bar{a}_r = \frac{a_r}{\omega_{ref}}, \bar{\omega}_r = \frac{\omega_r}{\omega_{ref}} \quad (77)$$

where,  $r = 1, 2, 3$

For stability, non-dimensional coefficient that governs growth of vibration ( $\bar{a}_r$ ) < 0 and non-dimensional natural frequency ( $\bar{\omega}_r$ ) should be more than applied frequency [116].

### 5.2.6 Input consideration for radial force maximization

For finding maximum radial force, the inner radius of the rotor ring magnet, the outer radius of the stator ring magnet, maximum radial clearance, the same length of all rotor and stator magnet, the mass of the rotating system and external applied force on rotor have been taken as input for optimization. The residual flux density of magnets is also taken as input. The space limit in the X and Y directions is equal to positive radial clearance, and the same in the Z direction is equal to the positive axial end of the stator.

### 5.2.7 Algorithm for the solution

The non-dimensional space is discretised by  $N_x, N_y$  and  $N_z$  along X, Y and Z direction. The algorithm steps as follows in table 11.

Table 11 Algorithm for the proposed model

Steps	Details
1	Load value of the input parameters.
2	Initiate all non-dimensional global parameter.
3	Discretise all space coordinates within the interested limit.
4	Run a loop for the outer radius of the rotor where the inner radius of the stator, $\bar{R}_3 = 1 + \bar{R}_2$
5	Solve the non-dimensional force and stiffness using one iterated loop by Riemann summation followed by the nested triple integral tool in any software like the integral3 function using equations (58 to (63).

- 6 Store the maximum values for a particularly interesting position in space boundary by comparing forces among different outer radii of the rotor and the inner radius of the stator. This radius searching may be adopted by any suitable method like the "coordinate descent method". Store the related concern outer radius of the rotor and the inner radius of the stator for which the maximum value is obtained.
- 7 Store the maximum values of forces and stiffness for various discretised space zone.
- 8 Plot all forces and stiffness for the interested space zones.

### 5.2.8 Input parameters

Following input parameters are chosen to run the program for the above algorithm in the following table 12, table 13 and table 14.

Table 12 Data used for force validation

Input parameters	Values (In SI units)
Inner radius of the rotor ring magnet	0.005
Outer radius of the rotor ring magnet	0.024
Inner radius of the stator ring magnet	0.025
Outer radius of the stator ring magnet	0.050
Length of the rotor magnet/ stator magnet	0.032 / 0.030
Mass of the rotor system	8
Load on journal/ bearing	40
Residual flux density of magnets	1.0 & 1.2
Absolute magnetic permeability	$4\pi \times 10^{-7}$

Table 13 Data used for axial stiffness validation

Input parameters	Values (In SI units)
Inner radius of the rotor ring magnet	0.021
Outer radius of the rotor ring magnet	0.024
Inner radius of the stator ring magnet	0.025
Outer radius of the stator ring magnet	0.028
Length of the rotor magnet/ stator magnet	0.003

Mass of the rotor system	8
Load on journal/ bearing	40
Residual flux density of magnets	1.0, 1.0
Absolute magnetic permeability	$4\pi \times 10^{-7}$

Table 14 Data used for radial stiffness validation

Input parameters	Values (In SI units)
Inner radius of the rotor ring magnet	0.010
Outer radius of the rotor ring magnet	0.020
Inner radius of the stator ring magnet	0.022
Outer radius of the stator ring magnet	0.032
Length of the rotor magnet/ stator magnet	0.010 / 0.010
Mass of the rotor system	8
Load on journal/ bearing	40
Residual flux density of magnets	1.0 & 1.0
Absolute magnetic permeability	$4\pi \times 10^{-7}$

### 5.3 Validation of the proposed model

Almost all of the available reference data are in image format. Hence to extract the force or stiffness distribution data numerically, the available image information is converted to matrix data format using the any image viewer. In this matrix format, the data are in pixel units. Origin position and axes position data from the available plot are also extracted. After that, the pixel unit is converted to an axes label unit in horizontal and vertical directions. These processed data are taken for validation with the proposed model data statistically and graphically. These are shown in fig. 15, fig. 16, fig. 17 and fig. 18. The relative error of a parameter has been calculated by subtracting the value of the same parameter of the proposed model from the same reference data. The relative error is multiplied by 100 and divided by the reference data to get the relative percentage error. All the calculated relative error is fitted using the normal distribution to obtain the population mean and standard deviation. This information helps to quantify the validation statistically.

#### 5.3.1 Theoretical validation for axial force and stiffness

Ravaud et al. [33-35] and Lemarquand and Lemarquand [37] have shown the axial force

variation over axial position with the same relevant input data of table 13. Axial force data concerning axial position has been extracted from the reference plot image given by Lemarquand and Lemarquand [37] and linked with the relevant input parameter of table 13. The same has been calculated using the proposed model. Using normal distribution population mean of relative error is calculated as 0.45%, and the standard deviation is 1.75% approximately. With the fitted normal distribution mean relative error of axial force using the proposed model over the reference model is found between -1.34% to 2.24%, approximately with a 99.97% confidence level. The axial force is validated by the above statistically, and a comparison is also shown in fig. 15.

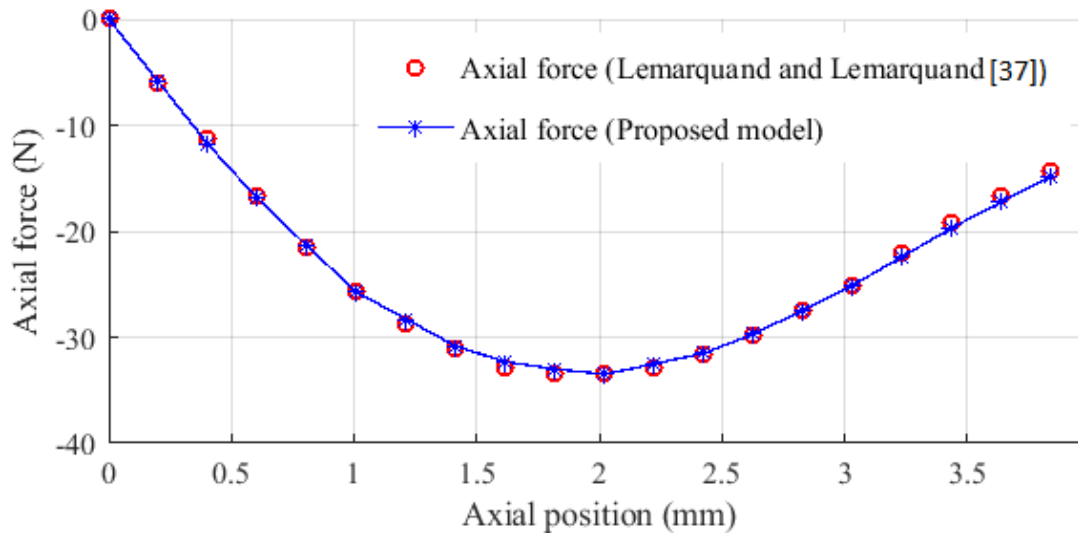


**Fig. 15** Comparison of axial force computed by proposed model and ref. Lemarquand and Lemarquand [37]

The variation of axial force to the relative axial position of the rotor in the reported and proposed model is very close in fig. 15, and most of the zone is overlapped.

Lemarquand and Lemarquand [37] have shown the axial stiffness variation over axial position with the same relevant input data of table 13. Axial stiffness data for the axial position has been extracted from the reference plot image, as shown by Lemarquand and Lemarquand [37], linked with the relevant input parameter of table 13. The same has been calculated using the proposed model. Using normal distribution population mean of relative error is calculated as -1.21% and the standard deviation as 2.08% approximately. With the fitted normal distribution mean relative error of axial stiffness using the proposed model over the reference model is found between -3.27% to 0.84%, approximately with a 99.97% confidence level. The axial stiffness is validated by the above statistically, and the comparison result is also shown in fig. 16. Here also, the results are close.

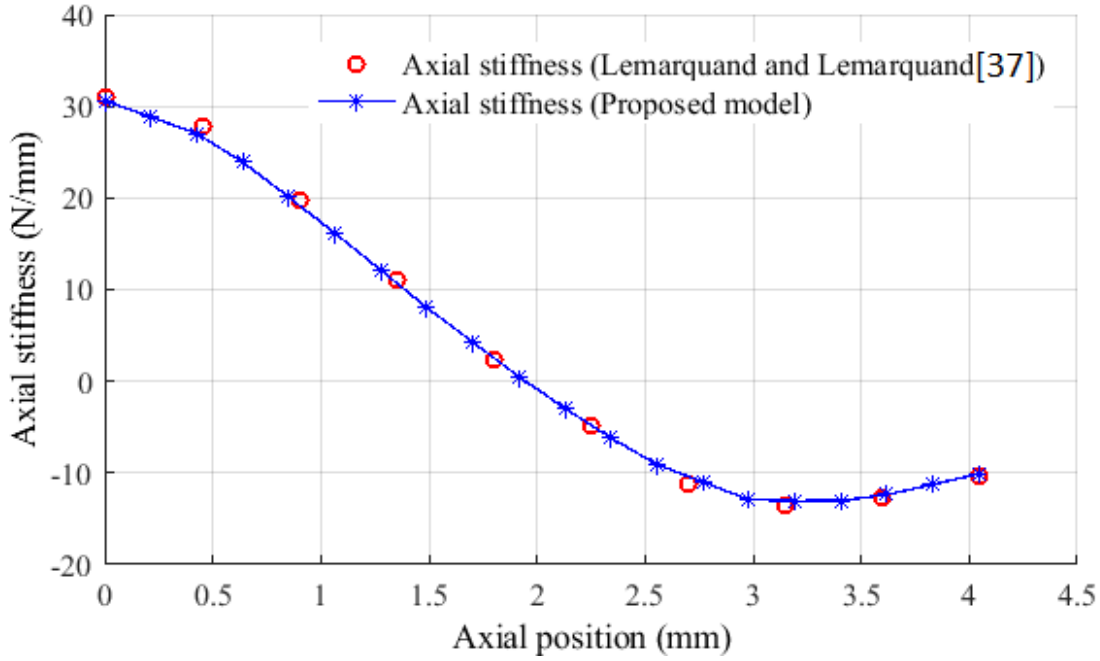


**Fig. 16** Comparison of axial stiffness computed by proposed model and ref. Lemarquand and Lemarquand [37]

### 5.3.2 Theoretical validation for radial force and stiffness

Muzakkir et al. [26] have shown the radial force variation over radial position with the same relevant input data of table 12. Radial force data with respect to radial position has been extracted from the reference plot image, as shown by Muzakkir et al. [26], linked with the relevant input parameter of table 12. The same has been calculated using the proposed model also. Using normal distribution population mean of relative error is calculated as 0.12%, and the standard deviation is 0.70% approximately. With the fitted normal distribution mean relative error of radial force using the proposed model over the reference model is found between -0.57% to 0.81%, approximately with a 99.97% confidence level. The radial force is validated by the above statistically, and the comparison result is shown in fig. 17.

Non-dimensional radial force variation is shown and validated in fig. 17, where radial force looks almost linearly varying with the radial eccentricity position. Here also, it is clearly observed that lines showing the variation of radial force with respect to the radial eccentricity of the rotor in reported, and the proposed model is very close in fig. 17, and most of the zone it is overlapped. Bekinal et al. [38] have shown the radial stiffness variation over radial position with the same relevant input data of table 14. Radial stiffness data concerning radial position has been extracted from the reference plot image, as shown by Bekinal et al. [38], linked with the relevant input parameter of table 14. The same has been calculated using the proposed model also. Using normal distribution population mean of relative error is calculated as 3.27%, and the standard deviation is 2.00% approximately.

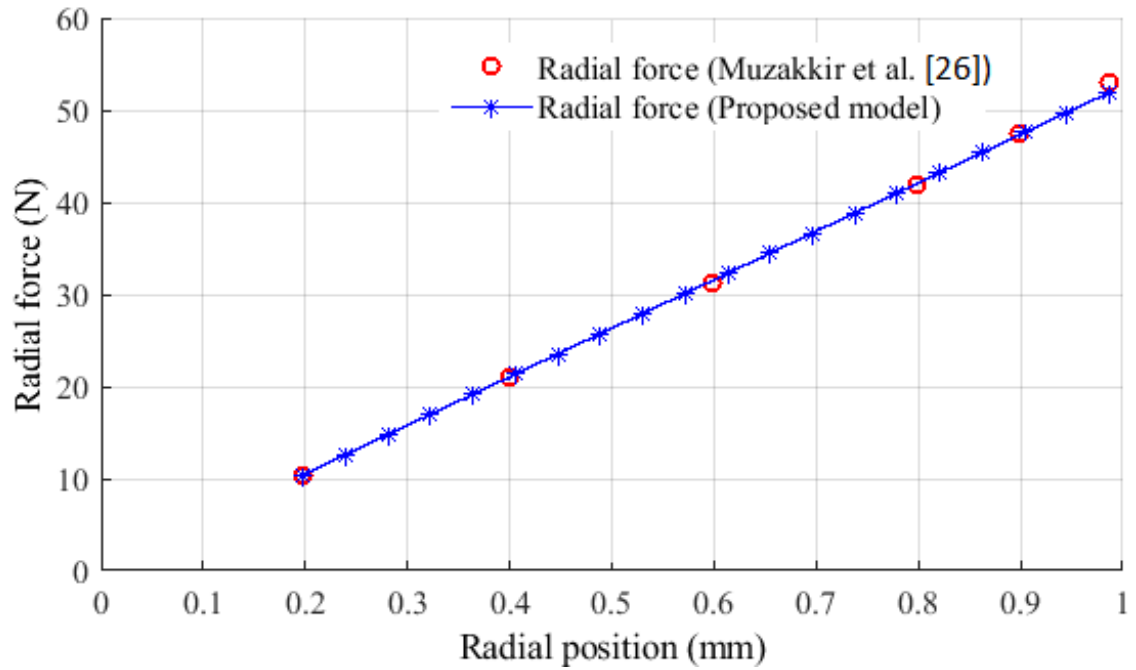


**Fig. 17** Comparison of radial force computed by proposed model and ref. Muzakkir et al. [26]

With the fitted normal distribution mean relative error of radial stiffness using the proposed model over the reference model is found between 1.30% to 5.24%, approximately with a 99.97% confidence level. The radial stiffness is validated by the above statistically, and the comparison result is also shown in fig. 18. Here, the radial stiffness parameter's error is higher than other parameters.

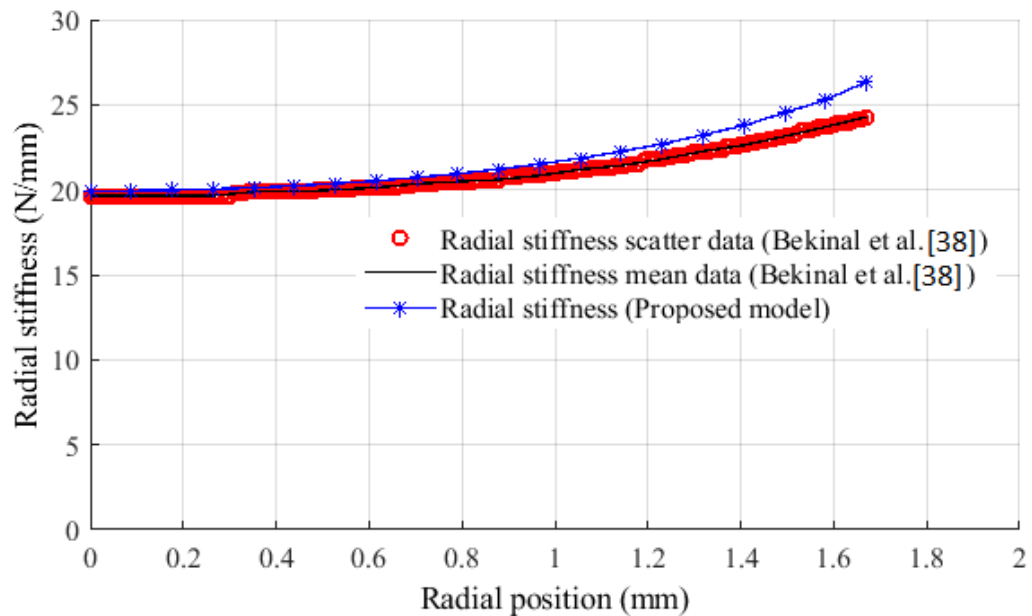


**Fig. 18** Comparison of radial stiffness computed by proposed model and ref. Bekinal et al. [38]

## 5.4 Simulation of non-dimensional proposed model

The non-dimensional analysis is carried out with the input parameter of table 13.

### 5.4.1 Non-dimensional force variation

Contour plots of non-dimensional forces are shown in fig. 19 and fig. 20 in ranges of the interested zone. The absolute force can be computed by multiplying the reference force with the non-dimensional force value obtained from the graph for a particular axial and radial eccentric location.

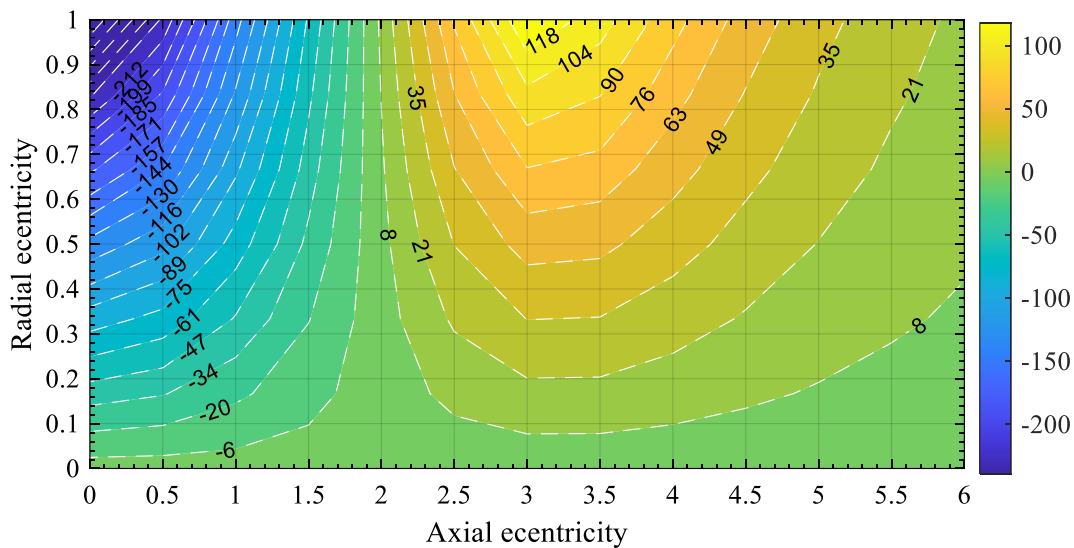


**Fig. 19** Contour plot of non-dimensional radial force

Fig. 19 shows that radial repulsive force has a considerably high value at zero axial eccentricity. The eccentric position is near the stator inner wall (Radial eccentricity equals 1). Here, radial eccentricity and forces experienced by rotor magnets are considered positive along the positive direction of the x-axis. So, the opposing force is directed towards the negative x-axis, trying to move the rotor magnet away from the proximity of the inner wall of the stator magnet, and it is repulsive. At axial eccentricity greater than 1.9, the force direction changes to a positive one, pulling the rotor towards the stator magnet. This attractive force is higher at a higher value of radial eccentricity.



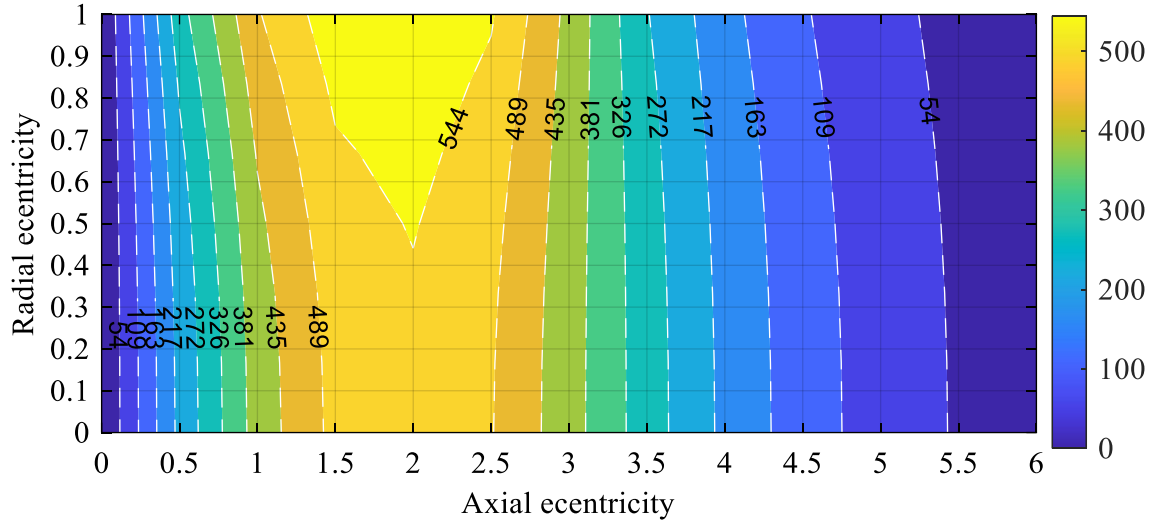


**Fig. 20** Contour plot of non-dimensional axial force

Fig. 20 shows the maximum value of axial force at non-dimensional axial eccentricity around 2. The reason is that the repulsive force (here, force along the positive z-axis) is more than that of other places. Further, more axial force components between the rotor and stator pole surfaces are in the same direction. When rotor magnets pass away axial eccentricity value 3, overall, two of such axial force components change the direction. Thus, it reduces effective axial force drastically.

#### 5.4.2 Non-dimensional stiffness variation

Non-dimensional stiffnesses in a different plane of interested space are shown in fig. 21 to 24. Four non-dimensional stiffnesses,  $K_{xx}$ ,  $K_{yy}$ ,  $K_{zz}$  and  $K_{zx}$ , dominate as x and y-axes are symmetric due to the consideration of a complete circular ring for the proposed model. Thus considering  $y=0$ , in 2D space of x and z axes,  $K_{xy}$  and  $K_{yz}$  are obtained zero value for every position of that 2D region as seen in fig. 25 and 26.

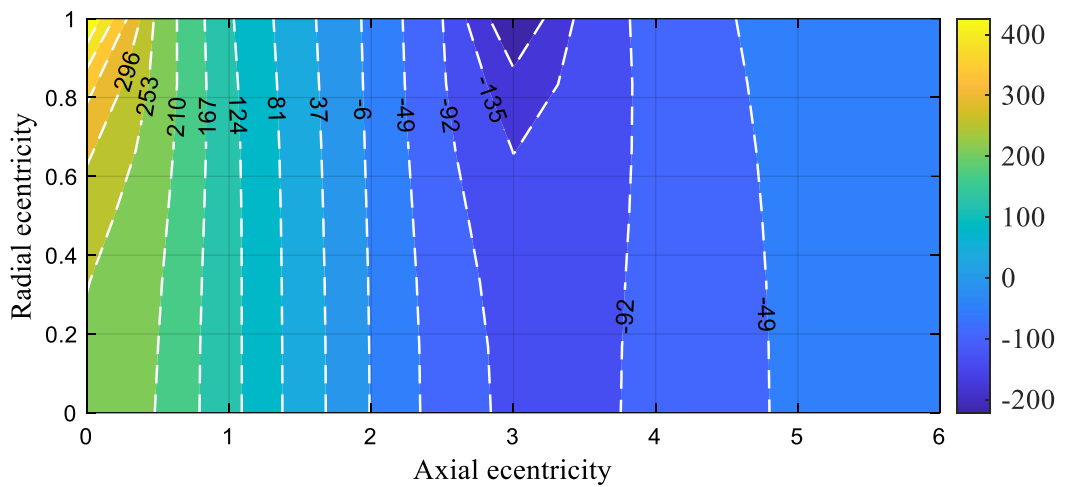


**Fig. 21** Contour plot of non-dimensional stiffness ( $K_{xx}$ )

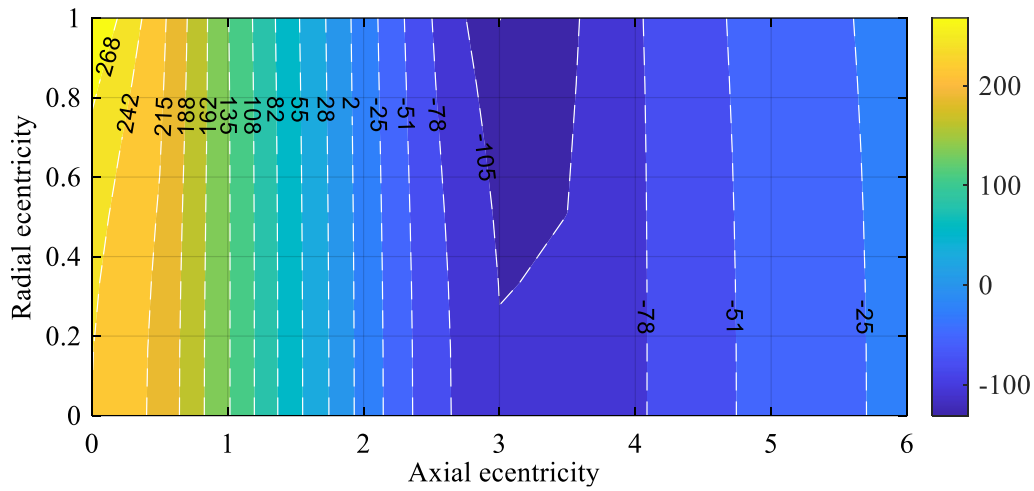


**Fig. 22** Contour plot of non-dimensional stiffness ( $K_{yy}$ )

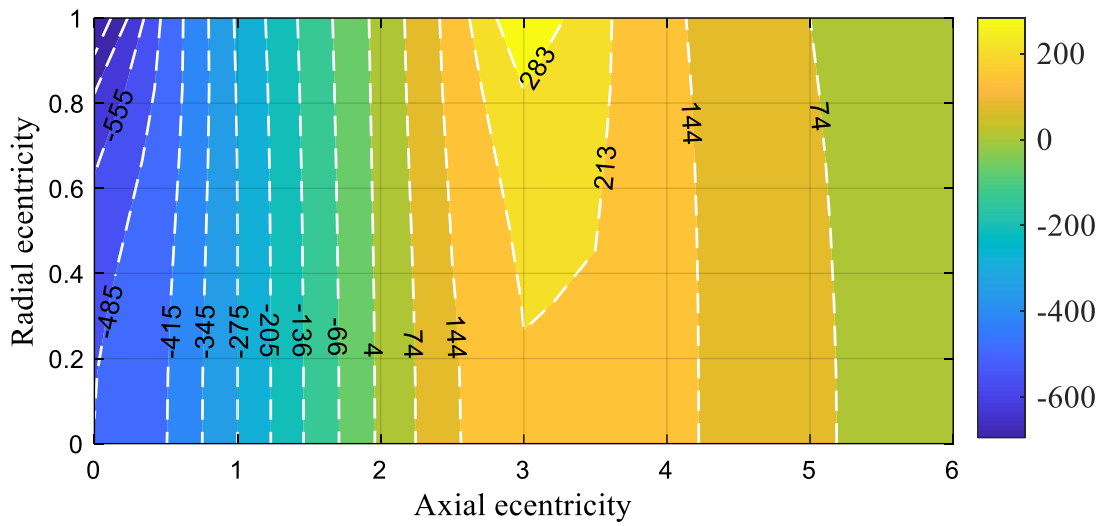


**Fig. 23** Contour plot of non-dimensional stiffness ( $K_{zz}$ )

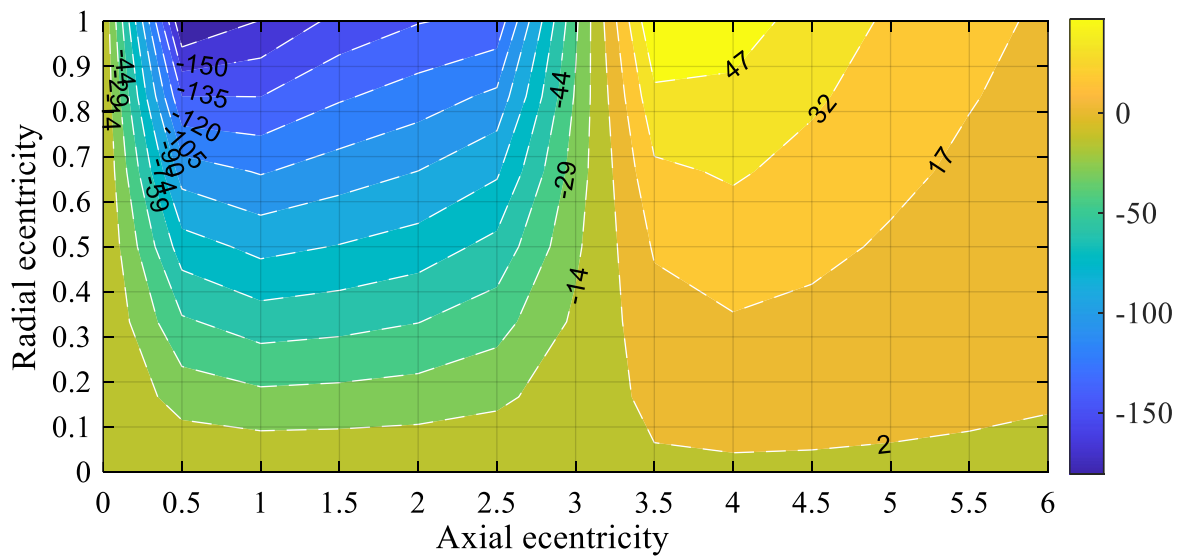


**Fig. 24** Contour plot of non-dimensional stiffness ( $K_{zx}$ )

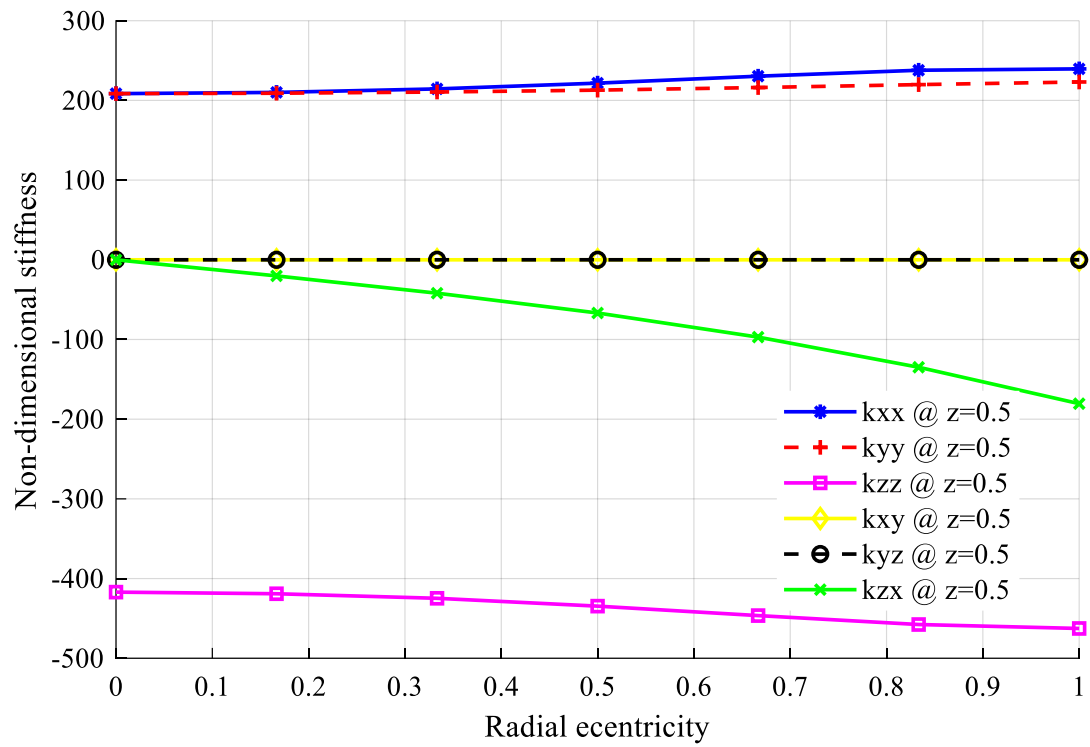


**Fig. 25** Plot of non-dimensional stiffness v/s radial eccentricity at particular axial eccentricity position

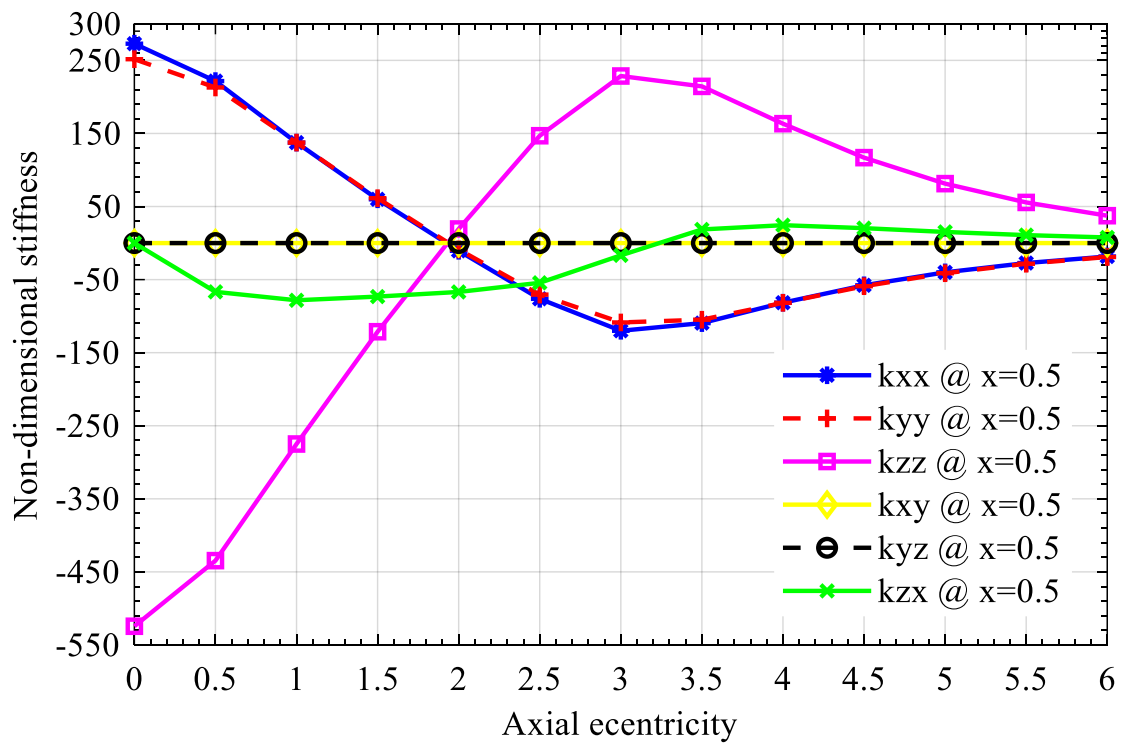


**Fig. 26** Plot of non-dimensional stiffness v/s axial eccentricity at particular radial eccentricity position

### 5.4.3 Stability analysis

The static stability is not found here as radial, and axial stiffness is opposite in sign, as seen in fig. 21, 23, 25 and 26. Hence when radial stability is achieved, the axial stability loses and vice versa [49].

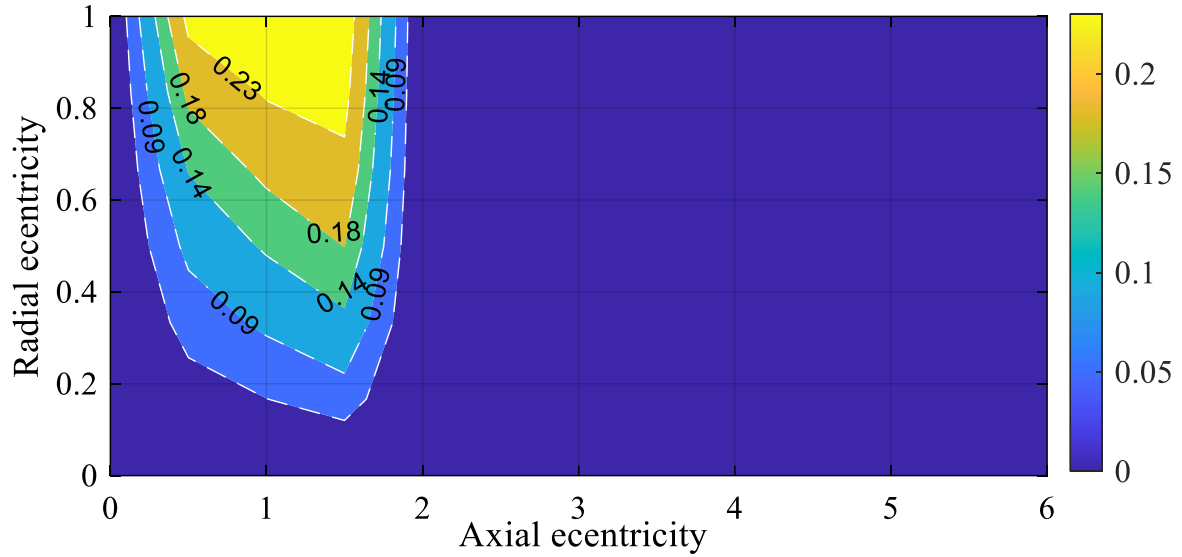


**Fig. 27** Contour plot of non-dimensional 2<sup>nd</sup> mode natural frequency

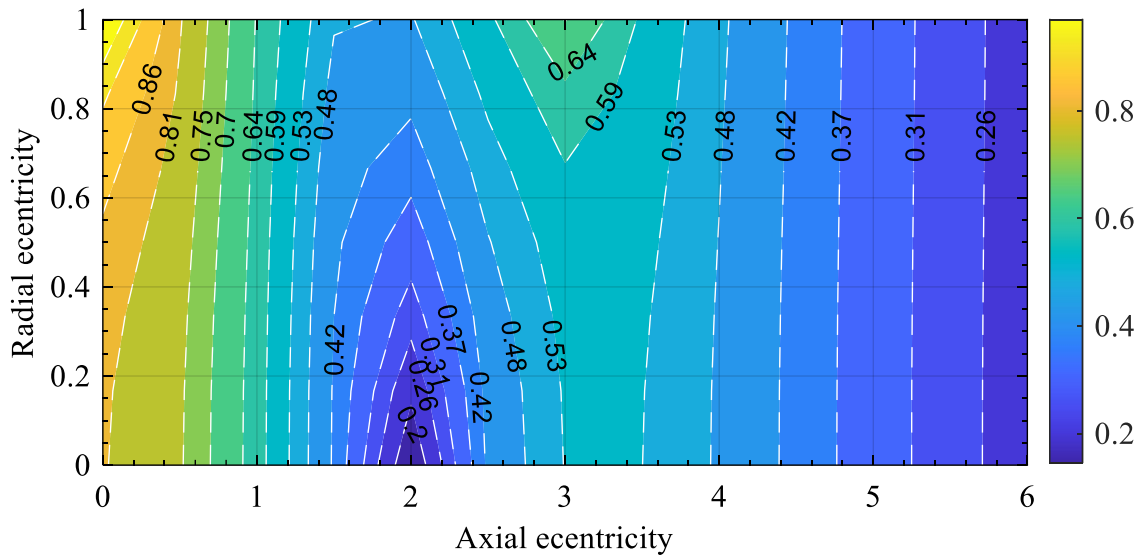


**Fig. 28** Contour plot of non-dimensional 3<sup>rd</sup> mode natural frequency

The stability plots are shown in terms of variation of non-dimensional natural frequency with the variation of the non-dimensional angular velocity of the rotor. The first mode of non-dimensional natural frequency is zero at all places. The second and third modes of non-dimensional natural frequency are shown in fig. 27 and fig. 28. If the rotor is supported by rigid axial support with a high stiffness value, stability may be observed at radial and axial eccentricity of 0.8. Near this point, the minimum of modal

frequencies shows a high value in fig. 27 and fig. 28. Due to the high rigid support assumption, the first mode of natural frequency also would be very high at the same point.

#### 5.4.4 Optimization results

For finding maximization of radial forces at zero axial position, the input and output parameters are shown in table 15 and table 16 accordingly.

Table 15 Data used for optimization

Input parameters	Values (In SI units)
Inner radius of the rotor ring magnet	0.010
Outer radius of the stator ring magnet	0.040
maximum radial clearance	0.002
Length of the rotor magnet/ stator magnet	0.010
Residual flux density of magnets	1.0, 1.0
Absolute magnetic permeability	$4\pi \times 10^{-7}$

Table 16 Optimization results

Output parameters	Values (In SI units)
Outer radius of the rotor ring magnet	0.030
Inner radius of the stator ring magnet	0.032

This simple optimization results from one kind of iterative method and incrimination of radius per iteration after completing the fourth-dimensional integration of radial force as per Eqn. (19) and a portion of the algorithm of Table 11 gives the idea of stator and rotor optimum size. The iterative technique used here is the coordinate descent method.

### 5.5 Summary

This chapter presents the simplest method of non-dimensional modelling using a simple permanent magnetic bearing configuration. This model is axially unstable, but it can be stable if axial outwards motion is restricted at the end of the journal with some axial shift by frictionless ball contact support to balance axial magnetic force. Non-dimensional value of parameters is more generalized than that of parameters analyzed by assuming specific dimensional values. The feasibility of actual dimensional parameters for permanent magnetic bearing design can be decided using the formula of

reference parameters as per Eqn. (17) and (42), as well as the corresponding value of non-dimensional parameters. The yellow zone of the second mode of non-dimensional natural frequency in fig. 27 is also valuable information to the designer where the radial stability reaches the maximum as the second mode of non-dimensional natural frequency has the maximum value here. The algorithm covers one proper non-dimensional optimization of radial magnetic force. The algorithm does not consider probabilistic approaches like the Monte Carlo Integration method. Hence, the simulation results have deterministic information. Examples simulated in this work act as an initial guideline for permanent magnetic design. The knowledge gained from Chapter 5 has been transferred to Chapter 6 for further exploration of the second and third objectives of the research.

## 6. Semi-analytical FEM approach for studying 6-DOF PMB

In the extension of Chapter 5, Chapter 6 presents a new approach using FEM to calculate the force and moment on a permanent magnet bearing. In this chapter, we used a typically new semi-analytical finite element approach to calculate the force and moment of permanent magnet bearing (PMB) in this work. PMB stator and rotor consist of ring-type cylindrical magnets having an axial magnetization. This work focuses on the characterization of magnetic moment, stiffness matrix, model validation and comparisons of the moment with other simulating software. This work also explains how PMB's angular stiffness or resisting magnetic moment improves with the rotor's change of magnet length and positional shift.

### 6.1 Introduction

The chapter presents an innovative semi-analytical finite element approach to estimate the force and moment for a single pair of axially magnetized ring-type permanent magnet bearings. A sensitivity study with this method and algorithm handles the accuracy and computation performance of the calculation. Further, a designer can adopt any optimization algorithm in the following explained model of the repulsive type PMB to characterize according to application requirements. Moreover, the scripting of the proposed algorithm allows it to couple with any physical interface around the spatial boundary of the bearing so that analysis may be carried out to study stability in the presence of active or passive interaction due to viscous damping.

All six degrees of freedom (6-DOF) are considered to extend our previous work [53]. Here, the complete 6 degrees of freedom means three orthogonal axes X, Y, and Z translation orientation and three tilting orientations about those three axes.

### 6.2 Details of the proposed model

We present the details of the proposed model with the schematic diagram, a mathematical model with a different approach of computation strategy and algorithm to address the simulation of the stiffness matrix of 6-DOF passive magnet bearing.

#### 6.2.1 Schematic of passive magnetic bearing

A single pair of cylindrical permanent magnets (Fig.29) are considered for the analysis. Both magnets of the stator and rotor are hollow and cylindrical type. These magnets have axially similar polarization. The outer part is the stator magnet kept fixed with the PMB base. The inner magnet can be attached co-axially with the flexible cylindrical shaft.  $R_{so}$  and  $R_{si}$  are the outer and inner radius of the stator magnet respectively.

Similarly,  $R_{ro}$  and  $R_{ri}$  are the outer and inner radius of the rotor magnet.  $L_s$  and  $L_r$  are the length of the stator and rotor magnet.

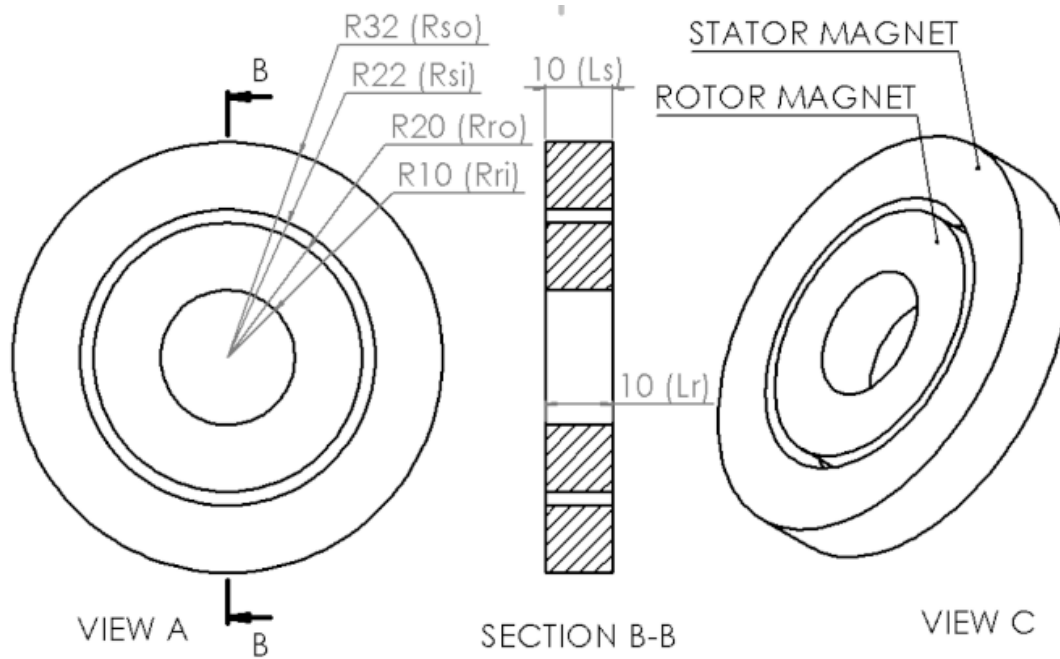


Fig. 29. Schematic of PMB rotor and stator magnet

### 6.2.2 Mathematical model

The expression of magnetic force components follows the Columbian model with constant isotropic and homogeneous magnetostatics surface charge density [32, 35, 39, 40, 60, 61]. The magnet's remanence and coercivity properties are assumed to have negligible impact. Hence, demagnetization during repulsive magnetic force interaction has negligible influence on the nearby rotor and stator finite elements. The structural stiffness of the magnets and shaft is assumed to be very high to consider the finite element as rigid. The rotor magnet and the shaft have fixed joints, so there is no relative displacement between them. 3D vector space in a right-angled Cartesian coordinate system presents the force components. The cross-sectional area of the rotor and stator magnet has meshed with the triangular shape finite elements, as shown in Fig. 30. Hence, all such elements of the rotor and stator magnets have the shape of right-angled prism geometry with a triangular cross-section. The prism elements' length is equal to those magnets' axial lengths. Both side triangular areas of the prism elements are assumed to have the same quantity of magnetic charge but opposite in sign. The total charge of each small triangular prism magnet is assumed to have an equivalent point source charge that lies at the centroid of the triangular area.



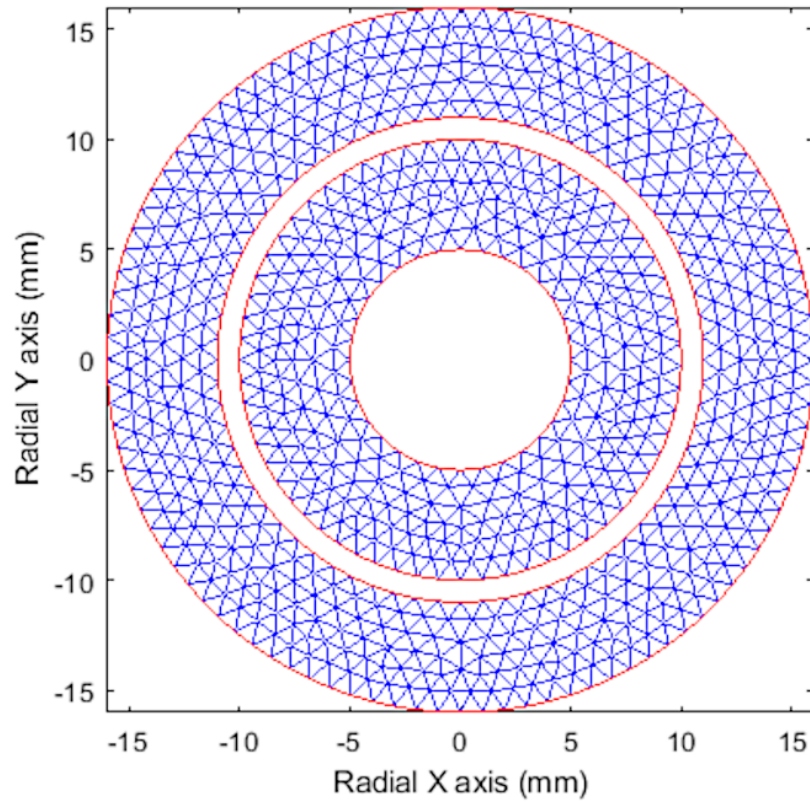


Fig. 30. Triangular mesh plot of magnets

The vector summation of forces of all combinations between stator and rotor finite elements represents the force given by the stator magnet on the rotor magnet. The rotor magnet's moment is about the rotor magnet's geometrical centre. Hence, the positional vectors of all such magnetic point charges become the relative positional vectors after subtracting the position vector of the rotor geometric centre.

The moment vector of the rotor magnet is calculated by vector summation of moments obtained using the cross product of the relative positional vector of the rotor triangular element and force vector applied on it due to stator elemental charge with all combinations.

The present model considers three translational ( $x$ ,  $y$ , and  $z$ ) and three angular ( $\alpha$ ,  $\beta$ , and  $\gamma$ ) degrees of freedom of rotor magnet. The orientation angles of the cylindrical rotor magnet axis are represented as  $\alpha$ ,  $\beta$ , and  $\gamma$ . They are measured on  $YZ$ ,  $ZX$ , and  $XY$  planes anticlockwise about the  $X$ ,  $Y$ , and  $Z$ -axis accordingly. The stator has a global coordinate system  $XYZ$ . The cylindrical axis of the stator magnet is considered global  $Z$ -axis. The global axes are orthogonal to each other. The  $X$ -axis and component of the parameter along this axis in this work are assumed as radial only, while the centroid of the rotor magnet lies on the  $XZ$  plane. The directional cosine angles of the positional vectors are considered as  $\phi_x$ ,  $\phi_y$  and  $\phi_z$  for global axis  $X$ ,  $Y$  and  $Z$  accordingly as shown in Fig. 31. Generally, all these angles hold the relationship as per (1).

$$\tan(\alpha)\tan(\beta)\tan(\gamma) = 1 \quad (78)$$

These angles also have relationship with cosine of axis angles (l, m and n) shown on (79)-(81). All angles are shown in Fig. 31.

$$l = \frac{1}{\sqrt{1+(\tan(\gamma))^2+(\cot(\beta))^2}} = \cos(\Phi_x) \quad (79)$$

$$m = \frac{1}{\sqrt{1+(\tan(\alpha))^2+(\cot(\gamma))^2}} = \cos(\Phi_y) \quad (80)$$

$$n = \frac{1}{\sqrt{1+(\tan(\beta))^2+(\cot(\alpha))^2}} = \cos(\Phi_z) \quad (81)$$

$$\text{Where, } l^2 + m^2 + n^2 = 1 \quad (82)$$

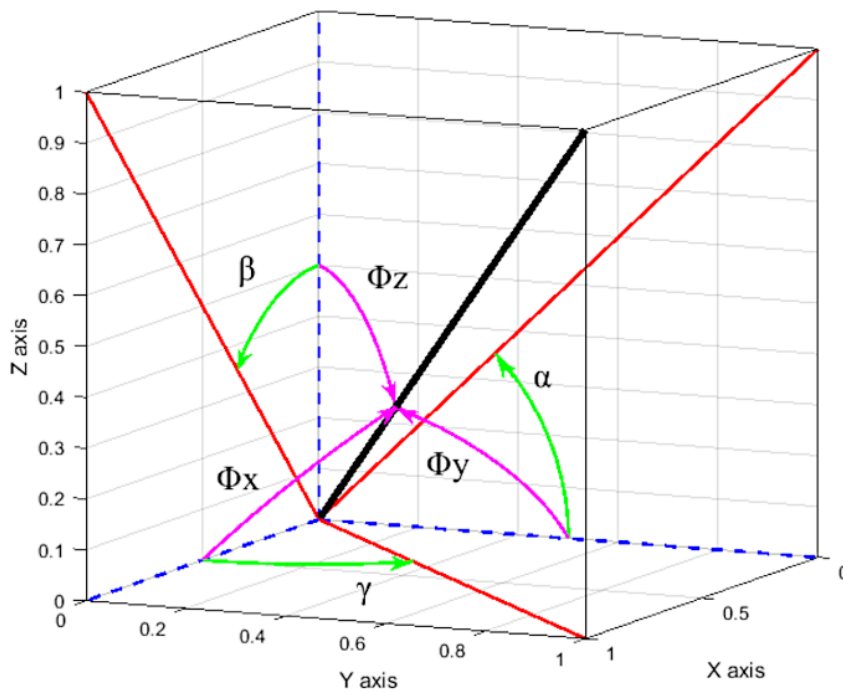


Fig. 31. Orientation of axis angles and projection angles

Initially, the rotor axis is parallel to the fixed stator axis. It is considered that the rotor axis has taken a typical orientation as per Fig. 31. Orientation angles of the rotor magnet axis will help configure the rotation matrix. The black line shown in Fig. 31 can be assumed the rotor magnet axis here. Another spin rotation angle may be considered to configure the final rotation matrix. Here we rotate the local coordinate system about the local Y-axis with  $\beta$  angle. Then rotate about immediate X-axis with  $(0.5\pi - \phi_y)$  angle and finally rotation as spin angle  $\lambda$  about next immediate Z-axis. Thus, the rotation matrix will be as per equation (83).

$$R_{LtoG} = \text{roty}(\beta) \times \text{rotx}\left(\frac{\pi}{2} - \phi_y\right) \times \text{rotz}(\lambda) \quad (83)$$

Here, rotation about Y axis,

$$roty(\beta) = \begin{bmatrix} \cos\beta & 0 & \sin\beta \\ 0 & 1 & 0 \\ -\sin\beta & 0 & \cos\beta \end{bmatrix} \quad (84)$$

rotation about X axis,

$$rotx\left(\frac{\pi}{2} - \varphi_y\right) = \begin{bmatrix} 1 & 0 & 0 \\ 0 & \cos\left(\frac{\pi}{2} - \varphi_y\right) & -s \in \left(\frac{\pi}{2} - \varphi_y\right) \\ 0 & \sin\left(\frac{\pi}{2} - \varphi_y\right) & \cos\left(\frac{\pi}{2} - \varphi_y\right) \end{bmatrix} \quad (85)$$

rotation about Z axis,

$$rotz(\lambda) = \begin{bmatrix} \cos\lambda & -\sin\lambda & 0 \\ \sin\lambda & \cos\lambda & 0 \\ 0 & 0 & 1 \end{bmatrix} \quad (86)$$

And  $\phi_y$  can be estimated from equation (78) and (80) with following sign corrected equation (10)

$$\phi_y = \cos^{-1} \frac{sh}{\sqrt{(1+(\tan(\alpha))^2 + (\tan(\alpha)\tan(\beta))^2)}} \quad (87)$$

Here,

$$sh = \text{signoftan}(\alpha) \quad (88)$$

The rotation matrix can also be found when the local coordinate axes component is considered an input concerning the global coordinate system. Hence, three unknown angles will be required, like  $\alpha$ ,  $\beta$ , and  $\lambda$ , to find the rotation matrix for transforming local to global orientation system.

The rotation matrix is pre-multiplied to all rotor elemental magnetic charge positional vectors and added to the linear translation positional vector. Thus, the final oriented position of the rotor element is achieved for the global coordinate system, as mentioned below.

$$\vec{p}_r = R_{LtoG} \times \begin{bmatrix} x_R \\ y_R \\ z_R \end{bmatrix} + \begin{bmatrix} x_{rc} \\ y_{rc} \\ z_{rc} \end{bmatrix} \quad (89)$$

Where,  $x_{re}$ ,  $y_{re}$ , and  $z_{re}$  are rotor local Cartesian coordinates of rotor element position.  $x_{rc}$ ,  $y_{rc}$ , and  $z_{rc}$  indicate centroid of rotor magnet concerning global coordinates.  $R_{LtoG}$  is the rotation matrix for converting the vector parameter to the global coordinate system from the local rotor coordinate system. The centroid of the stator magnet is considered to the global origin O as shown in Fig. 32. The force vector is expressed in global coordinate reference system where stator geometric center is at the location of global origin. The magnetic moment vector is evaluated about the rotor geometric center with

the same reference frame of global orientation. The externally moment and force load applied on the rotor center can be directly used as an equilibrium matrix equation due to the generic consideration of rotor centroid for magnetic moment evaluation. The rotor magnet also has a local coordinate reference frame as  $X_1Y_1Z_1$  with origin  $O_1$ . They are orthogonal to each other and fixed to the rotor centroid. The geometry of the rotor magnet is symmetric about  $Z_1$  axis.

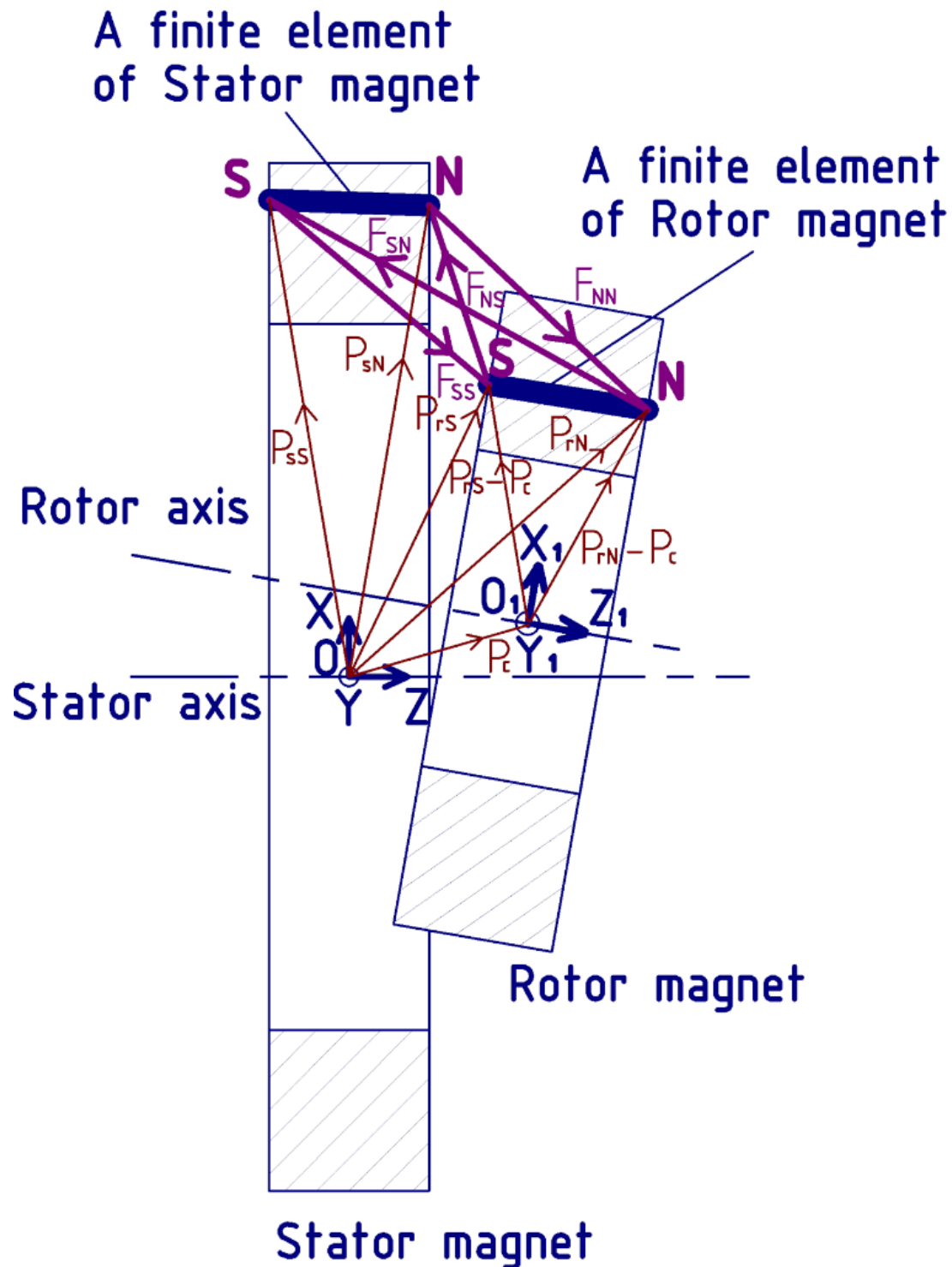


Fig. 32. Schematic of mathematical model of PMB load

$F_{NN}$  and  $F_{SN}$  are the magnetic force of a finite stator element applied on the north pole of the finite rotor element due to the magnetic field of the north and south poles of the finite stator element. The directions are shown in Fig.32. Similarly,  $F_{SN}$  and  $F_{SS}$  are defined and demonstrated in Fig.32. The value of the position vectors  $P_{SS}$  and  $P_{SN}$  in Fig. 32 indicates the south and north pole positions of the stator magnet element respectively. Similarly,  $P_{rS}$  and  $P_{rN}$  indicate the positional value of the poles of the rotor magnet element. The value of the center position of the rotor magnet is indicated by  $P_c$ , as shown in Fig.32. The directional arrow of the positional vectors is also demonstrated in Fig. 32.

Now magnetic force acted on a rotor magnetic element due to one stator magnetic element is expressed as follows.

$$\vec{F}_{NN} = F_{ref} A_r A_s \left\{ \frac{(\vec{p}_{rN} - \vec{p}_{sN})}{(|\vec{p}_{rN} - \vec{p}_{sN}|)^3} \right\} \quad (90a)$$

$$\vec{F}_{SN} = -F_{ref} A_r A_s \left\{ \frac{(\vec{p}_{rN} - \vec{p}_{sS})}{(|\vec{p}_{rN} - \vec{p}_{sS}|)^3} \right\} \quad (90b)$$

$$\vec{F}_{NS} = -F_{ref} A_r A_s \left\{ \frac{(\vec{p}_{rS} - \vec{p}_{sN})}{(|\vec{p}_{rS} - \vec{p}_{sN}|)^3} \right\} \quad (90c)$$

$$\vec{F}_{SS} = F_{ref} A_r A_s \left\{ \frac{(\vec{p}_{rS} - \vec{p}_{sS})}{(|\vec{p}_{rS} - \vec{p}_{sS}|)^3} \right\} \quad (90d)$$

And the resultant Force value by stator element on rotor element due to four poles combination between the rotor and stator element pair is defined as  $F_{ers}$ . The following vector expression represents the same.

$$\vec{F}_{ers} = \vec{F}_{NN} + \vec{F}_{SN} + \vec{F}_{NS} + \vec{F}_{SS} \quad (90e)$$

Where, reference force,  $F_{ref} = \frac{Br_1 Br_2 \delta^2}{4\pi\mu_0}$  [53]

$Br_1$ , and  $Br_2$  are the residual flux density of stator and rotor magnets accordingly. Maximum radial clearance between rotor and stator is indicated by  $\delta$ . Absolute magnetic permeability is indicated by  $\mu_0$ .

The total force is calculated by algebraic vector summation of all forces as shown below, where  $N_1$  and  $N_2$  are the number of mesh elements for rotor and stator, respectively.

$$\vec{F} = \sum_{s=1}^{N_1} \sum_{r=1}^{N_2} \vec{F}_{ers} \quad (91)$$

The other positional vectors have suffix r and s to indicate the index of the rotor mesh element and stator mesh element respectively. North and south polarity is indicated by N and S accordingly. Similarly, value of moment vector is indicated by  $M_{ers}$  and found as follows.

$$\vec{M}_{ers} = \delta \times [(\vec{p}_{rN} - \vec{p}_c) \times \{\vec{F}_{NN} + \vec{F}_{SN}\} + (\vec{p}_{rS} - \vec{p}_c) \times \{\vec{F}_{NS} + \vec{F}_{SS}\}] \quad (92)$$

$\delta$  will be in equation (92) while there is the consideration of non-dimensional parameter for  $\vec{p}_c$ ,  $r_{sr}$  or  $\vec{p}_{rN}$  and so on to maintain the same practice as equation (34c). Where, translation positional vector of rotor magnet centroid expressed as follows.

$$\vec{p}_c = \begin{bmatrix} x_{rc} \\ y_{rc} \\ z_{rc} \end{bmatrix} \quad (93)$$

The total moment is calculated by algebraic vector summation of all moments of all elements.

$$\vec{M} = \sum_{s=1}^{N_1} \sum_{r=1}^{N_2} \vec{M}_{ers} \quad (94)$$

Stiffness coefficient ( $K_{ab}$ ) is estimated using central finite difference method as follows.

$$K_{ab} = \frac{-V_{a(b+\Delta b)} - V_{a(b-\Delta b)}}{2\Delta b} \quad (95)$$

Where, V corresponds to F or M, a and b corresponds to x, y, z,  $\alpha$ ,  $\beta$  and  $\gamma$ . Hence stiffness matrix due to magnetism only is shown below expression (96).

$$K_m = \begin{bmatrix} K_{xx} & K_{xy} & K_{xz} & K_{x\alpha} & K_{x\beta} & K_{x\gamma} \\ K_{yx} & K_{yy} & K_{yz} & K_{y\alpha} & K_{y\beta} & K_{y\gamma} \\ K_{zx} & K_{zy} & K_{zz} & K_{z\alpha} & K_{z\beta} & K_{z\gamma} \\ K_{\alpha x} & K_{\alpha y} & K_{\alpha z} & K_{\alpha\alpha} & K_{\alpha\beta} & K_{\alpha\gamma} \\ K_{\beta x} & K_{\beta y} & K_{\beta z} & K_{\beta\alpha} & K_{\beta\beta} & K_{\beta\gamma} \\ K_{\gamma x} & K_{\gamma y} & K_{\gamma z} & K_{\gamma\alpha} & K_{\gamma\beta} & K_{\gamma\gamma} \end{bmatrix} \quad (96)$$

### 6.2.3 Computation strategy of the model

The computation strategy is found by compromising between results error and allowable time resources for computation. The increment of mesh density reduces the error and increases computation time. The computation step includes a while loop that checks the allowable error and computation total time resource limit. If the limit permits, it increases mesh density by reducing the maximum element size for each loop iteration. The initial maximum size (indicated by  $e_{\max}$ ) of triangular mesh elements as shown in Fig. 30, is considered as per the following expression (97).

$$e_{\max} = \sqrt{R_{so}^2 + R_{ro}^2 - R_{si}^2 - R_{ri}^2} \quad (97)$$

### 6.2.4 Algorithm of the model

The computation of the proposed model is done with an algorithm that follows the flow chart is shown in Fig. 33.

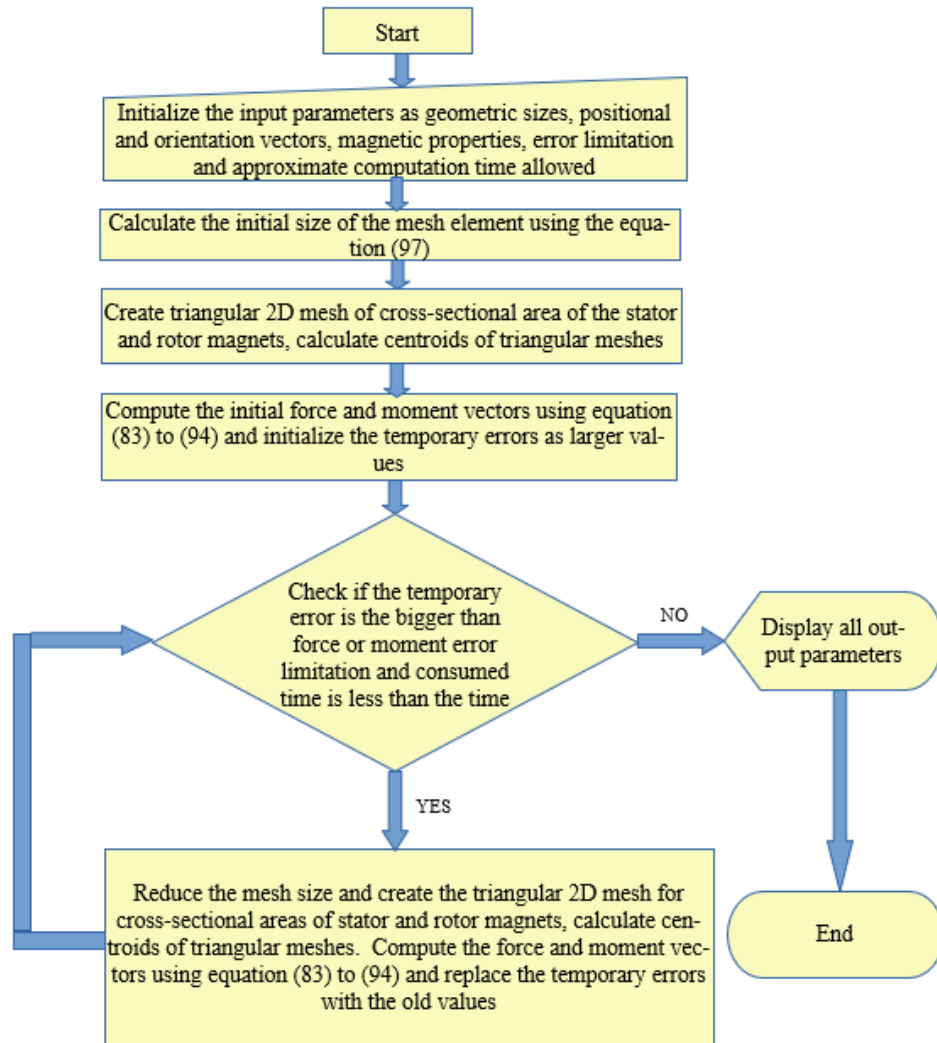


Fig. 33. Flowchart of the program of the proposed model

### 6.3 Sensitivity analysis of error and computational time on mesh density

The sensitivity study of absolute error and computation time are conducted together. The maximum size of the element reduces while multiplying a suitable fractional number of 0.75 for each step. The relevant number of elements also increased on mesh generation for each iteration. Hence, Mesh density.

(i.e., number of elements per unit area) also increases. The error and computation time is calculated for each mesh density and plotted in Fig. 34. Geometric and magnetic properties of PMB are taken from Table 17. Rotor magnet position is considered radially 1 mm shift and axially 5 mm shift from the stator magnet. Axes of the rotor magnet and stator magnet are considered parallel here. The slope of Relative errors, as per Fig. 34, becomes almost flat and reaches below 0.63% for mesh density approximately above 48 elements/ cm<sup>2</sup>. The optimum computation time is approximately below 4 seconds for this mesh density. Computation time increases with

the increment of mesh density, as shown in Fig. 34. The convergence error mentioned as an error bar in Fig. 36, Fig. 37, Fig. 38, Fig. 39 and Fig. 41 is demonstrated to get the confidence of the computation.

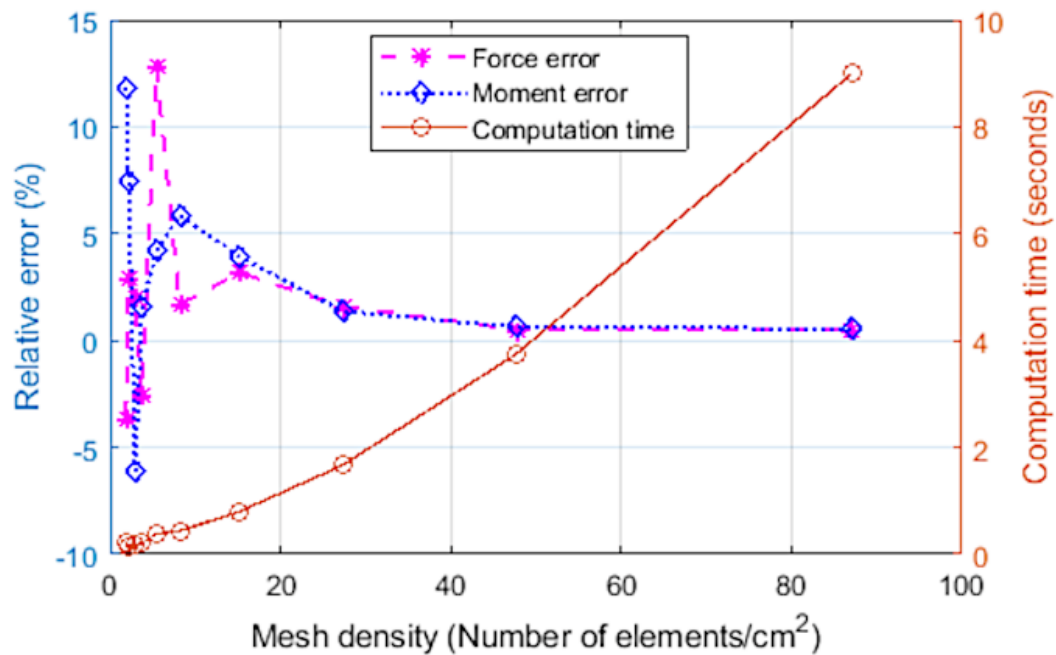


Fig. 34. Relative errors and computation time variation with mesh density

## 6.4 Validation of the proposed model

The basic estimated parameters, such as force and moment, are validated with the relevant previous research data [38] and compared with the FEM analysis tool (A commercial software). A similar method was adopted to [53] extract data in a quantified

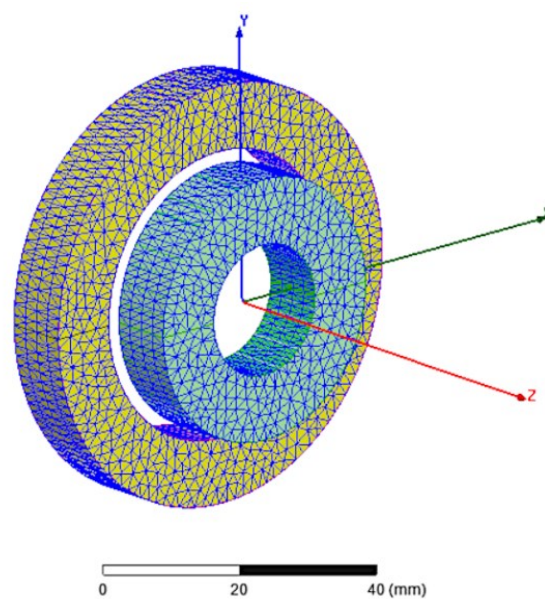


Fig.35. 3D Mesh plot of magnets in A commercial software



format for comparison. We found present model holds good validation with the existing model in the force parameter comparisons plot. Further, parameters estimated using other FEM analysis tools (A commercial software) also confirm a close comparison plot of results.

The typical input data of Table 17 and Table 18 are used for validation and comparison purposes. Here, the rotor translation movement is considered on the XZ plane only with zero tilt for validation. In commercial software, default tetrahedron elements are created during meshing, as shown in Fig. 35. We used a parametric option in Magnetostatics Solver of a commercial software for setting different rotor magnet positions to compute relevant forces and moments in row vectors. This tool solves the Maxwell magnetostatics equation using the integral of the surface current source method followed by generalized potential formulation [56]. Fig. 35 shows all three axes of the rotor magnet and 3D meshing axes.

Table 17 Physical parameters for validation

Input parameters	Values with units
Inner radius of the rotor ring magnet	0.010 m
Outer radius of the rotor ring magnet	0.020 m
Inner radius of the stator ring magnet	0.022 m
Outer radius of the stator ring magnet	0.032 m
Length of the rotor magnet/ stator magnet	0.010 m
Residual flux density of magnets	1.0 T (kg. s <sup>-2</sup> . A <sup>-1</sup> )
Absolute magnetic permeability	$4\pi \times 10^{-7}$ N/ A <sup>2</sup>
Relative magnetic permeability	1.0

Table 18 Mesh and other Parameters for Validation

Input parameters	Values with units
Initial absolute error of forces used in proposed model	4 N
Initial absolute error of moments used in proposed model	0.01 Nm
Initial relative error of both force and moment used in proposed model	0.1%
Cumulative computation time resource per estimation of force and moment together used in proposed model	3 seconds
Variable density of triangular mesh used in proposed model for rotor and stator magnet	25-90 number of elements/ cm <sup>2</sup>
Number of elements used in software for rotor magnet	11649
Number of elements used in software for stator magnet	19410

### 6.4.1 Proposed model validation using axial force data

The axial force is calculated at the different axial shifts of the rotor magnet as Fig. 36. The radial shift of the rotor magnet for this calculation is kept constant at 1 mm. The absolute maximum and minimum errors of the predicted axial force found in the proposed model are 2.346 N and 0 N. Here, the prediction error is the difference between the results on the last two successive iterations of the conditional loop of the algorithm shown in Fig. 33. The estimation of axial force using the proposed model almost matches the previous research by Bekinal et al. [38] shown in Fig. 36. However, it shows approximately different error values at all positions compared with a commercial software result. The main two probable reasons for this error compared with commercial software results are the demagnetization effect and non-optimum or coarse element size. The average density of tetrahedral mesh calculated here is 1177 elements/ cm<sup>3</sup> for estimation using a commercial software to limit the computation cost. Also, demagnetization effects due to the proximity of the rotor and stator magnet are not considered in the proposed model. Error bars represent the range of model residual errors in predicted values, varying for different dependent variable values. These residual errors are derived from the output metrics at the final iteration step and can be positive or negative.

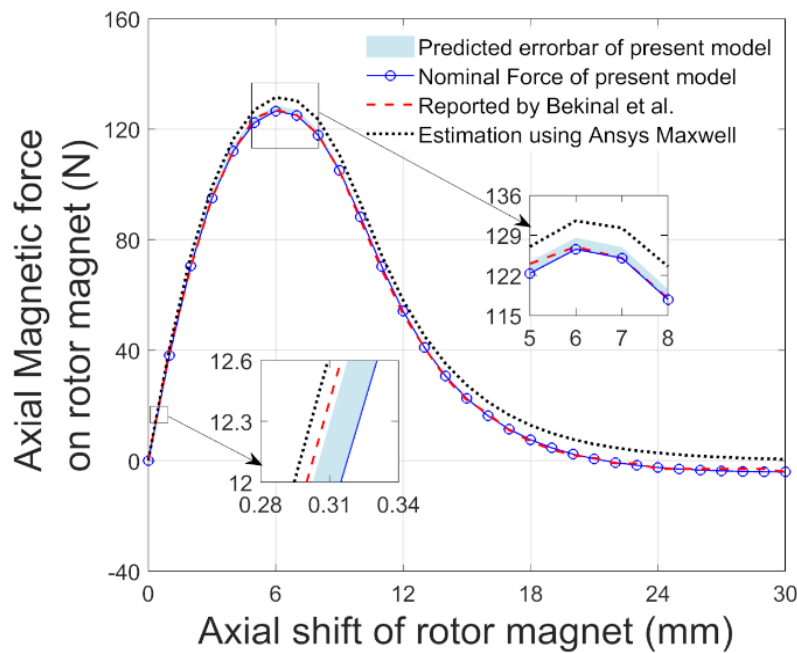


Fig. 36. Variation of magnetic axial force on rotor magnet with the variation of axial shift of rotor magnet from stator magnet for validation of present model with the existing model

### 6.4.2 Proposed model validation using radial force data

The radial force is calculated at the different radial shifts of the rotor magnet as Fig. 37. The axial position of the rotor magnet for this calculation is kept constant at zero. The maximum and minimum absolute prediction radial force errors found on the proposed

model are 1.772 N and 0.008 N. The estimation of radial force using the proposed model with the algebraic sum of the prediction error almost matches previous research [38], as shown in Fig. 37. Hence, the estimation of radial force using the proposed method is closer to the previous research by Bekinal et al. [38] than the computation value in software. The probable reasons are as same as mentioned earlier for axial force validation. The nature of errors while comparing with computation in a commercial software grows with the increment of radial force value.

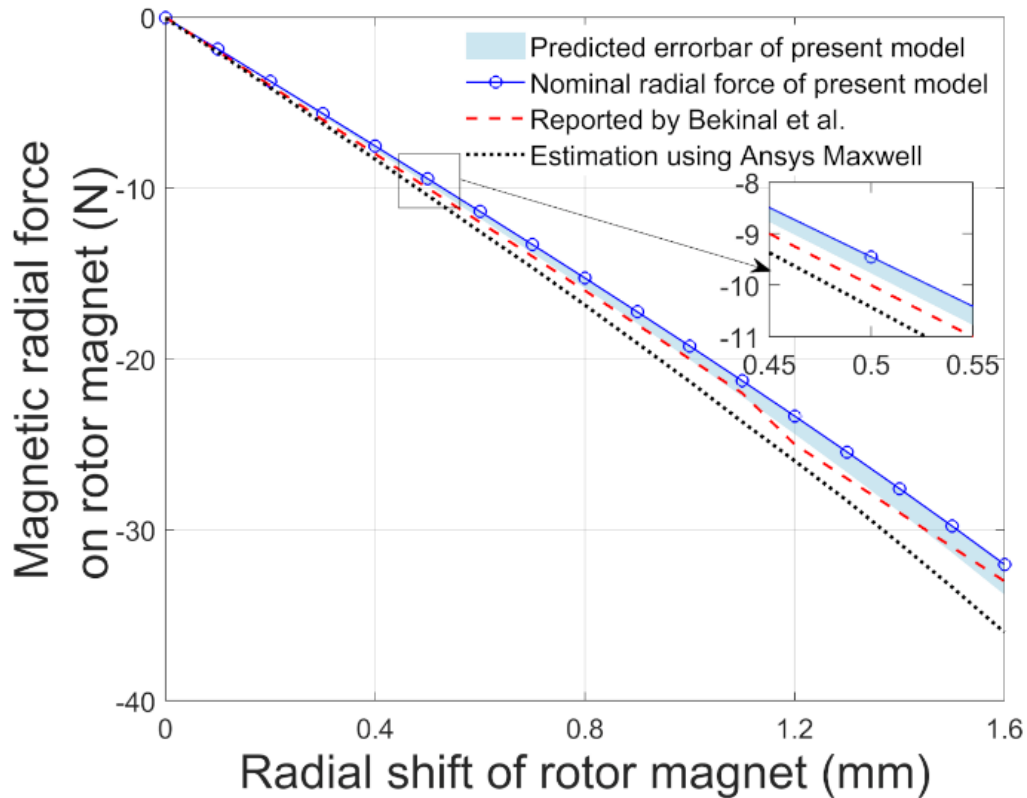


Fig. 37. Variation of magnetic radial force on rotor magnet with the variation of radial shift of rotor magnet from stator magnet for validation of present model with the existing model

### 6.4.3 The moment comparison

In the XZ plane, the moment is considered about an axis parallel to the Y-axis, passing through the geometric centre of the rotor magnet. The moment estimated from the proposed method is compared with the moment result of a commercial software only. We have yet to find any validated moment data from previous research with this type of PMB configuration. The moment of the rotor magnet is calculated at the different axial shifts of the rotor magnet as Fig. 38. The radial shift of the rotor magnet for this moment calculation is kept constant at 1 mm. The absolute value of the maximum and minimum prediction of moment errors found in the proposed model is 0.0088 Nm and 0 Nm, accordingly. Thus, the variation of the moment using the present model is also compared and validated with the results using a commercial software are shown in Fig. 38. Here, the magnetic moment results about the centroidal Y-axis of the rotor magnet

using the recommended method are close to the computation results estimated by software. Here, the maximum difference in results between the recommended method and the software tool is 0.017 Nm. This maximum difference result is found while calculating the moment at the rotor magnet's 1 mm axial shift and 1 mm radial shift. As a result, the moment value using the proposed method at this position is -0.0966 Nm, and the same using software is -0.1136 Nm. The reasons for this minor variation of results should be the same as discussed in the proposed model validation with axial force data.

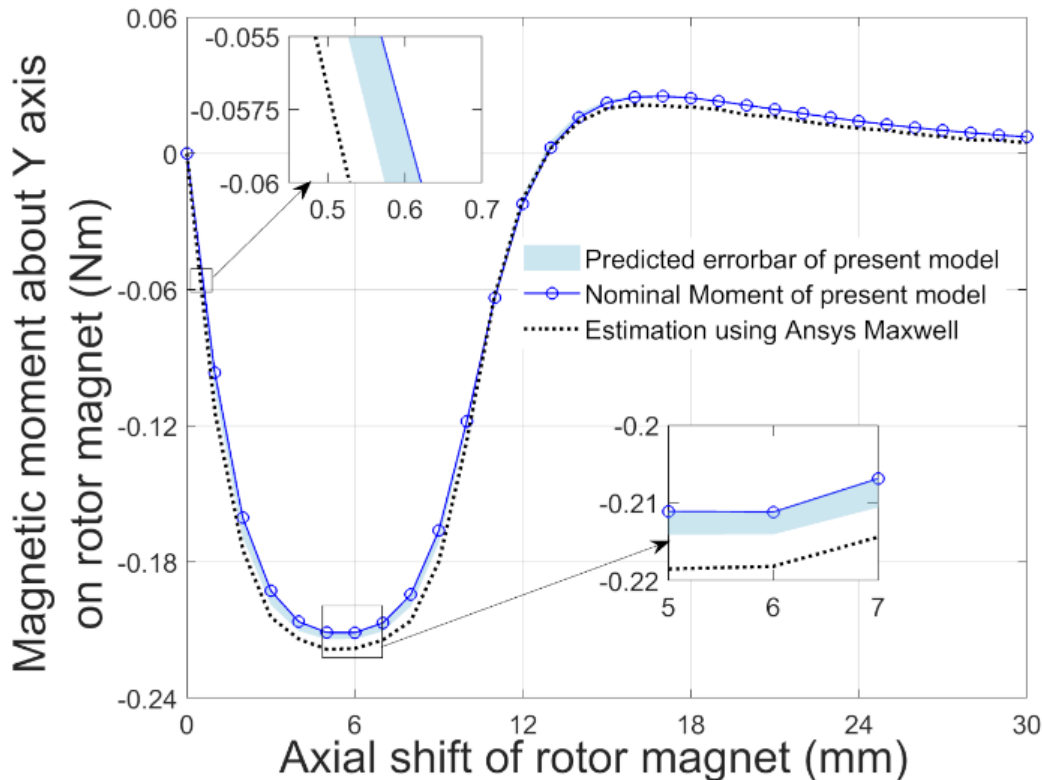


Fig. 38. Variation of magnetic moment about centroidal Y axis of rotor magnet for validation of present model with a commercial software

## 6.5 Simulation results for magnetic moment and stiffness characteristics using proposed method

The proposed method with an applied example is simulated here using the same input of Table 17 and Table 18. The magnetic moment for the various shift positions and tilt as angular orientations is simulated.

The magnetic moment of the rotor magnet about the centroidal Y-axis for various axial shift positions is simulated in Fig. 39. The plots in Fig. 39 also compare moments for the different radial shifts. The orientation considered here is constant and maintains concentric axial alignment between magnets. The plots in Fig. 39 also consist of prediction errors tendency as shades for each calculation. A separate contour plot of the magnetic moment about the centroidal Y-axis is shown in Fig. 40 with color scale and

lines to understand the constant magnetic moment line characteristics on the XZ plane.

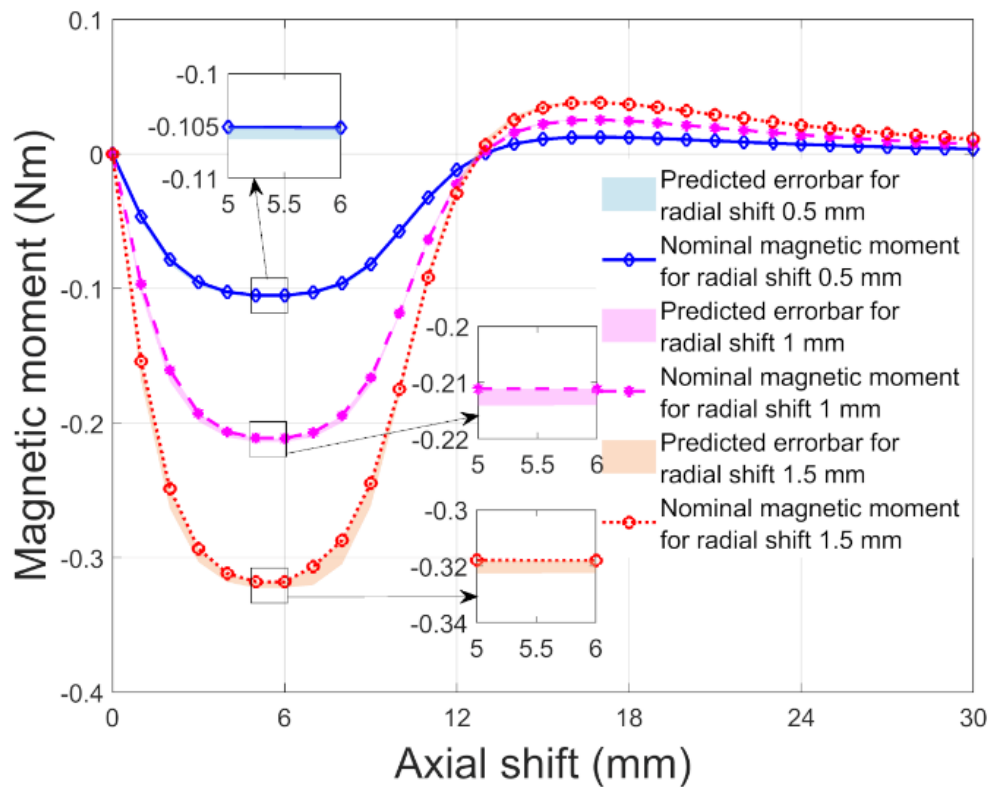


Fig. 39. Magnetic moment with subsequent prediction error bar distribution along axial shift for three different radial shifts differentiating by three colors of blue, magenta and red accordingly

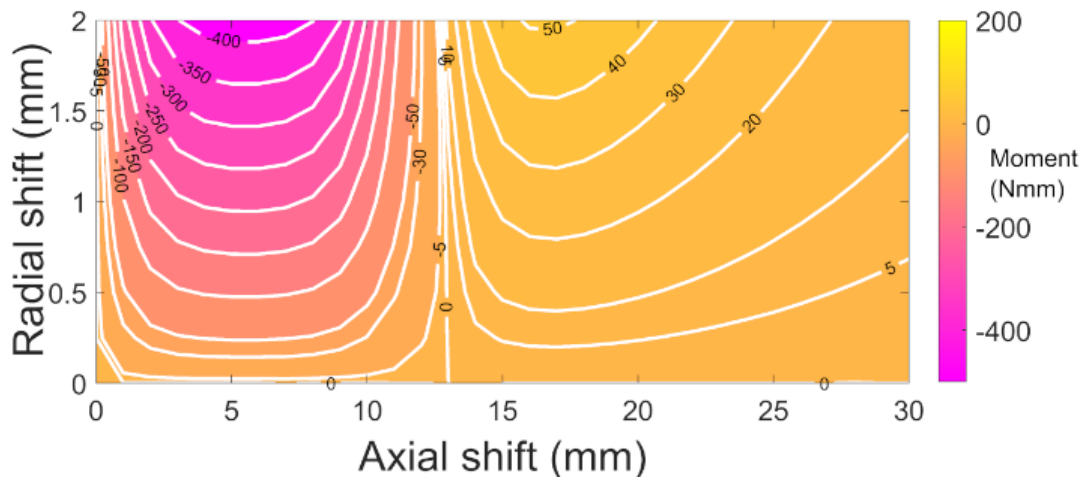


Fig. 40. 2D contour plot of magnetic moment about centroidal Y axis distributed over XZ plane

Only the relative radial position in the X direction and the relative axial position in the Z direction are considered for the 2D contour plot for the magnetic moment in the XZ plane, keeping all other degrees of freedom as zero. The equal magnitude moments (in Nm) are joined with the white line mentioning the value. The colour map with a scale

presents an additional presentation of moment estimation. The magnetic moment in Fig.40 is negative (clockwise) for axial shifts up to approximately 13 mm and positive (counterclockwise) for axial shifts above 13mm. The radial shift of the rotor magnet centre is positive (away from the radial X direction and perpendicular to the stator axis).

Another similar magnetic moment distribution over tilt about the centroidal Y-axis is shown in Fig. 41. Here, the centroid of the rotor magnet is kept radially zero position such that the centroid of the rotor always lies on the stator magnet axis for all tilts and axial shifts. It also compares the moment and its error bar for the different axial shifts of the rotor magnet. The moment for a particular tilt angle is reducing with the increase of axial shifts from zero to 5 mm axial shift. Finally, it becomes negative at a 10 mm axial shift in the same direction as observed in Fig. 41. This characterization is simulated for the variation of tilts from 0 degrees to 10 degrees in Fig. 41. This phenomenon is also observed in Fig. 42 along the Y axis. The absolute value of the magnetic moment about the centroidal Y-axis of the rotor magnet increases with the increase of tilt angle about the same centroidal Y-axis.

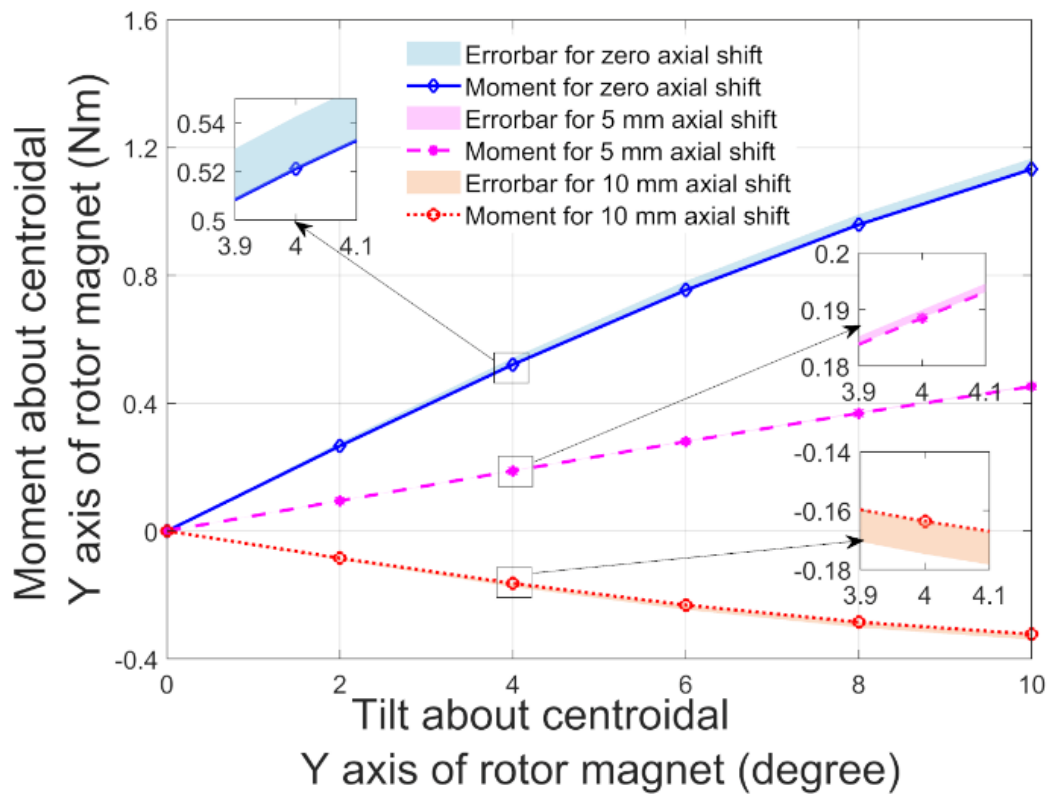


Fig. 41. Magnetic moment with subsequent prediction error bar distribution over tilts about centroidal Y axis of the rotor magnet for three different axial shifts differentiating by three colors of blue, magenta and red accordingly

A similar characterization simulation can also be observed if we change the rotor magnet axial length without changing the stator parameters; even the rotor magnet centroid is radially and axially at zero position. A 2D contour plot in Fig. 42 shows a color scale and constant magnetic moment line to describe the observation. The contour plot presents the magnetic moment variation where tilt about the centroidal Y axis varies in the vertical axis, and rotor magnet axial length varies in the horizontal axis.

Fig. 42 shows that moment becomes positive up to approximately 20 mm axial rotor length. The moment becomes negative (changed moment direction) for the axial length above 20 mm. The moment in Fig. 42 becomes maximum at 10 mm axial length of the rotor (equal length of stator magnet) and 10 degrees tilt of the rotor. Similar behaviour is also understood from Fig. 14 that resisting moment (negative moment) with the increase of tilt can be achieved once the rotor magnet axial length is more than 20 mm approximately while the stator magnet axial length remains the same at 10 mm. Thus, a designer can choose the appropriate rotor length to achieve the required angular stiffness and stability when there is a demand for angular stiffness. The same demand of angular stiffness can be fulfilled with the proper axial shift, as shown in Fig. 41, with the same length of rotor and stator.

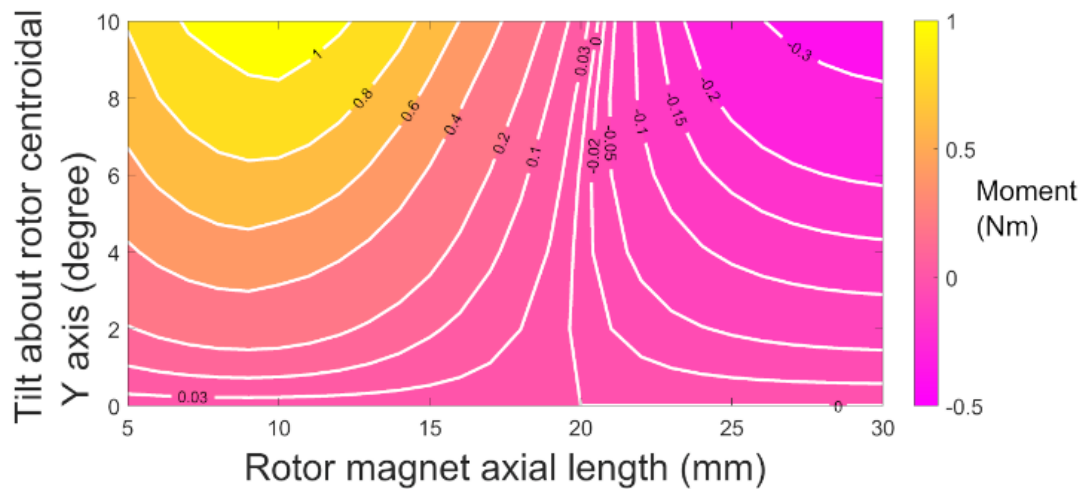


Fig. 42. 2D Contour plot of magnetic moment about centroidal Y axis of rotor magnet distributed over variation of tilt and rotor magnet length

This characteristic can also be understood from the 6-DOF stiffness matrix, as shown in Tables 19 and 20. The stiffness matrix in Table 19 and Table 20 is calculated when the rotor has zero shift and tilt orientation in all degrees of freedom. The other input parameters are also the same as Table 17 and Table 18 except for the rotor magnet axial length for calculating the stiffness matrix of Table 20. The rotor magnet axial length is chosen as 30 mm to get the diagonal positive angular stiffness matrix, as shown in Table 20. The value is 1.98 Nm/ rad. Table 19 shows negative angular direct stiffness as -7.96 Nm/ rad as the same length (10 mm) of stator and rotor magnet is chosen for calculation. The first row and column of Table 19 and Table 20 indicate the degrees of freedom and relevant load type. Direct and cross stiffness for the spin angular degree of freedom is found zero in Table 19 and Table 20. This zero is found as the stator magnet is symmetric about its cylindrical axis. If the stator is an intermittent or arc type of segmented magnet, the direct stiffness coefficient of the rotational axis about the Z-axis can be non-zero.

Table 19 magnetic stiffness coefficients for equal length of rotor and stator magnet

	X	Y	Z	$\alpha$	$\beta$	$\gamma$
Fx	19440 N/m	-4.179 N/m	0	0	0	0.0011 N/rad
Fy	-4.179 N/m	19449 N/m	0	0	0	0.0077 N/rad
Fz	0	0	-38889 N/m	-0.0774 N/rad	0.0188 N/rad	0
Mx	0	0	-0.0774 N	-7.96 Nm/rad	-0.0014 Nm/rad	0
My	0	0	0.0188 N	-0.0014 Nm/rad	-7.96 Nm/rad	0
Mz	0.0011 N	0.0077 N	0	0	0	0

Table 20 magnetic stiffness coefficients for increased length of rotor magnet from stator

	X	Y	Z	$\alpha$	$\beta$	$\gamma$
Fx	1623 N/m	0.0187 N/m	0	0	0	-0.0005 N/rad
Fy	0.0187 N/m	1623 N/m	0	0	0	-0.0002 N/rad
Fz	0	0	-3245 N/m	0.0003 N	0.001 N/rad	0
Mx	0	0	0.0003 N	1.98 Nm/ rad	0	0
My	0	0	0.001 N	0	1.98 Nm/ rad	0
Mz	-0.0005 N	-0.0002 N	0	0	0	0

A permanent magnet must be integrated with proper stiffed and damped interfaces to stabilize. Table 19 and 20 stiffness matrices here require additional positive stiffness (mainly axial stiffness). A positive value of the axial stiffness may be obtained using a pin joint support with a flexible structure to one end of the rotor magnet. The other end of the same structure has a fixed joint. The stiffness matrix can be converted to a modal stiffness matrix, assuming mass as the identity matrix. The eigenfrequency can be analyzed for its static stability. Static stability demands the diagonal element of the normalized modal stiffness matrix to be positive. Direct angular stiffnesses, as per the fourth and fifth diagonal elements in Table 19, become positive, as shown in the same component in table 20, by changing the geometric property as the length of the rotor magnet.

Similarly, The Moment component of the rotor centroid along the global Z-axis may be assumed as a relatively high stiffness value equal to the shaft's twisting stiffness, considering the angle between the Z and Z1 axis as significantly less. Hence, various random positive assumed stiffness values are added in Tables 19 and 20 separately to the coefficient  $K_{zz}$  and  $K_{\gamma\gamma}$  to assess the eigenfrequency. In all the cases, the table 20 stiffness matrix has positive eigenvalues after the above addition, whereas table 19 does not. Thus, rotor magnet axial length also significantly contributes to stiffness and stability.



## 6.6 Summary

This chapter presents a typically semi-analytic and finite element approach that differs from past available methods. The magnetic moment characterization of permanent ring-type axially magnetized magnetic bearing is explained in Fig 39, Fig. 40, Fig. 41, and Fig. 42. Particularly the plot of magnetic moment, proper validation of this kind of permanent magnetic bearing is not found in previous pieces of literature. A complete 6-DOF stiffness matrix is also studied. A characterization also shows how angular stiffness or resisting moment varies with the tilt angle. Furthermore, A designer can wisely choose the rotor magnet length or axial shift position while demanding positive angular direct stiffness, as shown in table 20. An algorithm is also presented here with this suggested model that handles the improvisation between numerical error and computation time. The algorithm of this proposed method is simplified for scripting. The simplicity of matrix operation in the proposed model will allow them to couple with another physical interface around the spatial boundary of the bearing. Hence, it has the future scope for studying dynamic stability considering the presence of any fluid in the clearance of the rotor and stator. Viscous damping due to the other fluid's passive or active interaction can be studied for stability and disturbance rejection. This overall finding will help the designer to optimize for a specific goal related to the magnetic moment and direct angular stiffness with the constraint of PMB parameters, such as the length of the rotor magnet over a stator magnet shift position of the rotor magnet. Thus, this chapter has addressed the second and third objectives. The knowledge from Chapter 6 can add value to the next chapter to address the last objective of the research.

## **7. Numerical study of hybrid-system of bearings**

In persuasion of the fourth objective of the research and the gap realized from the literature review done in Chapter 2.3, as also expressed in Chapter 2.4, The following works have correlations with earlier works. The fundamental characteristics of a hybrid system of different types of bearings are shown in this chapter with the non-dimensional analytical model. The fundamental characteristics of the hybrid system of multiple types of bearings are shown in this present work with a non-dimensional analytical model. The hybrid bearings system is a simple arrangement of permanent magnet bearings and fluid film plain cylindrical short bearings with a standard journal. It can also be valid for certain types of compact hybrid bearings instead of the system of bearings. The characteristic analysis covers the non-dimensional trajectory of the journal position, natural frequency, stability analysis, and the journal's response to harmonic load. The analysis results of the hybrid bearings system are compared with the results of fluid film plain cylindrical similar bearing pairs. This study is to understand the conditions of improved behaviours of the hybrid system of different bearings over fluid film bearings.

### **7.1 Introduction**

There is the requirement of such an analytical study like fluid film plain journal bearing so that designer can easily choose the design parameters to use such a hybrid system of bearings and also check if it is feasible with the desired application. From this motivation, analytical non-dimensional characteristics of the hybrid system of bearings are derived. So, there will be some fundamental clarity of the feasibility zone of such a hybrid system. A combination of passive magnetic bearing and fluid film plain cylindrical short bearing is considered in the present scope of work. However, it will still be valid for other magnetic bearings systems where the radial stiffness of magnetic bearing will not vary directly on all angular positions of the rotor magnet. Hence, the hybrid bearings with the angle of the arc of the stator magnet [26, 102-105] cannot be theoretically characterized with this present scope of the study. The findings are also shown in comparison figures with plain cylindrical short-bearing pairs of fluid film.

### **7.2 Details of the proposed model**

The detail analytical model is presented with derivation and schematic of the set up.

#### **7.2.1 Hybrid bearing setup**

A fluid film plain cylindrical short bearing, a stator ring magnet, a rotor magnet and a

standard journal are the key elements of a hybrid system of bearings setup, as shown in schematic views in Fig.43 and Fig. 44.

The journal of radius  $R_1$  is considered to be rotating with a constant anti-clockwise rotational speed. Journal centre  $C_j$  is located at a point of eccentricity  $\epsilon$  to the geometric centre  $C_b$  of the fluid film plain cylindrical short bearing of radius  $R_b$  and length  $L$ . The rotor magnet is concentric with a journal and attached to the journal with a fixed joint. The stator magnet is concentric with fluid film plain cylindrical short bearing and fixed with a common grounded base of both bearings. The rotor and stator magnet length is commonly considered  $L$  as the same length of short bearing. Hence both bearings are considered very close axially to each other and act as a parallel combination. Both the magnets of the rotor and stator have an axial magnetization. Rotor magnets have an inner and outer radius of  $R_1$  and  $R_2$  respectively. The same for stators have  $R_3$  and  $R_4$ , respectively. In this proposed model setup, the journal and other assumed rotary elements, excluding mass due to magnetic rotor arrangements, are considered rigid. It is also considered that these have lumped mass of  $m_0$ . However, A lumped mass, including the mass of rotor magnetic arrangements, is considered  $m$ . The reason for considering different masses is to compare both bearings systems with the applicable mass. Mass can also be considered as same when no comparison will be studied. The same maximum radial clearance or gap is also considered for all bearings for easy analytical purposes.

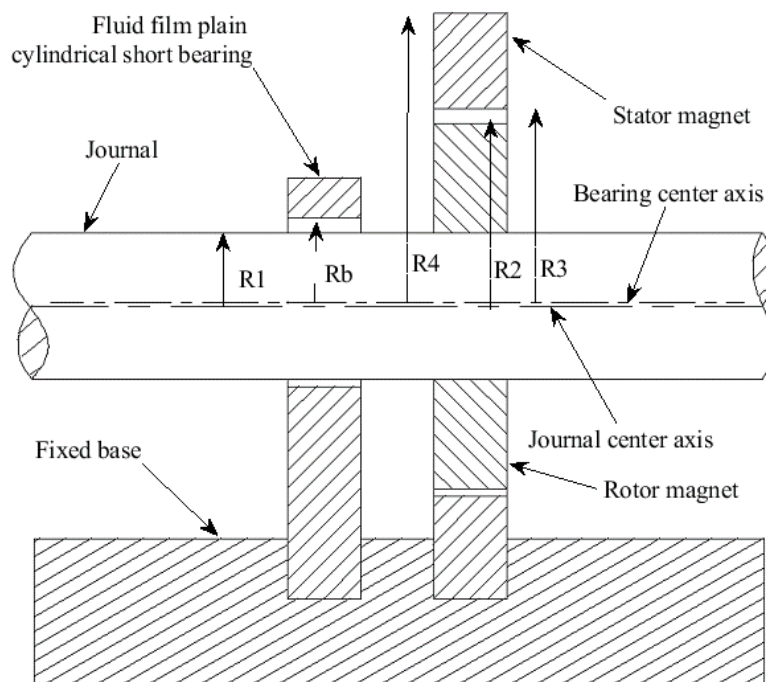


Fig. 43: Schematic front view of hybrid system of bearings



model of fluid film plain cylindrical short bearing [76] and model of ring type permanent magnet bearing [28, 31-35, 37-42, 47-49, 53, 65, 73, 117]. The Reynolds force of short bearing along X' and Y' are as follows [76].

$$F'_x = -F_{cb} \left\{ \epsilon \left( 1 - 2 \frac{\dot{\phi}}{\Omega} \right) \frac{2\epsilon^2}{(1-\epsilon^2)^2} + \pi \frac{\dot{\epsilon}}{\Omega} \frac{(1+2\epsilon^2)^{\frac{5}{2}}}{(1-\epsilon^2)^{\frac{5}{2}}} \right\} \quad (98)$$

$$F'_y = -F_{cb} \left\{ \frac{-\pi}{2} \left( 1 - 2 \frac{\dot{\phi}}{\Omega} \right) \frac{\epsilon}{(1-\epsilon^2)^{\frac{3}{2}}} - \frac{\dot{\epsilon}}{\Omega} \frac{4\epsilon}{(1-\epsilon^2)^2} \right\} \quad (99)$$

Where  $F_{cb}$  is Reynold's force coefficient,  $\mu$  is the absolute viscous coefficient of the fluid.  $\delta$  is the common radial clearance of fluid film plain cylindrical short bearing.

$$F_{cb} = \frac{\mu \Omega R_b L^3}{2\delta^2} \quad (100)$$

For static equilibrium the following relation holds.

$$\frac{\dot{\phi}}{\Omega} = 0, \frac{\dot{\epsilon}}{\Omega} = 0 \quad (101)$$

Reynolds dynamic force components along X and Y coordinates are as follows [76].

$$F_x = F'_x \cos \phi - F'_y \sin \phi \quad (102)$$

$$F_y = F'_x \sin \phi + F'_y \cos \phi \quad (103)$$

Magnitude of this force is,

$$F_b = \sqrt{(F_x^2 + F_y^2)} \quad (104)$$

Or,

$$F_b = \sqrt{(F'_x^2 + F'_y^2)} \quad (105)$$

And attitude angle only due to fluid film plain cylindrical short bearing is,

$$\eta = \tan^{-1} \frac{-F'_y}{F'_x} \quad (106)$$

Hence, following relation can be concluded where  $f_b$  is function of dynamic force without coefficients.

$$|F_b| = f_{cb} \Omega f_b \left( \epsilon, \frac{\dot{\epsilon}}{\Omega}, \frac{\dot{\phi}}{\Omega} \right) \quad (107)$$

$$f_{cb} = \frac{\mu R_b L^3}{2\delta^2} \quad (108)$$

The coefficient  $f_{cb}$  is always constant for a particular system of fluid film plain cylindrical short bearing.

The following expression is also true at static position of journal where  $f_{bs}$  is function of static force without coefficients.

$$\dot{\epsilon} = 0, \dot{\phi} = 0 \quad (109)$$

$$F_{bs} = f_{cb}\Omega f_{bs}(\epsilon) \quad (110)$$

Where,  $F_{bs}$  is the magnitude of static force.  $f_{bs}(\epsilon)$  is modified Summerfield number of fluid film short cylindrical bearing [76].

From the above following dynamic stiffness  $K_b$  and damping coefficient  $C_b$  of fluid film plain cylindrical short bearing can be arrived [76].

$$[K_b] = \left[ \left( \frac{F_{cb}}{\delta} \right) \begin{bmatrix} \cos\phi & \frac{-\sin\phi}{\epsilon} \\ \sin\phi & \frac{\cos\phi}{\epsilon} \end{bmatrix} \begin{bmatrix} \frac{\partial F_x}{\partial \epsilon} & \frac{\partial F_y}{\partial \epsilon} \\ \frac{\partial F_x}{\partial \phi} & \frac{\partial F_y}{\partial \phi} \end{bmatrix} \right]^T \quad (111)$$

$$[C_b] = \left[ \left( \frac{F_{cb}}{\Omega\delta} \right) \begin{bmatrix} \cos\phi & \frac{-\sin\phi}{\epsilon} \\ \sin\phi & \frac{\cos\phi}{\epsilon} \end{bmatrix} \begin{bmatrix} \frac{\partial F_x}{\partial \dot{\epsilon}} & \frac{\partial F_y}{\partial \dot{\epsilon}} \\ \frac{\partial F_x}{\partial \dot{\phi}} & \frac{\partial F_y}{\partial \dot{\phi}} \end{bmatrix} \right]^T \quad (112)$$

Non dimensional stiffness  $\bar{K}_b$  and damping coefficient  $\bar{C}_b$  are as expressed below.

$$[\bar{K}_b] = \frac{\delta}{F_b} [K_b] \quad (113)$$

$$[\bar{C}_b] = \frac{\Omega\delta}{F_b} [C_b] \quad (114)$$

Permanent magnetic radial force is almost directly proportional to the radial eccentricity of the journal or rotor magnet at zero axial shift of magnets [28, 31-35, 37-42, 47-49, 53, 65, 73, 117]. the radial stiffness is almost constant at zero axial shift between magnets as found on various literatures [28, 31-35, 37-42, 47-49, 53, 65, 73, 117]. The magnetic radial cross stiffnesses are zero and direct stiffnesses are equal at same condition [53]. Hence, following relations for magnetic force ( $F_m$ ) with stiffness ( $K_m$ ) can be adopted for easy analytical purposes.

$$[F_m] = -K_m \begin{bmatrix} 1 & 0 \\ 0 & 1 \end{bmatrix} \delta\epsilon \begin{bmatrix} \cos\phi \\ \sin\phi \end{bmatrix} \quad (115)$$

Non dimensional magnetic stiffness expression will be as follows.

$$[\bar{K}_m] = \begin{bmatrix} 1 & 0 \\ 0 & 1 \end{bmatrix} \quad (116)$$

The radial magnetic reaction force on the journal is along the eccentricity displacement of the journal centre. Reynold's reaction force is acting same location on the journal approximately as a concurrent force system, as shown in Fig. 44. The angle among them is equal to the attitude angle of a fluid film plain cylindrical short bearing. The angle of action of applied force on the journal acts  $\beta$  angle from the eccentricity displacement or magnetic force. The angle  $\beta$  is the modified attitude angle of the hybrid

bearings setup system. Under equilibrium conditions, the following expressions hold.

$$F_a^2 = F_b^2 + F_m^2 + 2F_b F_m \cos \eta \quad (117)$$

$$\beta = \tan^{-1} \frac{\sin \eta}{\frac{F_m}{F_b} + \cos \eta} \quad (118)$$

If external load on journal is acting at an angle  $\alpha$  with X axis then following relation holds.

$$\phi = \alpha + \beta \quad (119)$$

Angle  $\alpha$  is  $-90^\circ$  for downwards vertical applied load on journal.

The following state-space representation may be considered to find the trajectory of journal position or the final static position of the journal in case of vertical load.

$$\frac{d}{dt} \begin{bmatrix} x \\ y \\ \dot{x} \\ \dot{y} \end{bmatrix} = \begin{bmatrix} \dot{x} \\ \dot{y} \\ \frac{1}{m} F_{Tx}(t, x, y, \dot{x}, \dot{y}) \\ \frac{1}{m} F_{Ty}(t, x, y, \dot{x}, \dot{y}) \end{bmatrix} \quad (120)$$

Where,

Total horizontal force component as below,

$$F_{Tx}(t, x, y, \dot{x}, \dot{y}) = F_H - F_x - K_m x \quad (121)$$

And total vertical force component as below,

$$F_{Ty}(t, x, y, \dot{x}, \dot{y}) = F_V - F_y - K_m y \quad (122)$$

Here,  $F_H$  and  $F_V$  are the magnitude of horizontal and vertical force. In case of downward the sign of  $F_V$  may be considered as negative.

Orthogonal coordinates of the journal position and velocity of the above expressions can be converted to polar coordinates as follows.

$$\epsilon = \frac{\sqrt{x^2 + y^2}}{\delta} \quad (123)$$

$$\varphi = \tan^{-1} \frac{y}{x} \quad (124)$$

$$\dot{\epsilon} = \frac{(x+y)(\dot{x}+\dot{y})}{\delta \sqrt{x^2 + y^2}} \quad (125)$$

$$\dot{\varphi} = \frac{x\dot{y} - \dot{x}y}{x^2 + y^2} \quad (126)$$

Now, the expression (120) can be solved any two-state ordinary differential equation solver programs with initial condition.

For example, the initial velocity components may be considered zero at the initial condition if it allows moving from rest. The initial position may be considered near the bearing centre where eccentricity is close to zero.

To find the damped natural frequency general vibration equation will be,

$$\begin{bmatrix} m & 0 \\ 0 & m \end{bmatrix} \ddot{X} + \begin{bmatrix} c_{xx} & c_{xy} \\ c_{yx} & c_{yy} \end{bmatrix} \dot{X} + \left( \begin{bmatrix} k_{bxx} & k_{bxy} \\ k_{byx} & k_{byy} \end{bmatrix} + \begin{bmatrix} k_{mxx} & k_{mxy} \\ k_{myx} & k_{myy} \end{bmatrix} \right) X = 0 \quad (127)$$

Here, the rotating total mass is considered as m and stiffness and damping coefficient matrix details are considered from the following

$$\begin{bmatrix} c_{xx} & c_{xy} \\ c_{yx} & c_{yy} \end{bmatrix} = [C_b] \quad (128)$$

$$\begin{bmatrix} k_{bxx} & k_{bxy} \\ k_{byx} & k_{byy} \end{bmatrix} = [K_b] \quad (129)$$

$$\begin{bmatrix} k_{mxx} & k_{mxy} \\ k_{myx} & k_{myy} \end{bmatrix} = \begin{bmatrix} K_m & 0 \\ 0 & K_m \end{bmatrix} \quad (130)$$

The solution is considered as

$$X = X_0 e^{\omega t} \quad (131)$$

Where t is time and  $\omega$  is oscillating frequency.

From equation (30) the following derivation can be found.

$$\omega^2 \begin{bmatrix} m & 0 \\ 0 & m \end{bmatrix} e^{\omega t} + \omega \begin{bmatrix} c_{xx} & c_{xy} \\ c_{yx} & c_{yy} \end{bmatrix} e^{\omega t} + \left( \begin{bmatrix} k_{bxx} & k_{bxy} \\ k_{byx} & k_{byy} \end{bmatrix} + \begin{bmatrix} k_{mxx} & k_{mxy} \\ k_{myx} & k_{myy} \end{bmatrix} \right) e^{\omega t} = 0 \quad (132)$$

Or,

$$\begin{bmatrix} m\omega^2 & 0 \\ 0 & m\omega^2 \end{bmatrix} + \begin{bmatrix} \omega c_{xx} & \omega c_{xy} \\ \omega c_{yx} & \omega c_{yy} \end{bmatrix} + \left( \begin{bmatrix} k_{bxx} & k_{bxy} \\ k_{byx} & k_{byy} \end{bmatrix} + \begin{bmatrix} k_{mxx} & k_{mxy} \\ k_{myx} & k_{myy} \end{bmatrix} \right) = 0 \quad (133)$$

As  $e^{\omega t} \neq 0, t \neq 0$

Or,

$$\begin{bmatrix} m\omega^2 + \omega c_{xx} + k_{bxx} + k_{mxx} & \omega c_{xy} + k_{bxy} + k_{mxy} \\ \omega c_{yx} + k_{byx} + k_{myx} & m\omega^2 + \omega c_{yy} + k_{byy} + k_{myy} \end{bmatrix} = 0 \quad (134)$$

$$\begin{aligned} m^2 \omega^4 + (m c_{xx} + m c_{yy}) \omega^3 + (m k_{bxx} + m k_{mxx} + m k_{byy} + m k_{myy} + c_{xx} c_{yy} - \\ c_{xy} c_{yx}) \omega^2 + (c_{xx} k_{byy} + c_{xx} k_{myy} + c_{yy} k_{bxx} + c_{yy} k_{mxx} - c_{xy} k_{byx} - c_{xy} k_{myx} - \\ c_{yx} k_{bxy} - c_{yx} k_{mxy}) \omega + k_{bxx} k_{byy} + k_{bxx} k_{myy} + k_{byy} k_{mxx} + k_{mxx} k_{myy} - k_{bxy} k_{byx} - \\ k_{bxy} k_{myx} - k_{mxy} k_{byx} - k_{mxy} k_{myx} = 0 \end{aligned} \quad (135)$$



Now there is considered a reference frequency  $\omega_s$  such that following relation holds.

$$\omega_s = \sqrt{\frac{F_a}{m\delta}} [76] \quad (136)$$

Here,

Total mass of rotor magnet and journal together is m.

Let consider the following.

$$\bar{\omega} = \frac{\omega}{\omega_s}, \bar{\Omega} = \frac{\Omega}{\omega_s} \quad (137)$$

Hence, the following equation is found from (135).

$$\begin{aligned} m^2 \omega_s^4 \bar{\omega}^4 + (mc_{xx} + mc_{yy})\omega_s^3 \bar{\omega}^3 + (mk_{bxx} + mk_{mxx} + mk_{byy} + mk_{myy} + c_{xx}c_{yy} - \\ c_{xy}c_{yx})\omega_s^2 \bar{\omega}^2 + (c_{xx}k_{byy} + c_{xx}k_{myy} + c_{yy}k_{bxx} + c_{yy}k_{mxx} - c_{xy}k_{byx} - c_{xy}k_{myx} - \\ c_{yx}k_{bxy} - c_{yx}k_{mxy})\omega_s \bar{\omega} + k_{bxx}k_{byy} + k_{bxx}k_{myy} + k_{byy}k_{mxx} + k_{mxx}k_{myy} - k_{bxy}k_{byx} - \\ k_{bxy}k_{myx} - k_{mxy}k_{byx} - k_{mxy}k_{myx} = 0 \end{aligned} \quad (138)$$

Using non-dimensional stiffness and damping coefficients relations from (113, 114 & 116) following equation is arrived.

$$\begin{aligned} m^2 \omega_s^4 \bar{\omega}^4 + m \frac{F_b}{\Omega \delta} (\bar{c}_{xx} + \bar{c}_{yy}) \omega_s^3 \bar{\omega}^3 + \left( m \frac{F_b}{\delta} \bar{k}_{bxx} + m \frac{F_m}{\delta} \bar{k}_{mxx} + m \frac{F_b}{\delta} \bar{k}_{byy} + \right. \\ \left. m \frac{F_m}{\delta} \bar{k}_{myy} + \frac{F_b}{\Omega \delta} \frac{F_b}{\Omega \delta} \bar{c}_{xx} \bar{c}_{yy} - \frac{F_b}{\Omega \delta} \frac{F_b}{\Omega \delta} \bar{c}_{xy} \bar{c}_{yx} \right) \omega_s^2 \bar{\omega}^2 + \left( \frac{F_b}{\Omega \delta} \frac{F_b}{\delta} \bar{c}_{xx} \bar{k}_{byy} + \frac{F_b}{\Omega \delta} \frac{F_m}{\delta} \bar{c}_{xx} \bar{k}_{myy} + \right. \\ \left. \frac{F_b}{\Omega \delta} \frac{F_b}{\delta} \bar{c}_{yy} \bar{k}_{bxx} + \frac{F_b}{\Omega \delta} \frac{F_m}{\delta} \bar{c}_{yy} \bar{k}_{mxx} - \frac{F_b}{\Omega \delta} \frac{F_b}{\delta} \bar{c}_{xy} \bar{k}_{byx} - \frac{F_b}{\Omega \delta} \frac{F_m}{\delta} \bar{c}_{xy} \bar{k}_{myx} - \frac{F_b}{\Omega \delta} \frac{F_b}{\delta} \bar{c}_{yx} \bar{k}_{bxy} - \right. \\ \left. \frac{F_b}{\Omega \delta} \frac{F_m}{\delta} \bar{c}_{yx} \bar{k}_{mxy} \right) \omega_s \bar{\omega} + \frac{F_b}{\delta} \frac{F_b}{\delta} \bar{k}_{bxx} \bar{k}_{byy} + \frac{F_b}{\delta} \frac{F_m}{\delta} \bar{k}_{bxx} \bar{k}_{myy} + \frac{F_b}{\delta} \frac{F_m}{\delta} \bar{k}_{byy} \bar{k}_{mxx} + \\ \frac{F_m}{\delta} \frac{F_m}{\delta} \bar{k}_{mxx} \bar{k}_{myy} - \frac{F_b}{\delta} \frac{F_b}{\delta} \bar{k}_{bxy} \bar{k}_{byx} - \frac{F_b}{\delta} \frac{F_m}{\delta} \bar{k}_{bxy} \bar{k}_{myx} - \frac{F_b}{\delta} \frac{F_m}{\delta} \bar{k}_{mxy} \bar{k}_{byx} - \frac{F_m}{\delta} \frac{F_m}{\delta} \bar{k}_{mxy} \bar{k}_{myx} = \\ 0 \end{aligned} \quad (139)$$

$$\begin{aligned} \bar{\omega}^4 + \frac{F_b}{F_a \Omega} (\bar{c}_{xx} + \bar{c}_{yy}) \bar{\omega}^3 + \left\{ \frac{F_b}{F_a} \bar{k}_{bxx} + \frac{F_m}{F_a} \bar{k}_{mxx} + \frac{F_b}{F_a} \bar{k}_{byy} + \frac{F_m}{F_a} \bar{k}_{myy} + \left( \frac{F_b}{F_a} \right)^2 \frac{1}{\Omega^2} \bar{c}_{xx} \bar{c}_{yy} - \right. \\ \left. \left( \frac{F_b}{F_a} \right)^2 \frac{1}{\Omega^2} \bar{c}_{xy} \bar{c}_{yx} \right\} \bar{\omega}^2 + \left\{ \left( \frac{F_b}{F_a} \right)^2 \bar{c}_{xx} \bar{k}_{byy} + \frac{F_b F_m}{F_a^2} \bar{c}_{xx} \bar{k}_{myy} + \left( \frac{F_b}{F_a} \right)^2 \bar{c}_{yy} \bar{k}_{bxx} + \frac{F_b F_m}{F_a^2} \bar{c}_{yy} \bar{k}_{mxx} - \right. \\ \left. \left( \frac{F_b}{F_a} \right)^2 \bar{c}_{xy} \bar{k}_{byx} - \frac{F_b F_m}{F_a^2} \bar{c}_{xy} \bar{k}_{myx} - \left( \frac{F_b}{F_a} \right)^2 \bar{c}_{yx} \bar{k}_{bxy} - \frac{F_b F_m}{F_a^2} \bar{c}_{yx} \bar{k}_{mxy} \right\} \frac{1}{\Omega} \bar{\omega} + \left\{ \left( \frac{F_b}{F_a} \right)^2 \bar{k}_{bxx} \bar{k}_{byy} + \right. \\ \left. \frac{F_b F_m}{F_a^2} \bar{k}_{bxx} \bar{k}_{myy} + \frac{F_b F_m}{F_a^2} \bar{k}_{byy} \bar{k}_{mxx} + \left( \frac{F_m}{F_a} \right)^2 \bar{k}_{mxx} \bar{k}_{myy} - \left( \frac{F_b}{F_a} \right)^2 \bar{k}_{bxy} \bar{k}_{byx} - \frac{F_b F_m}{F_a^2} \bar{k}_{bxy} \bar{k}_{myx} - \right. \\ \left. \frac{F_b F_m}{F_a^2} \bar{k}_{mxy} \bar{k}_{byx} - \left( \frac{F_m}{F_a} \right)^2 \bar{k}_{mxy} \bar{k}_{myx} \right\} = 0 \end{aligned} \quad (140)$$

Or,

$$\bar{\omega}^4 + A_1 \bar{\omega}^3 + A_2 \bar{\omega}^2 + A_3 \bar{\omega} + A_4 = 0 \quad (141)$$

Here,

$$A_1 = \frac{F_b}{F_a \Omega} (\bar{c}_{xx} + \bar{c}_{yy}) \quad (142)$$

$$A_2 = \frac{F_b}{F_a} \bar{k}_{bxx} + \frac{F_m}{F_a} \bar{k}_{mxx} + \frac{F_b}{F_a} \bar{k}_{byy} + \frac{F_m}{F_a} \bar{k}_{myy} + \left(\frac{F_b}{F_a}\right)^2 \frac{1}{\Omega^2} \bar{c}_{xx} \bar{c}_{yy} - \left(\frac{F_b}{F_a}\right)^2 \frac{1}{\Omega^2} \bar{c}_{xy} \bar{c}_{yx} \quad (143)$$

$$A_3 = \left\{ \left(\frac{F_b}{F_a}\right)^2 \bar{c}_{xx} \bar{k}_{byy} + \frac{F_b F_m}{F_a^2} \bar{c}_{xx} \bar{k}_{myy} + \left(\frac{F_b}{F_a}\right)^2 \bar{c}_{yy} \bar{k}_{bxx} + \frac{F_b F_m}{F_a^2} \bar{c}_{yy} \bar{k}_{mxx} - \left(\frac{F_b}{F_a}\right)^2 \bar{c}_{xy} \bar{k}_{byx} - \frac{F_b F_m}{F_a^2} \bar{c}_{xy} \bar{k}_{myx} - \left(\frac{F_b}{F_a}\right)^2 \bar{c}_{yx} \bar{k}_{bxy} - \frac{F_b F_m}{F_a^2} \bar{c}_{yx} \bar{k}_{mxy} \right\} \frac{1}{\Omega} \quad (144)$$

$$A_4 = \left(\frac{F_b}{F_a}\right)^2 \bar{k}_{bxx} \bar{k}_{byy} + \frac{F_b F_m}{F_a^2} \bar{k}_{bxx} \bar{k}_{myy} + \frac{F_b F_m}{F_a^2} \bar{k}_{byy} \bar{k}_{mxx} + \left(\frac{F_m}{F_a}\right)^2 \bar{k}_{mxx} \bar{k}_{myy} - \left(\frac{F_b}{F_a}\right)^2 \bar{k}_{bxy} \bar{k}_{byx} - \frac{F_b F_m}{F_a^2} \bar{k}_{bxy} \bar{k}_{myx} - \frac{F_b F_m}{F_a^2} \bar{k}_{mxy} \bar{k}_{byx} - \left(\frac{F_m}{F_a}\right)^2 \bar{k}_{mxy} \bar{k}_{myx} \quad (145)$$

If the polynomial equation (141) has complex conjugate roots, the imaginary part of the roots will be the non-dimensional damped natural frequency of the hybrid bearing. There exists a maximum of two such natural frequencies. Real parts of the complex conjugate roots are the non-dimensional growth frequency coefficients of the hybrid bearing. There may exist a maximum of four such growth coefficients in the case of real roots only and a minimum of two such growth coefficients in the case of complex roots only.

For the system's stability, all growth coefficients of hybrid bearing need to be less than zero. The real part of the complex root of the polynomial equation (141) needs to be zero at the stability borderline. The imaginary part of the root is considered as  $\bar{\lambda}$ . The following relation can be obtained putting  $\bar{\omega} = i\bar{\lambda}$  on the polynomial equation (141).

$$\bar{\lambda}^4 - A_1 \bar{\lambda}^3 i - A_2 \bar{\lambda}^2 + A_3 \bar{\lambda} i + A_4 = 0 \quad (146)$$

The following relations are found as the real part and imaginary part of the above (146) is separately zero.

$$\bar{\lambda}^4 - A_2 \bar{\lambda}^2 + A_4 = 0 \quad (147)$$

$$-A_1 \bar{\lambda}^3 + A_3 \bar{\lambda} = 0 \quad (148)$$

The first solution of the above relation is zero which has no interest on this contrast. The other solution is as follows

$$\bar{\lambda}^2 = \frac{A_3}{A_1} \quad (149)$$

The non-dimensional damped natural frequency at the borderline is considered  $\bar{\lambda}_1$  and  $\bar{\lambda}_2$ . The following solution is obtained.

$$\bar{\lambda}_1 = \sqrt{\frac{A_3}{A_1}} \quad (150)$$

$$\bar{\lambda}_2 = \sqrt{\frac{A_4 A_1}{A_3}} \quad (151)$$

$$\frac{A_3}{A_1} - A_2 + \frac{A_4 A_1}{A_3} = 0 \quad (152)$$

The below relation can be obtained from the above relations (142, 143, 144 & 145).

$$\frac{A_3}{A_1} = \frac{\left\{ \left( \frac{F_b}{F_a} \right)^2 \bar{c}_{xx} \bar{k}_{byy} + \frac{F_b F_m}{F_a^2} \bar{c}_{xx} \bar{k}_{myy} + \left( \frac{F_b}{F_a} \right)^2 \bar{c}_{yy} \bar{k}_{bxx} + \frac{F_b F_m}{F_a^2} \bar{c}_{yy} \bar{k}_{mxx} \right\} - \left\{ \left( \frac{F_b}{F_a} \right)^2 \bar{c}_{xy} \bar{k}_{byx} - \frac{F_b F_m}{F_a^2} \bar{c}_{xy} \bar{k}_{myx} - \left( \frac{F_b}{F_a} \right)^2 \bar{c}_{yx} \bar{k}_{bxy} - \frac{F_b F_m}{F_a^2} \bar{c}_{yx} \bar{k}_{mxy} \right\}}{\frac{F_b}{F_a \Omega} (\bar{c}_{xx} + \bar{c}_{yy})} \frac{1}{\Omega} \quad (153)$$

$$\text{Or, } \frac{A_3}{A_1} = \frac{\left\{ \frac{F_b}{F_a} \bar{c}_{xx} \bar{k}_{byy} + \frac{F_m}{F_a} \bar{c}_{xx} \bar{k}_{myy} + \frac{F_b}{F_a} \bar{c}_{yy} \bar{k}_{bxx} + \frac{F_m}{F_a} \bar{c}_{yy} \bar{k}_{mxx} \right\} - \left\{ \frac{F_b}{F_a} \bar{c}_{xy} \bar{k}_{byx} - \frac{F_m}{F_a} \bar{c}_{xy} \bar{k}_{myx} - \frac{F_b}{F_a} \bar{c}_{yx} \bar{k}_{bxy} - \frac{F_m}{F_a} \bar{c}_{yx} \bar{k}_{mxy} \right\}}{(\bar{c}_{xx} + \bar{c}_{yy})} \quad (154)$$

Or,

$$\frac{A_3}{A_1} = \frac{\left\{ F_b \bar{c}_{xx} \bar{k}_{byy} + F_m \bar{c}_{xx} \bar{k}_{myy} + F_b \bar{c}_{yy} \bar{k}_{bxx} + F_m \bar{c}_{yy} \bar{k}_{mxx} \right\} - \left\{ F_b \bar{c}_{xy} \bar{k}_{byx} - F_m \bar{c}_{xy} \bar{k}_{myx} - F_b \bar{c}_{yx} \bar{k}_{bxy} - F_m \bar{c}_{yx} \bar{k}_{mxy} \right\}}{F_a (\bar{c}_{xx} + \bar{c}_{yy})} \quad (155)$$

Or,

$$\frac{A_3}{A_1} = \frac{\left\{ F_b (\bar{c}_{xx} \bar{k}_{byy} + \bar{c}_{yy} \bar{k}_{bxx} - \bar{c}_{xy} \bar{k}_{byx} - \bar{c}_{yx} \bar{k}_{bxy}) \right\} + \left\{ F_m (\bar{c}_{xx} \bar{k}_{myy} + \bar{c}_{yy} \bar{k}_{mxx} - \bar{c}_{xy} \bar{k}_{myx} - \bar{c}_{yx} \bar{k}_{mxy}) \right\}}{F_a (\bar{c}_{xx} + \bar{c}_{yy})} \quad (156)$$

Similarly,

$$A_2 = \frac{1}{F_a} \left\{ F_b (\bar{k}_{bxx} + \bar{k}_{byy}) + F_m (\bar{k}_{mxx} + \bar{k}_{myy}) + \left( \frac{F_b^2}{F_a} \right) \frac{1}{\Omega^2} (\bar{c}_{xx} \bar{c}_{yy} - \bar{c}_{xy} \bar{c}_{yx}) \right\} \quad (157)$$

$F_m$  is not function of spin speed of journal but  $F_b$  equals to  $F_{bs}$  and directly proportional to spin speed of journal at static condition. Now,

$$\frac{F_m}{F_b} = \frac{K_m \delta \epsilon}{f_{cb} \Omega f_{bs}} \quad (158)$$

Or,

$$r_{mb} = \frac{K_m \delta \epsilon}{f_{cb} \Omega \omega_s f_{bs}} \quad (159)$$

Here,

$$r_{mb} = \frac{F_m}{F_b}, r_{ab} = \frac{F_a}{F_b} \quad (160)$$

So, the following equation can be arrived from equation (145), (152), (156) and (157).

$$\bar{\Omega}^2 = \frac{B_1(B_2 r_{mb} + B_3)}{r_{ab}(B_4 r_{mb}^2 + B_5 r_{mb} + B_6)} \quad (161)$$

Here,

$$B_1 = (\bar{c}_{xx} + \bar{c}_{yy})(\bar{c}_{xx}\bar{c}_{yy} - \bar{c}_{xy}\bar{c}_{yx}) \quad (162)$$

$$B_2 = -(\bar{c}_{xx}\bar{k}_{myy} + \bar{c}_{yy}\bar{k}_{mxx} - \bar{c}_{xy}\bar{k}_{myx} - \bar{c}_{yx}\bar{k}_{mxy}) \quad (163)$$

$$B_3 = -(\bar{c}_{xx}\bar{k}_{byy} + \bar{c}_{yy}\bar{k}_{bxx} - \bar{c}_{xy}\bar{k}_{byx} - \bar{c}_{yx}\bar{k}_{bxy}) \quad (164)$$

$$B_4 = \bar{c}_{xx}^2 \bar{k}_{mxy} \bar{k}_{myx} - \bar{c}_{xx} \bar{c}_{xy} \bar{k}_{mxx} \bar{k}_{myx} + \bar{c}_{xx} \bar{c}_{yx} \bar{k}_{myx} \bar{k}_{myy} - \bar{c}_{xx} \bar{c}_{yx} \bar{k}_{mxx} \bar{k}_{mxy} + \bar{c}_{xx} \bar{c}_{yy} \bar{k}_{mxy} \bar{k}_{myy} + \bar{c}_{xx} \bar{c}_{yy} \bar{k}_{mxx}^2 - 2\bar{c}_{xx} \bar{c}_{yy} \bar{k}_{mxx} \bar{k}_{myy} + 2\bar{c}_{xx} \bar{c}_{yy} \bar{k}_{mxy} \bar{k}_{myx} + \bar{c}_{xx} \bar{c}_{yy} \bar{k}_{myy}^2 - \bar{c}_{xy}^2 \bar{k}_{myx}^2 - 2\bar{c}_{xy} \bar{c}_{yx} \bar{k}_{mxy} \bar{k}_{myx} + \bar{c}_{xy} \bar{c}_{yy} \bar{k}_{mxx} \bar{k}_{myx} - \bar{c}_{xy} \bar{c}_{yy} \bar{k}_{myx} \bar{k}_{myy} - \bar{c}_{yx}^2 \bar{k}_{mxy}^2 + \bar{c}_{yx} \bar{c}_{yy} \bar{k}_{mxx} \bar{k}_{mxy} - \bar{c}_{yx} \bar{c}_{yy} \bar{k}_{mxy} \bar{k}_{myy} + \bar{c}_{yy}^2 \bar{k}_{mxy} \bar{k}_{myx} \quad (165)$$

$$B_5 = (\bar{k}_{bxy} \bar{k}_{myx} + \bar{k}_{byx} \bar{k}_{mxy}) \bar{c}_{xx}^2 + (\bar{k}_{byx} \bar{k}_{myy} - \bar{k}_{byx} \bar{k}_{mxx} - \bar{k}_{bxx} \bar{k}_{myx} + \bar{k}_{byy} \bar{k}_{myx}) \bar{c}_{xx} \bar{c}_{xy} + (\bar{k}_{bxy} \bar{k}_{myy} - \bar{k}_{bxy} \bar{k}_{mxx} - \bar{k}_{bxx} \bar{k}_{mxy} + \bar{k}_{byy} \bar{k}_{mxy}) \bar{c}_{xx} \bar{c}_{yx} + (2\bar{k}_{bxx} \bar{k}_{mxx} - 2\bar{k}_{bxx} \bar{k}_{myy} + 2\bar{k}_{bxy} \bar{k}_{myx} + 2\bar{k}_{byx} \bar{k}_{mxy} - 2\bar{k}_{byy} \bar{k}_{mxx} + 2\bar{k}_{byy} \bar{k}_{myy}) \bar{c}_{xx} \bar{c}_{yy} - 2\bar{k}_{byx} \bar{k}_{myx} \bar{c}_{xy}^2 + (-2\bar{k}_{bxy} \bar{k}_{myx} - 2\bar{k}_{byx} \bar{k}_{mxy}) \bar{c}_{xy} \bar{c}_{yx} + (\bar{k}_{bxx} \bar{k}_{myx} + \bar{k}_{byx} \bar{k}_{mxx} - \bar{k}_{byx} \bar{k}_{myy} - \bar{k}_{byy} \bar{k}_{myx}) \bar{c}_{xy} \bar{c}_{yy} - 2\bar{k}_{bxy} \bar{k}_{mxy} \bar{c}_{yx}^2 + (\bar{k}_{bxx} \bar{k}_{mxy} + \bar{k}_{bxy} \bar{k}_{mxx} - \bar{k}_{bxy} \bar{k}_{myy} - \bar{k}_{byy} \bar{k}_{mxy}) \bar{c}_{yx} \bar{c}_{yy} + (\bar{k}_{bxy} \bar{k}_{myx} + \bar{k}_{byx} \bar{k}_{mxy}) \bar{c}_{yy}^2 \quad (166)$$

$$B_6 = \bar{c}_{xx} \bar{c}_{yy} \bar{k}_{bxx}^2 - 2\bar{c}_{xx} \bar{c}_{yy} \bar{k}_{bxx} \bar{k}_{byy} + (\bar{c}_{yx} \bar{c}_{yy} - \bar{c}_{xx} \bar{c}_{yx}) \bar{k}_{bxx} \bar{k}_{bxy} + (\bar{c}_{xy} \bar{c}_{yy} - \bar{c}_{xx} \bar{c}_{xy}) \bar{k}_{bxx} \bar{k}_{byx} + \bar{c}_{xx} \bar{c}_{yy} \bar{k}_{byy}^2 + (\bar{c}_{xx} \bar{c}_{yx} - \bar{c}_{yx} \bar{c}_{yy}) \bar{k}_{byy} \bar{k}_{bxy} + (\bar{c}_{xx} \bar{c}_{xy} - \bar{c}_{xy} \bar{c}_{yy}) \bar{k}_{byy} \bar{k}_{byx} - \bar{c}_{yx}^2 \bar{k}_{bxy}^2 + (\bar{c}_{xx}^2 + 2\bar{c}_{xx} \bar{c}_{yy} + \bar{c}_{yy}^2 - 2\bar{c}_{xy} \bar{c}_{yx}) \bar{k}_{bxy} \bar{k}_{byx} - \bar{c}_{xy}^2 \bar{k}_{bxy}^2 \quad (167)$$

Now

$$r_{mb} = \frac{B_7}{\bar{\Omega}} \quad (168)$$

Here,

$$B_7 = \frac{K_m \delta \epsilon}{f_{cb} \omega_s f_{bs}} \quad (169)$$

Or,

$$B_7 = \frac{c_m \epsilon}{f_{bs}} \quad (170)$$

The  $c_m$  from the above equation is characteristic constant of the hybrid system of bearings which is newly introduced here and can be expressed as follows.

$$c_m = \frac{K_m \delta}{f_{cb} \omega_s} \quad (171)$$

Or,

$$c_m = c_s c_{mk} \sqrt{\frac{m}{m_0}} \quad (172)$$

Here,

Journal mass is  $m_0$ .  $c_{mk}$  and  $c_s$  are the characteristic constant of permanent magnet bearing and fluid film plain cylindrical short bearing accordingly.  $c_{mk}$  and  $c_s$  can be expressed as follows.

$$c_{mk} = \frac{2K_m \delta}{G} \quad (173)$$

$$c_s = \frac{\sqrt{G m_0}}{\mu R_b L^3} \delta^{2.5} [76] \quad (174)$$

Where,  $G$  is applied load on the journal. It is equal to  $F_a$  for hybrid system of bearings. The following equation is derived from equation (117), (160), (168) and (170).

$$r_{ab} = \sqrt{\left(1 + \frac{B_7^2}{\bar{\Omega}^2} + 2 \frac{B_7}{\bar{\Omega}} \cos \eta\right)} \quad (175)$$

Following relation is also derived from equation (117), (136), (137), (160), (168) and (170).

$$f_{bs}^2 \bar{\Omega}^2 + c_m^2 \epsilon^2 + 2c_m \epsilon f_{bs} \bar{\Omega} \cos \eta - 4c_s^2 \frac{m}{m_0} = 0 \quad (176)$$

The following relation is also true for the systems of  $n$  number of fluid film plain cylindrical short bearing.

$$\bar{\Omega} f_{bs} = \frac{2c_s}{n} \quad (177)$$

The above equation (176) and (177) are the startup curves of system of hybrid bearing and the system of plain fluid film cylindrical short bearing accordingly.

The following polynomial equation is also derived from equation ().

$$C_1 \bar{\Omega}^6 + C_2 \bar{\Omega}^5 + C_3 \bar{\Omega}^4 + C_4 \bar{\Omega}^3 + C_5 \bar{\Omega}^2 + C_6 \bar{\Omega} + C_7 = 0 \quad (178)$$

Where coefficients expressions are as follows

$$C_1 = B_6^2 \quad (179)$$

$$C_2 = 2B_7 B_6^2 \cos \eta + 2B_5 B_6 B_7 \quad (180)$$

$$C_3 = B_5^2 B_7^2 + 4B_5 B_6 B_7^2 \cos \eta + B_6^2 B_7^2 + 2B_4 B_6 B_7^2 \quad (181)$$

$$C_4 = (2B_5^2 \cos \eta + 2B_4 B_5 + 2B_5 B_6 + 4B_4 B_6 \cos \eta) B_7^3 \quad (182)$$

$$C_5 = -B_1^2 B_3^2 + B_4^2 B_7^4 + 4B_4 B_5 B_7^4 \cos \eta + 2B_4 B_6 B_7^4 + B_5^2 B_7^4 \quad (183)$$

$$C_6 = 2B_1^2 B_2 B_3 B_7 + 2 \cos \eta B_4^2 B_7^5 + 2B_4 B_5 B_7^5 \quad (184)$$

$$C_7 = -B_1^2 B_2^2 B_7^2 + B_4^2 B_7^6 \quad (185)$$

The positive real root of the solution of the equation (178) is the variable borderline speed of the hybrid system of bearings over eccentricity. The polynomial equation (178) is the borderline curve.

Hence, the characteristics of the non-dimensional borderline curve of a hybrid bearings system depend only on non-dimensional characteristics constant parameter  $c_m$ . However, the same borderline speed for fluid film plain short cylindrical bearing is almost universal for a particular length-to-diameter ratio [76].

Non-dimensional borderline speed and corresponding borderline eccentricity can be obtained as the intersection of the borderline and startup curves.

The equations (120) are also expressed in a non-dimensional form as follows.

$$\frac{1}{\omega_s} \frac{d}{dt} \begin{bmatrix} \bar{x} \\ \bar{y} \\ \dot{\bar{x}} \\ \dot{\bar{y}} \end{bmatrix} = \begin{bmatrix} \dot{\bar{x}} \\ \dot{\bar{y}} \\ \cos\alpha - \frac{1}{2} \left( \frac{\bar{\Omega F}_x}{c_s \sqrt{\frac{m}{m_0}}} - c_{mk} \bar{x} \right) \\ \sin\alpha - \frac{1}{2} \left( \frac{\bar{\Omega F}_y}{c_s \sqrt{\frac{m}{m_0}}} - c_{mk} \bar{y} \right) \end{bmatrix} \quad (186)$$

Here,

$$\bar{F}_x = \frac{F_x}{F_{cb}}, \bar{F}_y = \frac{F_y}{F_{cb}}, \dot{\bar{x}} = \frac{\dot{x}}{\omega_s \delta} = \frac{\ddot{x}}{\omega_s}, \dot{\bar{y}} = \frac{\dot{y}}{\omega_s \delta} = \frac{\ddot{y}}{\omega_s}, \ddot{\bar{x}} = \frac{1}{\omega_s} \frac{d\dot{\bar{x}}}{dt}, \ddot{\bar{y}} = \frac{1}{\omega_s} \frac{d\dot{\bar{y}}}{dt} \quad (187)$$

Equation of motion for excitation force can be expressed following way in equilibrium state [118].

$$[M]\ddot{X} + [C]\dot{X} + [K]X = \begin{bmatrix} F_H e^{-i\omega_1 t} \\ F_V e^{-i\omega_2 t} \end{bmatrix} \quad (188)$$

Where FH and FV are horizontal and vertical forces respectively and  $\omega_1$  and  $\omega_2$  are excitation frequencies, M is mass matrix, C is damping coefficient matrix and K is total stiffness matrix.

If there is only consideration of vertical Force and related forced frequency is  $\omega$ , the above equation becomes as following.

$$[M]\ddot{X} + [C]\dot{X} + [K]X = \begin{bmatrix} 0 \\ F_V \end{bmatrix} e^{-i\omega t} \quad (189)$$

Assuming harmonic form of solution which mimics the induced forced function, the solution can be expressed as

$$X = X_0 e^{-i\omega t} \quad (190)$$

So, Differentiating the followings can be found.

$$\dot{X} = -i\omega X_0 e^{-i\omega t} \quad (191)$$

$$\ddot{X} = -\omega^2 X_0 e^{-i\omega t} \quad (192)$$

Substituting the same on equation (189)

$$-\omega^2[M]X_0 - i\omega[C]X_0 + [K]X_0 = \begin{bmatrix} 0 \\ F_V \end{bmatrix} \quad (193)$$

Or,

$$X_0 = [-\omega^2[M] - i\omega[C] + [K]]^{-1} \begin{bmatrix} 0 \\ F_V \end{bmatrix} \quad (194)$$

Or,

$$\frac{X_0}{F_V} = [-\omega^2[M] - i\omega[C] + [K]]^{-1} \begin{bmatrix} 0 \\ 1 \end{bmatrix} \quad (195)$$

The above expression is the two-dimensional response of journal position in terms of non-dimensional displacement magnitude per unit non-dimensional vertical force, which is named here non-dimensional receptance. As mentioned below, the same can also be expressed as a non-dimensional form for hybrid bearing.

$$\frac{\bar{X}_0}{\bar{F}_V} = \left[ -\bar{\omega}^2[I] - i\bar{\omega}[\bar{C}] \frac{1}{r_{ab}} \sqrt{\frac{m_0}{m}} + \left[ \frac{\bar{K}_b}{r_{ab}} + \frac{r_{mb}}{r_{ab}} \bar{K}_m \right] \right]^{-1} \begin{bmatrix} 0 \\ 1 \end{bmatrix} \quad (196)$$

### 7.3 Validation of model for static load

Validation of the algorithm for solving programs using any coding is necessary as it warns of typographical program mistakes. The journal has been considered as having a constant downward vertical load and spinning motion about its axis. The present model is firstly aligned with a single fluid film plain cylindrical short bearing, putting cm as zero on equation (186) to validate it with existing numerical solutions available on past research data. The validation input parameters and output results are shown in Table 21 and Fig.45.

Static stability position is found when velocity components of the journal centre again become approximately zero after releasing the journal from the start location mentioned as “A1” in Fig. 45. The transient locus of the journal centre is shown with a brown curved line starting from point “A1” in Fig. 45. The brown line data is the validation reference data extracted from the figure of the past available research [85]. The same curve is plotted with the present model with the same input as Table 21 in same Fig. 45 to understand the validation accuracy. The colour of the transient locus as per the present model is also maintained in a colour scale mapped to the nondimensional spin speed of the journal, as shown using a colour bar in Fig.45 to understand the speed variation along the locus.

Table 21 Data used for validation

parameters	Non dimensional values
Static eccentricity	0.2
Static attitude angle	75.4°
Borderline spin speed of journal	2.688

Direction of external static load with horizontal	-90°
Running spin speed of journal (counter clockwise)	2
Coordinates of start location	0.2, - 0.3418
Characteristic constant calculated from equation (177)	0.3451

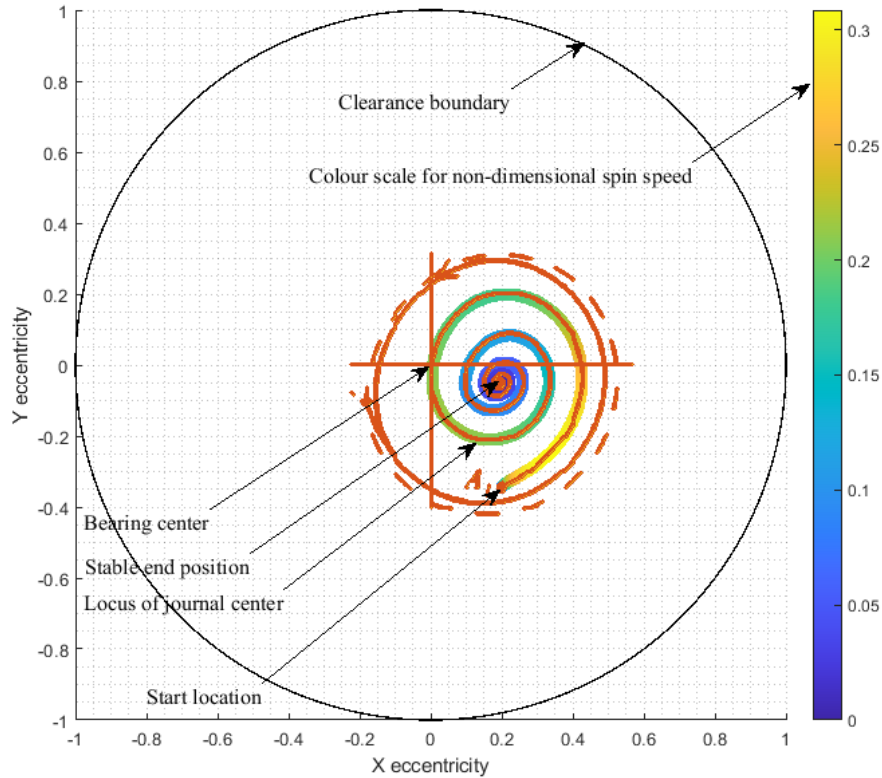


Fig.45: Validation of trajectory of the journal center position of plain cylindrical short bearing

## 7.4 Comparison results and characteristics study of hybrid system of bearings

A detailed comparison study is carried out to study the characteristics of the hybrid bearings system. The hybrid system consists of one fluid film, a plain cylindrical short bearing, and a permanent magnetic bearing. The comparison is made for a hybrid bearings system over two fluid film plain cylindrical short bearings. Thus, it is easy to understand how a hybrid bearing system shows different characteristics than two fluid film plain cylindrical short bearings do with the input parameters.

### 7.4.1 Stable position comparison

A similar method as adopted during the validation of fluid film plain short cylindrical bearing is followed here to compare results for estimating stable position. The static position is estimated using the assumed data as per Table 22.



Table 22 Data used for hybrid system of bearings

parameters	Non dimensional values
Coordinates of start location	0, 0
Journal mass plus rotor mass to journal mass ratio	1.5
Characteristic constant of fluid film cylindrical	1
Characteristic constant of hybrid system of bearings	0, 1, 3, 5, 10, 20

The details, including starting and final positions of journal centres for both systems of bearings, are shown in Fig. 46. The journal centre of the fluid film's plain short cylindrical bearing is shown in black dashed lines. Others are shown in different colours.

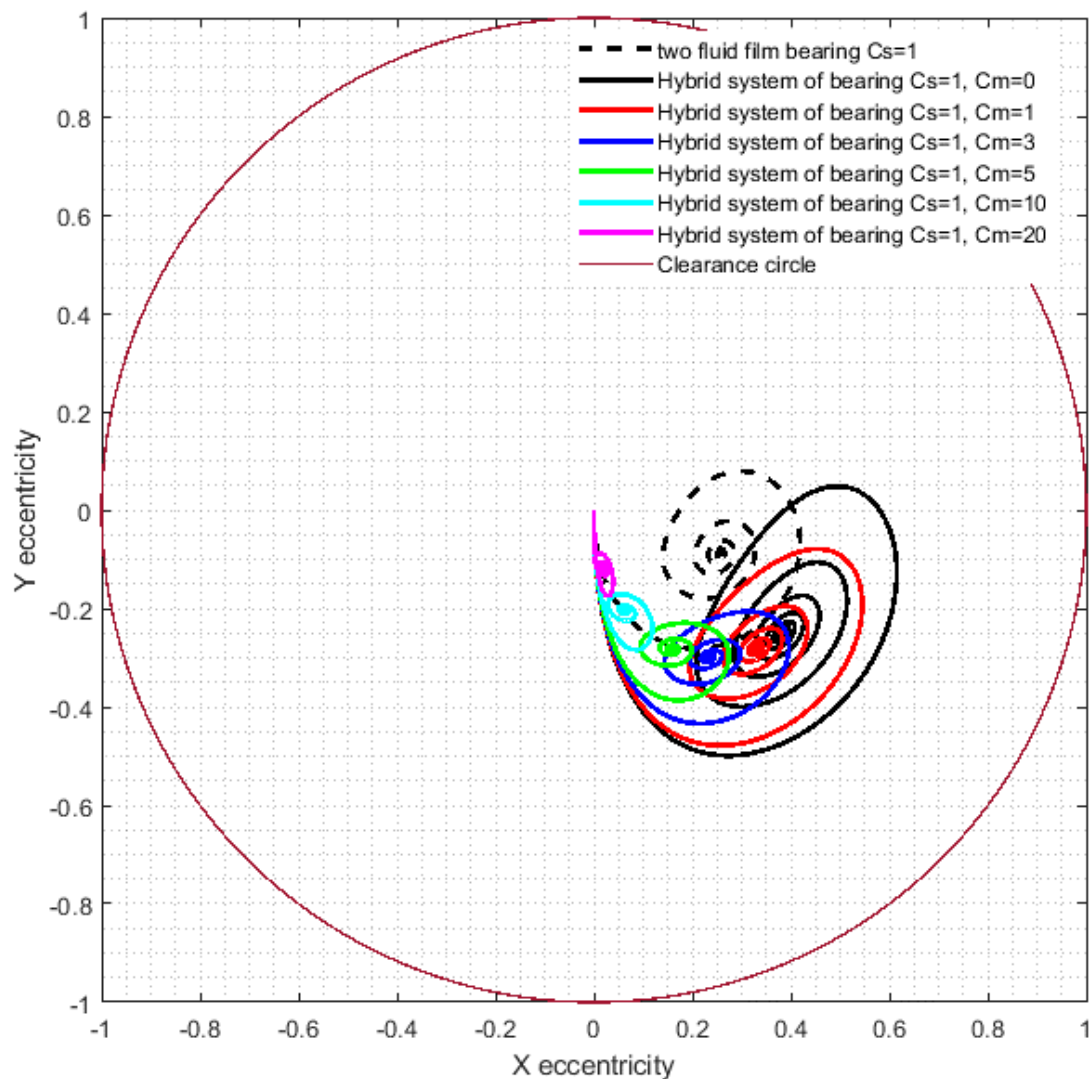


Fig.46: Trajectory of the journal center position of both plain fluid film cylindrical short bearing pair and hybrid system of bearings

To understand the above comparison with the time domain, Fig. 47 is shown the variation of eccentricity to time. The oscillation of the journal centre of hybrid bearing

is now comparable over fluid film plain short cylindrical bearing in Fig. 47. However, the journal centre position is not showing a large oscillation to time due to the above combination. The stability of eccentricity exists after some typical times, as shown in Fig. 47. This settling time depends upon the characteristics constant and mass ratio of journal mass to total rotating mass.

The high amplitude of eccentricity during the journey of oscillation is not favourable. Due to the high eccentricity value, the bearing and journal surfaces are very close together. The practical surfaces of the journal and bearing must have some irregularity in terms of surface roughness at the micron level. Hence oscillation with large amplitude is prone to bearing health.

The shorter amplitude of eccentricity oscillation of hybrid bearing means the clearance of the journal surface and bearing surface is now more than that of fluid film plain short cylindrical bearing. In this concern, essential observations are found in Fig. 46 and Fig. 47 that the eccentric position of the journal centre of a hybrid system of bearings before and after settling to zero motion is more than that of fluid film plain short cylindrical bearing depending upon the characteristics constant. This phenomenon is one of the essential characteristics for avoiding friction due to the irregularity of the surfaces.

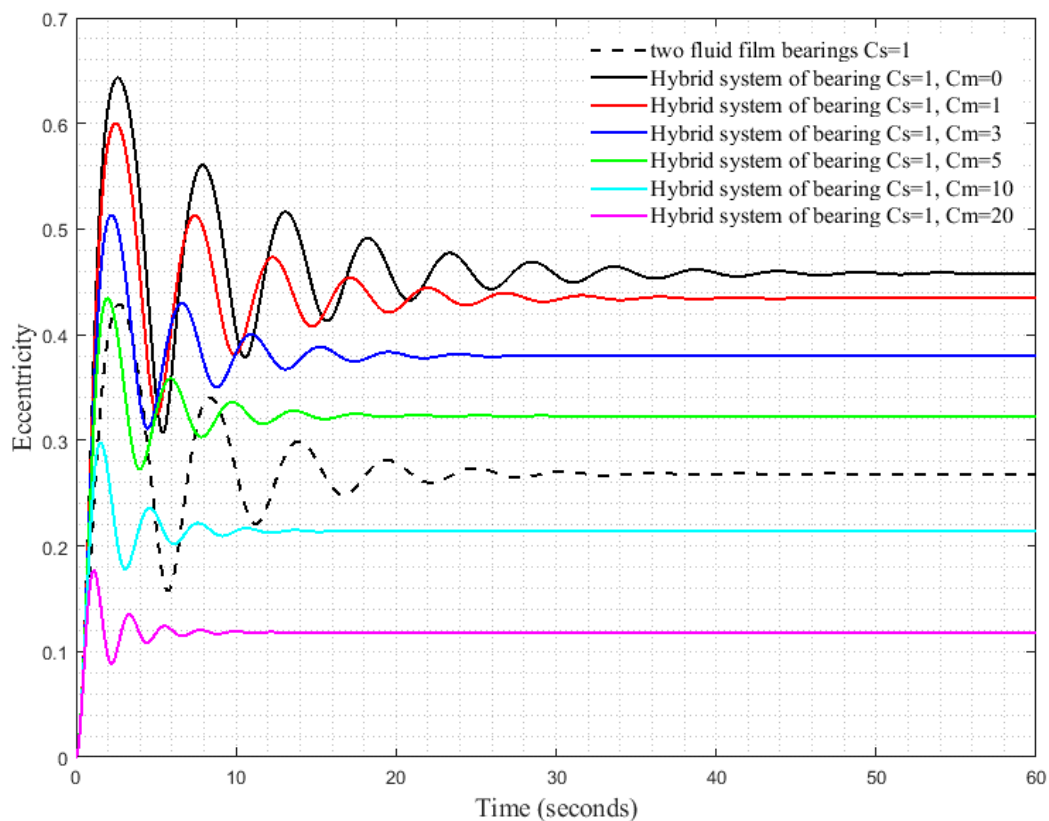


Fig.47: Eccentricity of the journal center position of both plain fluid film cylindrical short bearing pair and hybrid system of bearings

### 7.4.2 Attitude angle variation comparison

A comparison of attitude angle over time is shown in Fig. 48, considering the same data in Table 22. The attitude angle of a hybrid bearings system is lesser than that of two plain short cylindrical bearings, as shown in Fig. 48.

The characteristics curve of attitude angle over eccentricity at the stability point are shown in Fig. 49. The attitude angle curve of fluid film plain cylindrical short bearing is almost universal [76] as attitude angle is a function of eccentricity only here. The same curve of a hybrid system of bearings varies with a change of speed and applied load or both if the geometric and other parameters of the hybrid bearing are constant. The attitude angle becomes zero much early before it reaches zero if the magnetic bearing reaction contribution is biased by increasing the value of the characteristic constant of a hybrid bearings system. A similar behaviour of attitude angle variation is also reported in some recent research [105] which is close to one of this kind of bearings arrangement as expected from the derived mathematical expression (118). That is not precisely similar to the force of the electromagnetic bearing model [105] and is not linear with eccentricity. Hence, stiffness is not approximately constant and not applicable to this proposed model.

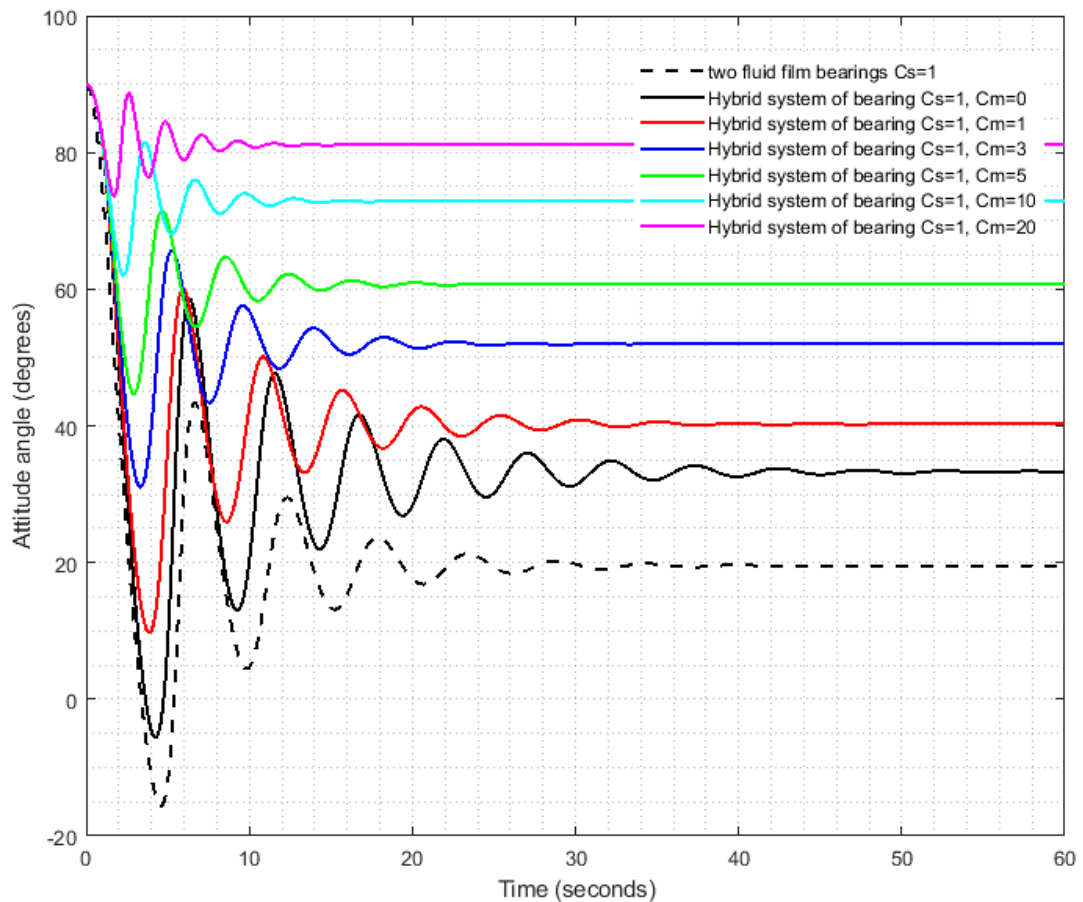


Fig.48: Attitude angle of the journal center position of both plain fluid film cylindrical short bearing pair and hybrid system of bearings

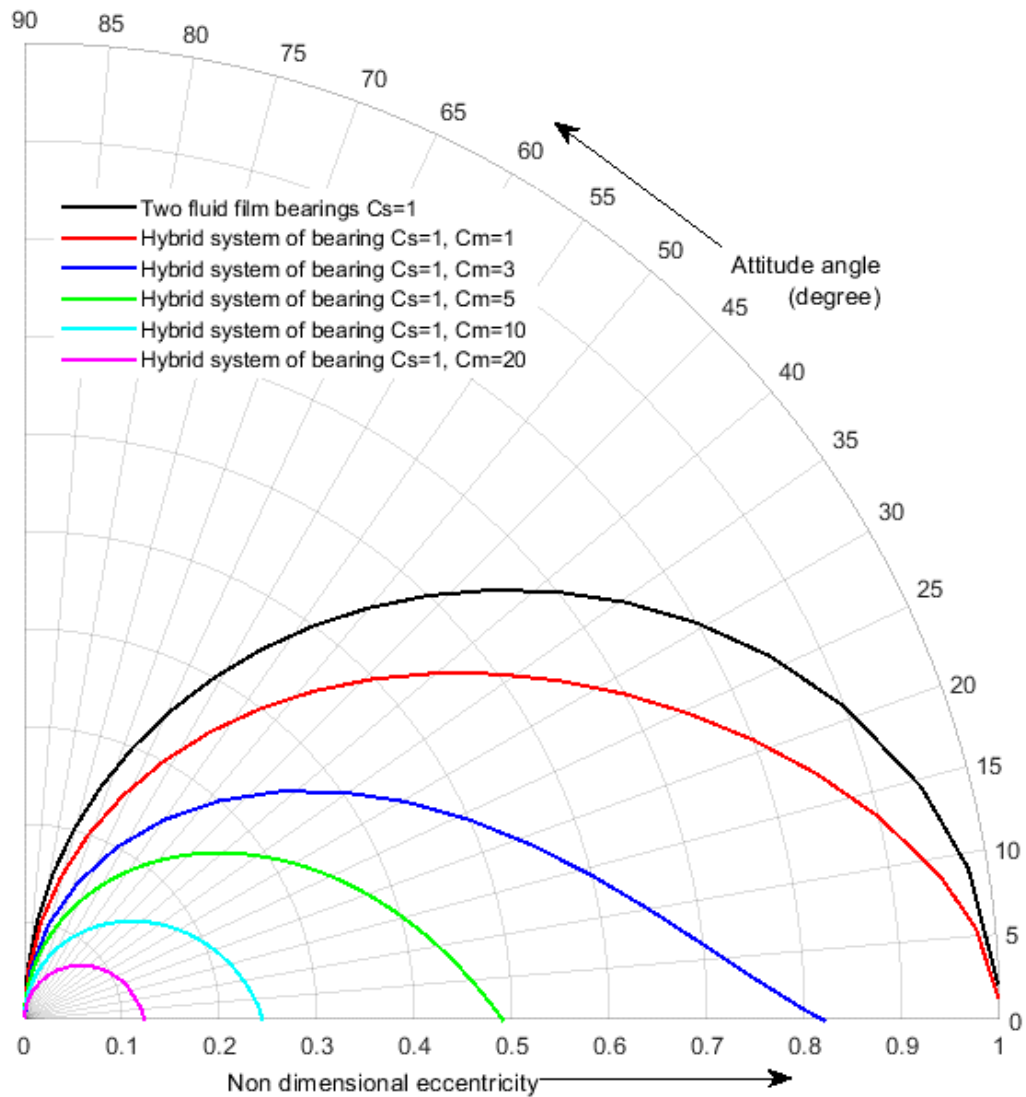


Fig.49: Polar plot of attitude angle variation with non-dimensional eccentricity for different characteristic constant of hybrid system of bearings

Another study is carried on as per subset data in table 22. The attitude angle of a hybrid bearings system is dependent on both journal's spin speed and eccentricity simultaneously, as shown in Fig. 50. White region of Fig. 50 is the unstable zone for this particular hybrid bearings system. Constant attitude angle levels in lines are also shown with the colour scale in Fig. 50.

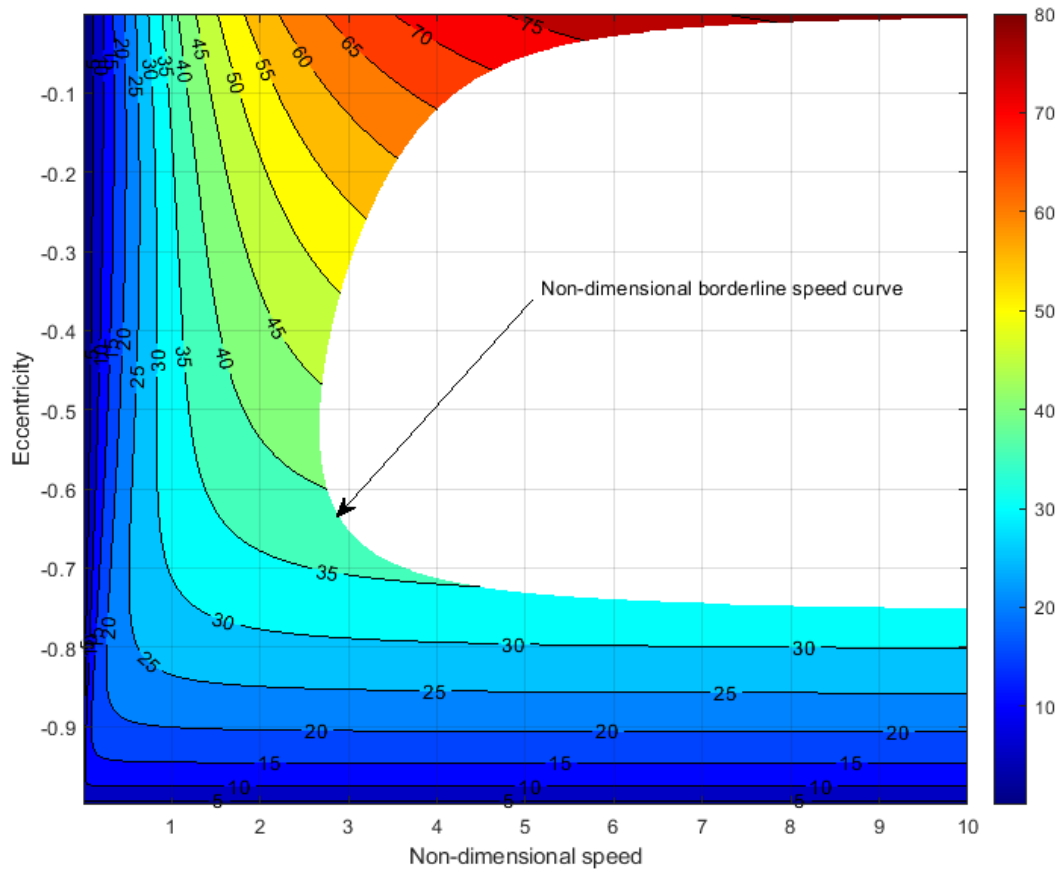


Fig.50: Contour plot of attitude angle variation for hybrid system of bearings ( $C_m = 2$ )

### 7.4.3 Bearing Load capacity ratio of hybrid system of bearings to incompressible fluid film short bearings system

Fig. 51 shows the bearing load capacity ratio between the two systems of bearings. The bearing load capacity ratio of hybrid system bearings to the similar double fluid film bearings system is more than one when non-dimensional speed is approximately less than one and eccentricity is also approximately 0.05 to 0.25. The characteristic constant of fluid film short cylindrical bearing of a hybrid system of bearings need not be the same at different sets of eccentricity and speed combinations. It has to maintain a fixed characteristic constant of value 2 for a hybrid system of bearing and mass ratio 1.44 by considering it as an example. This mass ratio is more than one to simulate extra mass due to the addition of a rotor magnet. It may be concluded with this example, as shown in Fig. 51, that the load capacity of a hybrid system of bearing can be increased when there is such a demand at low speed and eccentricity under the constraint of fixed mass ratio and characteristic constant of a hybrid system of bearings.

However, this will not be that useful concerning load carrying capacity while there is a demand for non-dimensional spin speed of journal more than one under the same constraints. This phenomenon is similar in Fig. 52, where the magnetic bearing load

carrying participation becomes less at the regions under low speed and high eccentricity.

The role of attitude angle on bearing resultant load capacity is easily understood from Fig. 44 and equation (117). This phenomenon is further explained in Fig. 53 with other typical examples. Here the fractional force components along the resultant load of both bearings of a hybrid system are plotted over eccentricity. Other orthogonal components will be the same and opposite to each other under equilibrium and stable conditions.

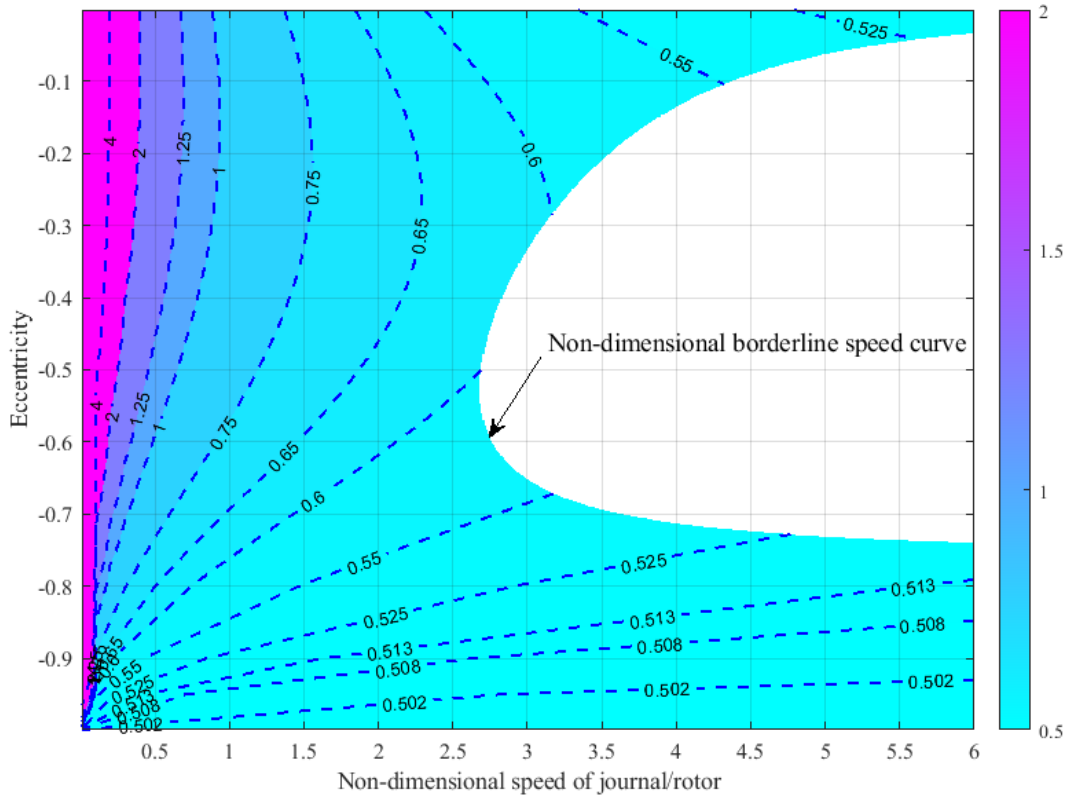


Fig. 51: Contour plot of bearing load capacity ratio of hybrid system of bearings to double fluid film short bearings system over non-dimensional speed and eccentricity for a typical hybrid system of bearings ( $C_m = 2.4$ , mass ratio = 1.44)

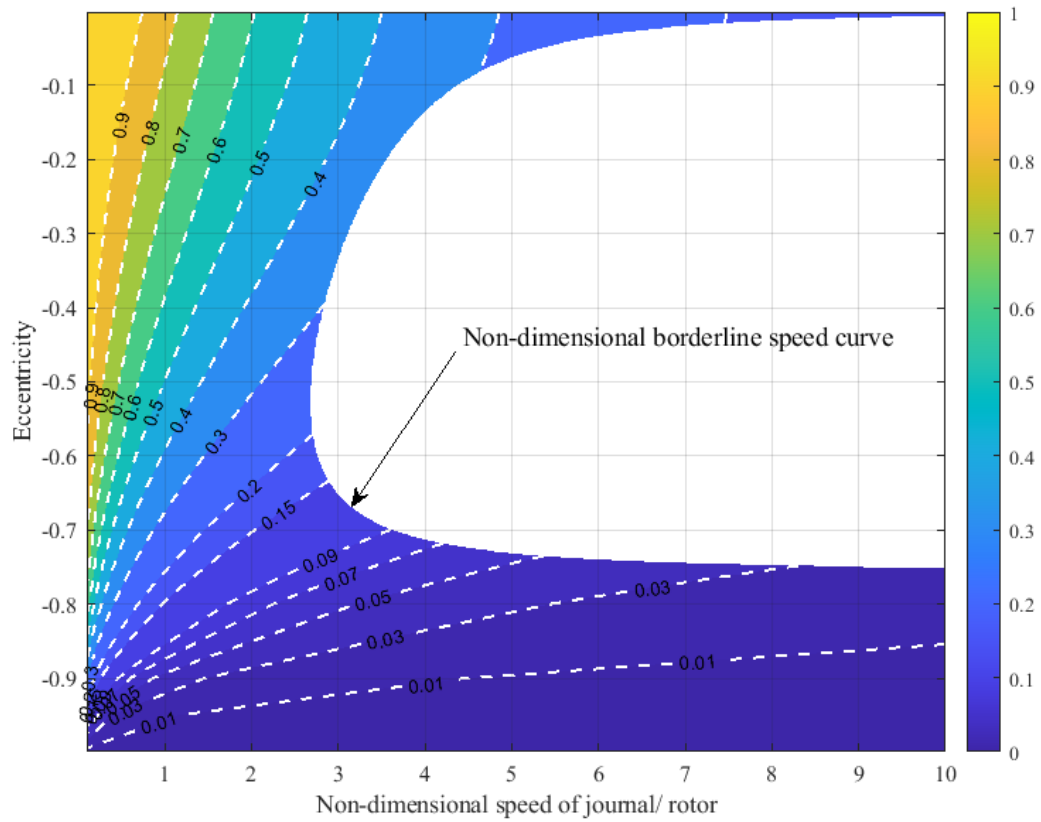


Fig. 52: Contour plot of magnetic force to total load ratio variation over non-dimensional speed and eccentricity for hybrid system of bearings ( $C_m = 2.4$ , mass ratio = 1.44)

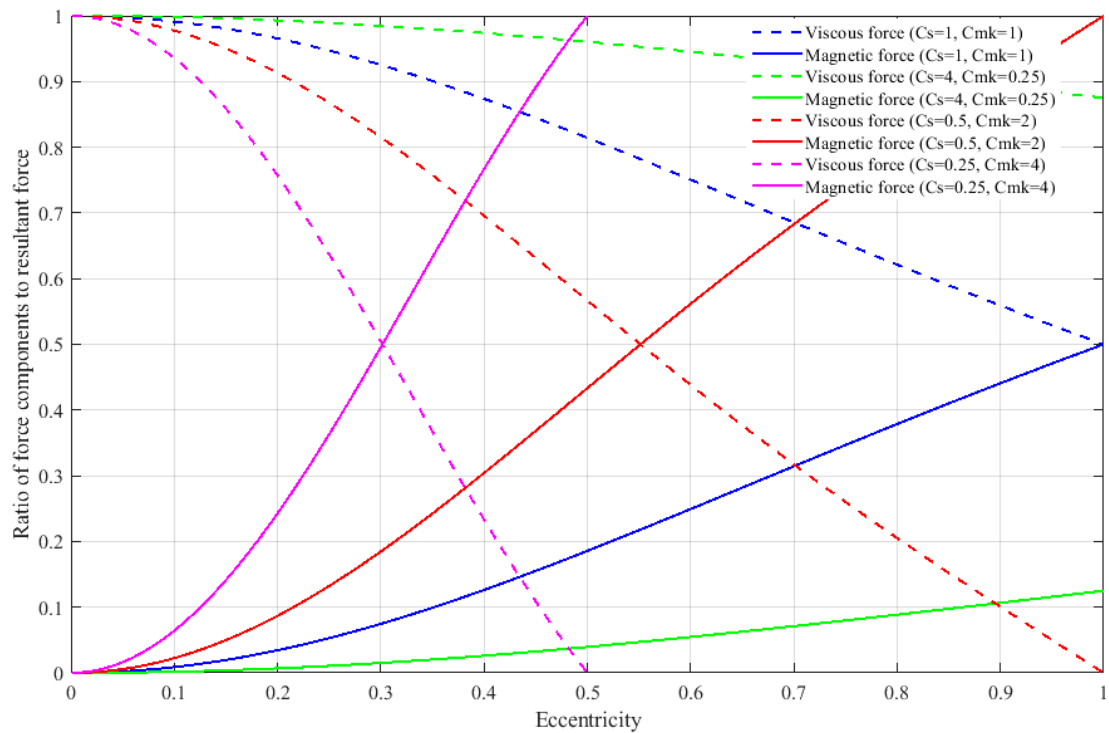


Fig. 53: Force components ratio comparisons for various characteristics mixing of fundamental bearings to hybrid system of bearings ( $C_m = 1.2$  and mass ratio = 1.44)

#### 7.4.4 Natural frequency comparison

The variations of non-dimensional natural frequency are plotted over the non-dimensional spin speed of the journal/ rotor. Fig. 54 shows that the natural frequencies of two fluid film bearings systems are less than the spin speed of the journal. Here, the natural frequency curve of a hybrid system of bearings crosses the equal spin speed line at different points, indicating that the natural frequencies of a hybrid system of bearings are somewhere more or less equal to the non-dimensional spin speed of the journal.

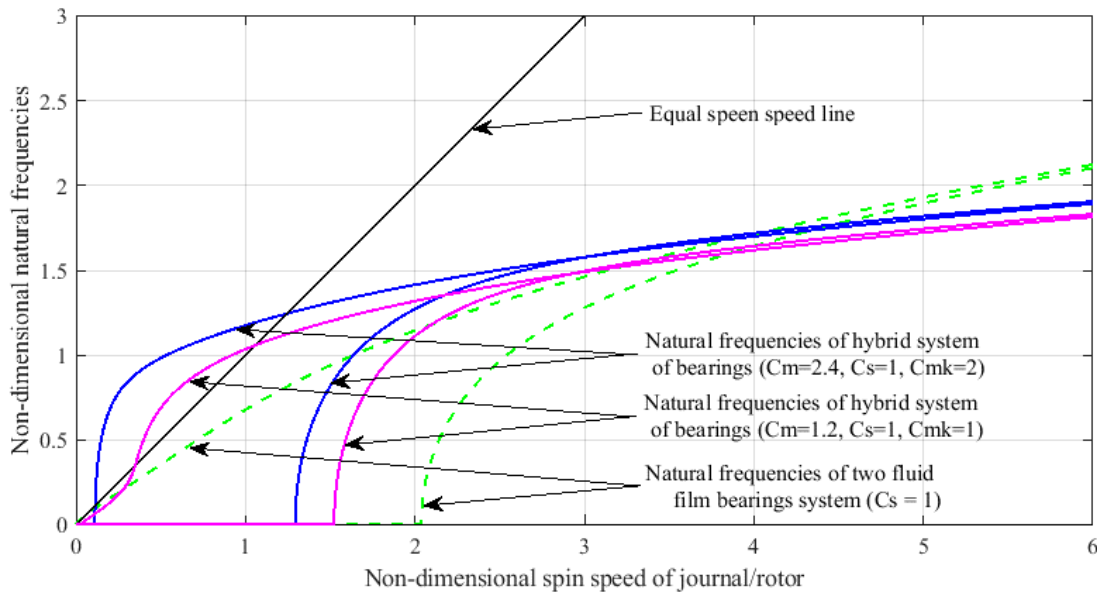


Fig. 54: Variation of non-dimensional natural frequency with respect to non-dimensional spin speed of journal/ rotor

The relevant characteristic constants of all systems of bearings are also shown in Fig.54. The designer has to choose the characteristic constants so that the journal's non-dimensional working spin speed is not equal or nearly equal to the natural frequency of the system. This choice is to avoid resonance during working speed.

#### 7.4.5 Stability comparison for static load

The variations of non-dimensional growth coefficients are plotted over the non-dimensional spin speed of the journal/ rotor. A stability comparison is also carried out considering the typical characteristic constant of a hybrid system of bearings, as shown in Fig. 55. The limit of the non-dimensional spin speed of the journal of a hybrid system of bearings is at the point where the horizontal axis passing through the origin crosses with the growth coefficient curve. The limit of journal spin speed of fluid film plain cylindrical short bearing is 2.671. The growth coefficients curve of two fluid film cylindrical short bearings systems are shown in the dashed green line in Fig. 55, the same as standard [76]. Similarly, the limits for a hybrid system of bearings are 2.791 and 3.037 for different characteristic constants of a hybrid system of bearings, as shown



in the pink and blue curve in Fig. 55. Stability of the bearing loses above the limit of spin speed as the growth coefficients of bearings have not negative sign.

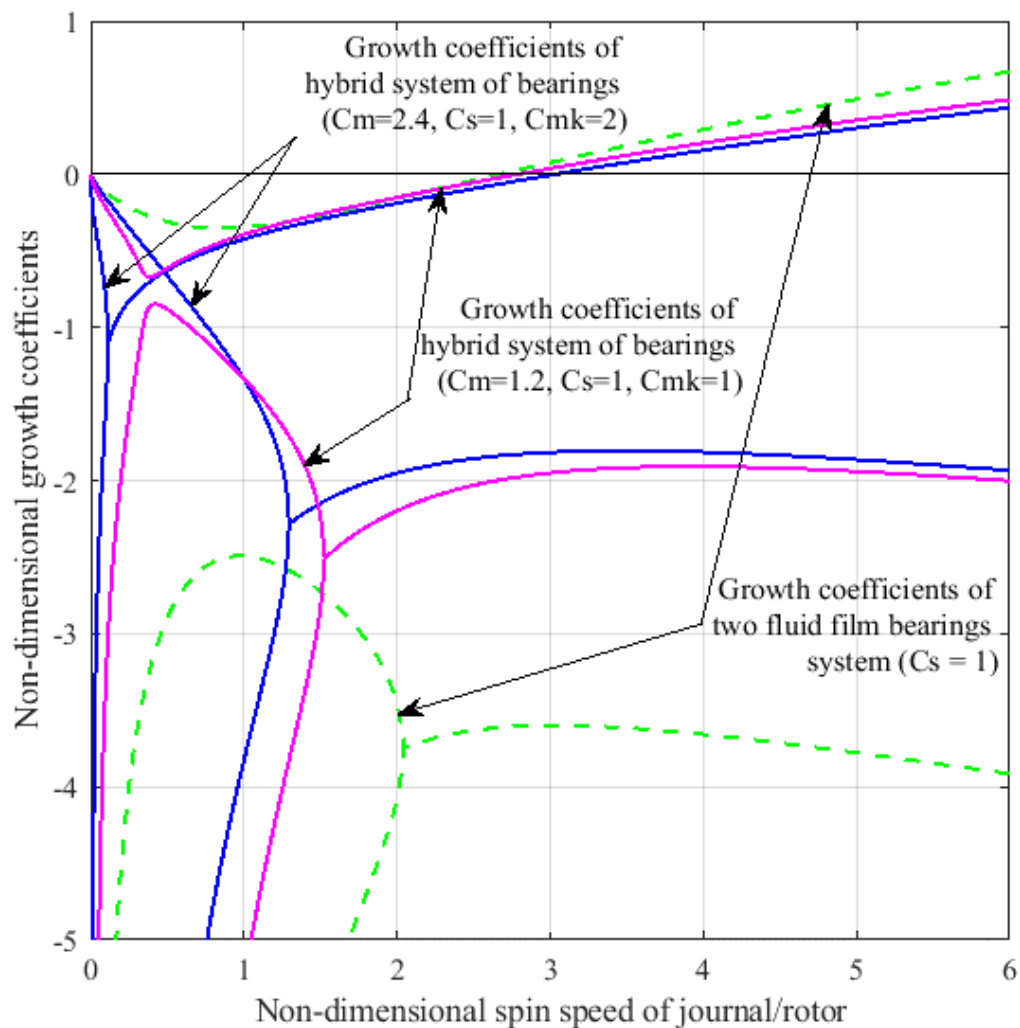


Fig. 55: Variation of non-dimensional growth coefficients with respect to non-dimensional spin speed of journal

Another plot is shown in Fig. 56 for presenting the borderline speed curve and startup curve of a different hybrid system of bearings and double fluid film bearings system. The startup curve of each system bearing differs with the change of characteristic constants of bearings. The stability border point of a particular system of bearings is found at the intersection of the startup curve with the borderline curve. The stability borderline speed curve of the double fluid film short cylindrical bearings system is shown in the red curved standard line [76] in Fig. 56.

The borderline stability curve is a function of the bearing system's geometric and other internal properties. Fig. 56 shows that the area of the stability zone of the hybrid system of bearings has more coverage area than the area of two fluid film plain cylindrical short bearings systems. The unstable zone is enclosed by a borderline speed curve, as shown in Fig. 56 and Fig. 50, Fig. 51 and Fig. 52 as a white region. The hybrid bearing

systems can operate an extended range of spin speed of journal at low eccentricity compared with the same two fluid film plain cylindrical short bearings system.

Borderline speed curves of hybrid systems of bearings and two fluid film plain cylindrical short bearings systems have overlapped each other at an eccentricity of 0.756. This phenomenon is shown in the dashed black line in Fig. 56. A contour plot of the borderline speed of the hybrid bearings system is shown in Fig. 57 by assuming the typical mass ratio of total rotary mass to journal mass as 1.44.

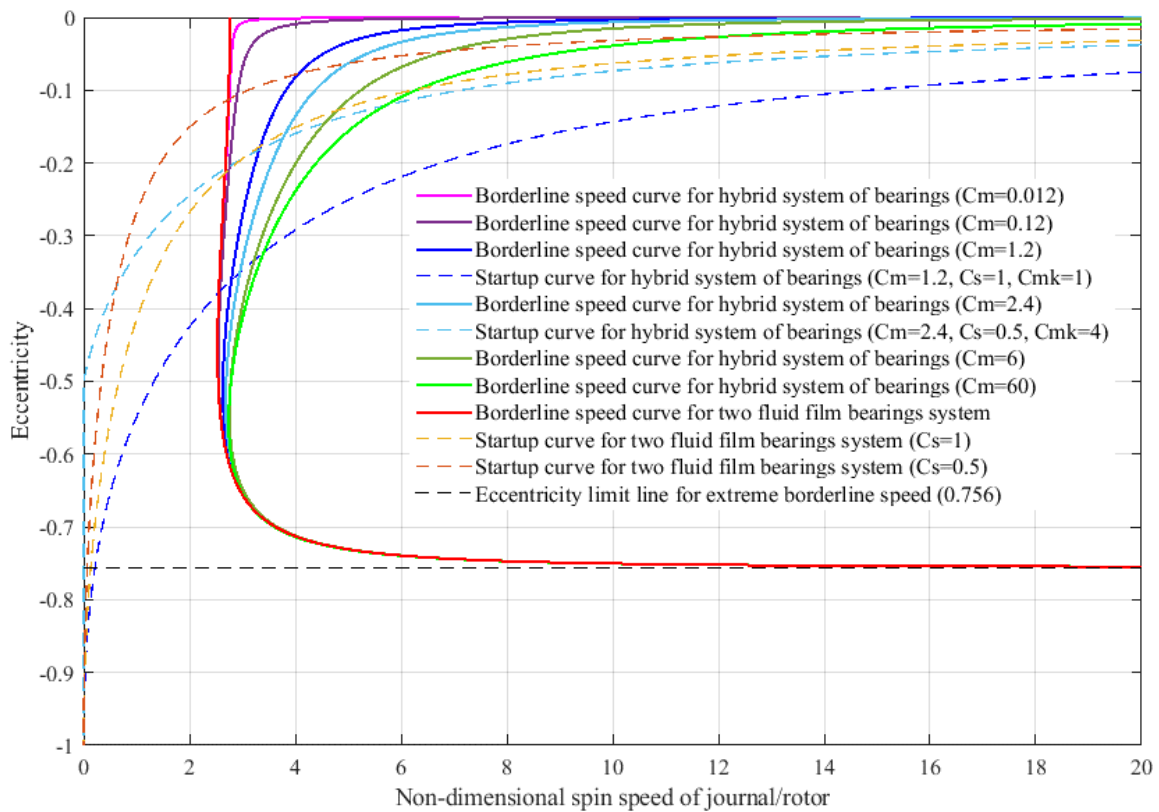


Fig. 56: Borderline of stability and start up curve comparisons between hybrid system of bearings over two fluid film bearings system

Characteristic constants of magnetic bearing and fluid film cylindrical short bearing vary in the horizontal and vertical axis of Fig. 57. This type of plots information will be helpful to the designer in choosing the mixing characteristics constants of a hybrid system of bearings to achieve the desired maximum non-dimensional spin speed of journal.

Another similar contour plot of eccentricity at maximum borderline speed is shown in Fig. 58. This kind of information will be significant when the designer tries to limit the eccentricity at maximum speed, maintaining a desired radial gap between the journal and bearing.

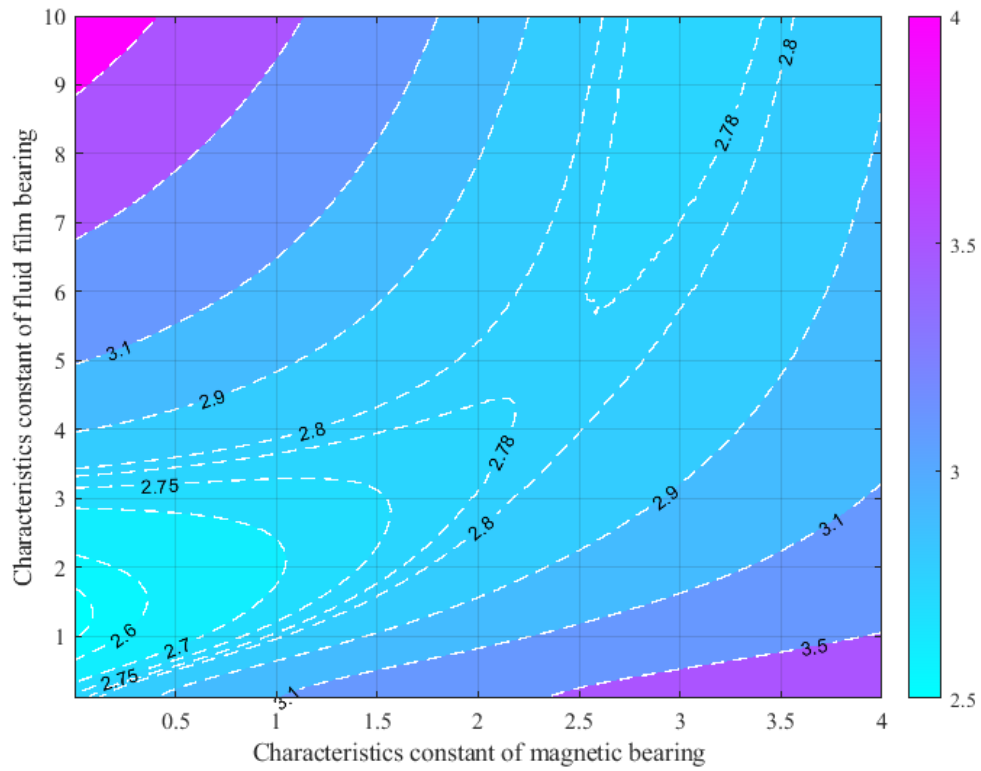


Fig. 57: Non-dimensional boundary speed variation over characteristic's constants of hybrid systems of bearing

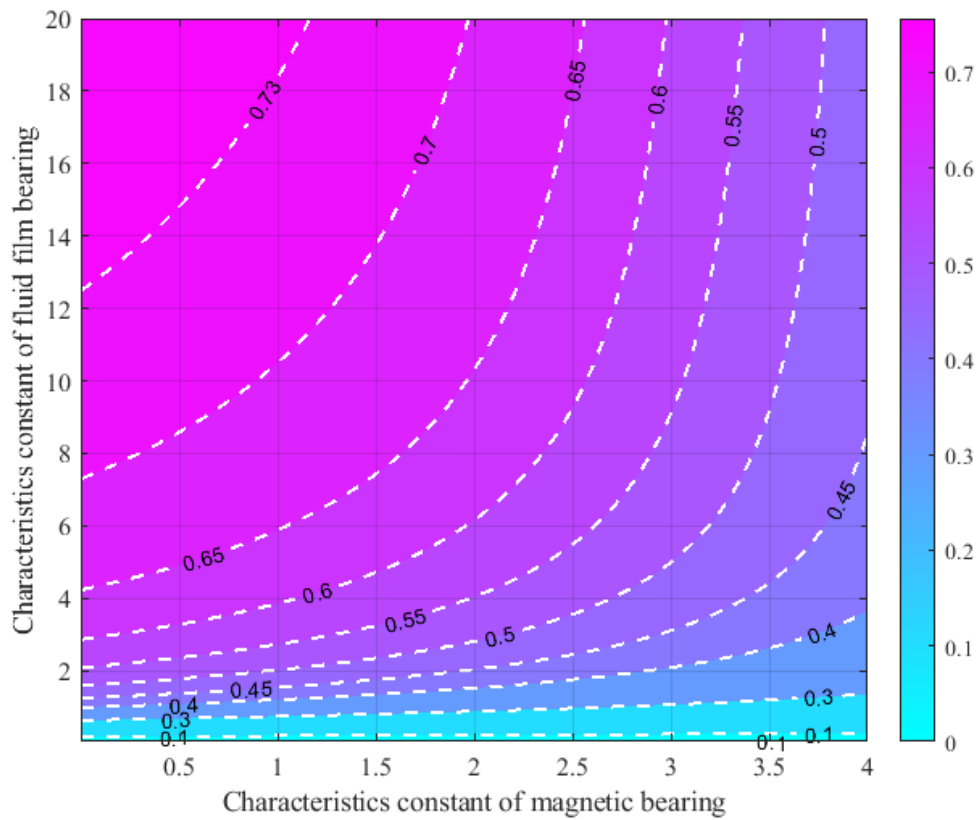


Fig. 58: Minimum eccentricity variation over characteristic's constants of hybrid systems of bearing occurred at boundary speed

### 7.4.6 Forced frequency response comparison for vertical harmonic excitation

A frequency response comparison study is carried out under a downward vertical excitation. The hybrid bearing system is becoming stiffer due to the addition of stiffness of permanent magnetic bearing. There has been no additional damping considered due to magnetic bearing. Hence, this type of bearing is typically more than the response of two fluid film bearings systems. Non-dimensional vertical and horizontal receptance over various non-dimensional spin speeds of the journal is shown in Fig. 59 and Fig. 60 to understand the response comparison of a hybrid system of bearing over two fluid film bearings systems. All the responses are due to vertical harmonic excitation, which matches the non-dimensional spin speed of the journal. Fig. 59 shows more responses for the hybrid system of bearing than another one due to harmonic excitation vertical load for typical characteristic constant. The dynamic responses, as shown in Fig. 60, are not similar patterns as shown in Fig. 59 because of stiffness and damping matrix coefficients contribution to the dynamics are different for the vertical and horizontal directions.

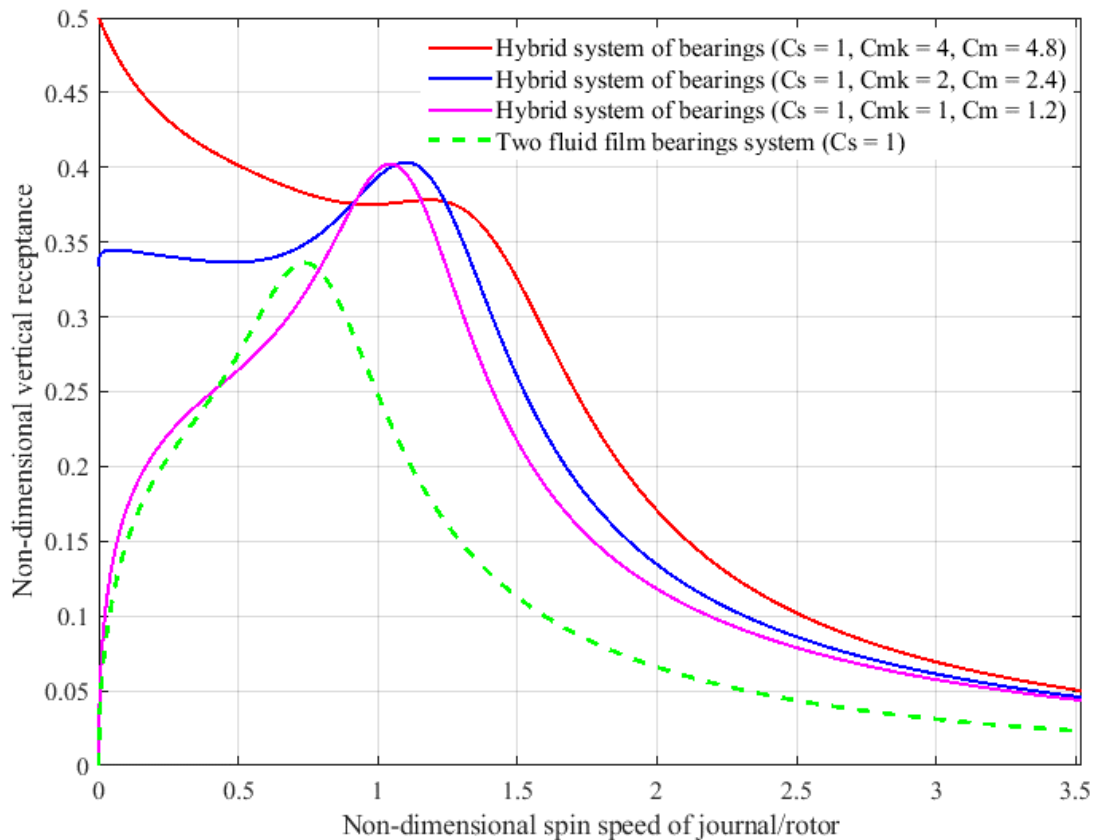


Fig. 59: Absolute vertical non-dimensional receptance of both system of bearings for vertical harmonic force

The responses of the bearings show the highest peak close to their damped natural frequency while plotting to the non-dimensional spin speed of the journal. Figures Fig. 59 and Fig. 60 show three types of characteristic constant combinations for a hybrid

system of bearing with a fluid film bearing system shown in different colour response lines. The lower response of the bearing system is desired as it reduces the chance of surface damage due to collision and rubbing between bearing and journal surfaces during harmonic excitation.

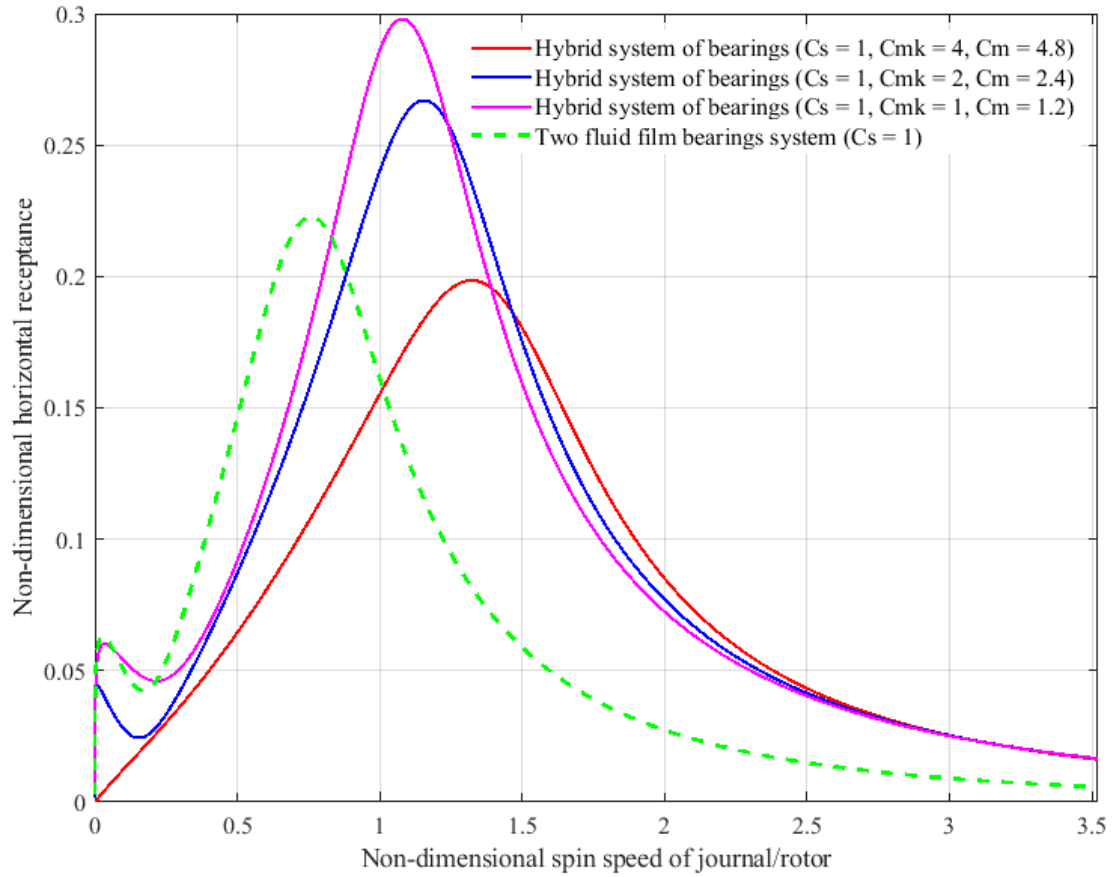


Fig. 60: Absolute horizontal non-dimensional receptance of both system of bearings for vertical harmonic force

## 7.5 Summary

This work presents a detailed analytical model for finding the behaviour of a hybrid system of journal-bearing setup. This analytical model with a similar schematic configuration can help the designer decide the use of this type of hybridization as per the required design objective and constraint. This finding can quantify the conditions of improving the stability zone, increasing the borderline spin speed of the journal, and increasing the excitation load capacity of a hybrid system of bearing over fluid film plain cylindrical short bearings system. This analytical model also invites further investigation scope for the character study of the different geometric structures of bearings with more degrees of freedom.

## **8. End conclusion and future scope of work**

### **8.1 Conclusions**

The thesis presents a detailed study of journal-bearing systems. It includes a statistical and graphical comparison of errors and computational time on non-dimensional journal force estimation for short cylindrical bearings. It also presents a numerical method for estimating hydrodynamic journals bearing characteristic parameters under static equilibrium. The writing presents a simple method of non-dimensional modelling using a simple permanent magnetic bearing configuration. The article also presents a semi-analytic and finite element approach that differs from past available methods. Finally, the report presents a detailed numerical model for finding the behaviour of a hybrid system of journal-bearings and permanent magnet bearings setup.

### **8.2 Suggestions for potential future work**

Develop a more comprehensive model considering thermal load for estimating hydrodynamic journal-bearing characteristic parameters. The current model is based on a simplified assumption of static equilibrium without using any thermal load. A more comprehensive model could consider the effects of thermal loads, wear, and other factors, which would provide more accurate estimates of bearing performance and could be used to design more reliable bearings.

Investigate the use of probabilistic approaches for estimating non-dimensional natural frequencies. The current study uses a deterministic approach to estimate non-dimensional natural frequencies. However, probabilistic approaches, such as the Monte Carlo Integration method, could be used to consider the uncertainty in the input parameters. This would provide more realistic estimates of bearing stability.

Develop a more sophisticated algorithm for optimizing radial magnetic force. The current algorithm is a simple one-step optimization algorithm. A more sophisticated algorithm could be used to find the global optimum of the radial magnetic force. Considering all interfaces with PMB, A parametric study with feature engineering could lead to the design of more efficient permanent magnetic bearings.

Investigate the effect of viscous damping on the stability of hybrid journal bearings. The current study and model do not consider the effect of viscous damping except for fluids viscous damping. However, viscous damping can significantly affect the stability of bearings. Investigating the effect of additional viscous damping using active magnetic bearing could provide more insights into the design of hybrid journal bearings.

Develop a more general analytical model for a hybrid system of journal bearings and

magnetic bearings. The current analytical model is specific to a particular type of hybrid journal bearing. A more general model could be developed. This might be applied to a broader range of hybrid journal bearings with 6-DOF that would be a valuable tool for bearing designers. Similar methods can be applied on hybrid-system of AMB and fluid film journal bearing or PMB with pneumatic bearing.

# References

- [1] E. Krämer. Foundation. Dynamics of Rotors and Foundations, 261-291, (1993). [https://doi.org/10.1007/978-3-662-02798-1\\_19](https://doi.org/10.1007/978-3-662-02798-1_19)
- [2] S. Sarkar, A. Nandi, S. Neogy, J. K. Dutt, T. K. Kundra. Finite element analysis of misaligned rotors on oil-film bearings. *Sadhana*, 35(1), 45-61 (2010). <https://doi.org/10.1007/s12046-010-0005-1>
- [3] T. H. Machado, K. L. Cavalca. Evaluation of dynamic coefficients for fluid journal bearings with different geometries. *Proceedings of COBEM* (2009). <https://www.abcm.org.br/app/webroot/anais/cobem/2009/pdf/COB09-0722.pdf>
- [4] Marco T. C. Faria. Finite element analysis of oil-lubricated elliptical journal bearings, *Apr.* (2015). <https://doi.org/10.5281/zenodo.1100549>
- [5] W.B. Rowe, F.S. Chong. Computation of dynamic force coefficients for hybrid (hydrostatic/hydrodynamic) journal bearings by the finite disturbance and perturbation techniques. *Tribology International*, 19(5), 260-271 (1986). [https://doi.org/10.1016/0301-679x\(86\)90005-8](https://doi.org/10.1016/0301-679x(86)90005-8)
- [6] H. Hirani. *Fundamentals of Engineering Tribology with Applications*. Journal not available, (2016). <https://doi.org/10.1017/cbo9781107479975>
- [7] S. Sarkar, A. Nandi and S. Neogy. Determination of journal position of an indeterminate rotor on oil film bearings subjected to static load. *International Conference on System Dynamics and Control -ICSDC*, (2010). [https://www.academia.edu/8265708/determination\\_of\\_journal\\_position\\_of\\_an\\_indeterminate\\_rotor\\_on\\_oil\\_film\\_bearings\\_subjected\\_to\\_static\\_load](https://www.academia.edu/8265708/determination_of_journal_position_of_an_indeterminate_rotor_on_oil_film_bearings_subjected_to_static_load)
- [8] P. Raymond Canale and S. C. Chapra. *Numerical Methods for Engineers* (1st ed.). McGraw-Hill Education (1985).
- [9] G. W. Stachowiak, A. W. Batchelor. *Computational Hydrodynamics*. *Engineering Tribology*, 205-259, (2006). <https://doi.org/10.1016/b978-075067836-0/50006-7>
- [10] R. G. Budynas and J. K. Nisbett. *Shigley's Mechanical Engineering Design* (10th ed.), McGraw-Hill Education, (2010).
- [11] D. Sfyris, A. Chasalevris. An exact analytical solution of the Reynolds equation for the finite journal bearing lubrication. *Tribology International*, 55, 46-58 (2012). <https://doi.org/10.1016/j.triboint.2012.05.013>
- [12] V. B. Bhandari. *Design of Machine Elements*. McGraw-Hill Education (2010).
- [13] R. Tiwari. *Rotor Systems: Analysis and Identification* (1st ed.). CRC Press (2017). <https://doi.org/10.1201/9781315230962>
- [14] A. A. Raimondi, John Boyd. A solution for the finite journal bearing and its application to analysis and design: I. *ASLE Transactions*, 1(1), 159-174 (1958). <https://doi.org/10.1080/05698195808972328>
- [15] J. W. Lund. Review of the Concept of Dynamic Coefficients for Fluid Film Journal Bearings. *Journal of Tribology*, 109(1), 37-41 (1987). <https://doi.org/10.1115/1.3261324>
- [16] W. Zhou, X. Wei, L. Wang, Guangkuan Wu. A superlinear iteration method for



- calculation of finite length journal bearing's static equilibrium position. *Royal Society Open Science*, 4(5), 161059 (2017). <https://doi.org/10.1098/rsos.161059>
- [17] J. W. Lund and K. K. Thomsen. A Calculation Method and Data for the Dynamic Coefficients of Oil-Lubricated Journal Bearings. In *Topics in Fluid Film Bearing and Rotor Bearing System Design and Optimization*, ASME, New York, 1-25 (1978).
  - [18] E. Omidreza, P. M. Zissimos, V. Nickolas & V. Kumar. Calculation of Journal Bearing Dynamic Characteristics Including Journal Misalignment and Bearing Structural Deformation. *Tribology Transactions*, 47(1), 94-102 (2005), <https://doi.org/10.1080/05698190490278994>
  - [19] P. Huang. *Numerical Calculation of Elastohydrodynamic Lubrication: Methods and Programs*. 1st ed. John Wiley & Sons Inc. ISBN: 1118920961, (2015).
  - [20] A. Chasalevris, D. Sfyris. Evaluation of the finite journal bearing characteristics, using the exact analytical solution of the Reynolds equation. *Tribology International*, 57, 216-234 (2013). <https://doi.org/10.1016/j.triboint.2012.08.011>
  - [21] D. M. Causon, C. G. Mingham, and Ventus Publishing ApS. *Introductory Finite Difference Methods for PDEs*. ISBN: 978-87-7681-642-1 (2010).
  - [22] J.-P. Yonnet. Passive magnetic bearings with permanent magnets. *IEEE Transactions on Magnetics*, 14(5), 803-805 (1978). <https://doi.org/10.1109/tmag.1978.1060019>
  - [23] K. W. Yung, P. B. Landecker, D. D. Villani. An Analytic Solution for the Force Between Two Magnetic Dipoles. *Magnetic and Electrical Separation*, 9(1), 39-52 (1998). <https://doi.org/10.1155/1998/79537>
  - [24] M. D. Simon, L. O. Heflinger, S. L. Ridgway. Spin stabilized magnetic levitation. *American Journal of Physics*, 65(4), 286-292 (1997). <https://doi.org/10.1119/1.18488>
  - [25] Q. Tan, W. Li, B. Liu. Investigations on a permanent magnetic–hydrodynamic hybrid journal bearing. *Tribology International*, 35(7), 443-448 (2002). [https://doi.org/10.1016/s0301-679x\(02\)00026-9](https://doi.org/10.1016/s0301-679x(02)00026-9)
  - [26] S.M. Muzakkir, K.P. Lijesh, H. Hirani. Tribological failure analysis of a heavily-loaded slow speed hybrid journal bearing. *Engineering Failure Analysis*, 40, 97-113 (2014). <https://doi.org/10.1016/j.engfailanal.2014.02.016>
  - [27] B. Paden, N. Morse, R. Smith. Magnetic bearing experiment for integrated teaching and research laboratories. *Proceeding of the 1996 IEEE International Conference on Control Applications IEEE International Conference on Control Applications held together with IEEE International Symposium on Intelligent Control IEEE International Symposium on Computer-Aided Control*, (Year not available). <https://doi.org/10.1109/cca.1996.558836>
  - [28] T. Azukuzawa, S. Yamamoto. Feasibility Study of a Passive Magnetic Bearing Using the Ring Shaped Permanent Magnets. *Performance Evaluation of Bearings*, (2012). <https://doi.org/10.5772/51347>
  - [29] R. Moser, J. Sandtner, H. Bleuler. Optimization of repulsive passive magnetic bearings. *IEEE Transactions on Magnetics*, 42(8), 2038-2042 (2006).

- <https://doi.org/10.1109/tmag.2005.861160>
- [30] E. A. Perigo, R. N. Faria, C. C. Motta. General Expressions for the Magnetic Flux Density Produced by Axially Magnetized Toroidal Permanent Magnets. *IEEE Transactions on Magnetics*, 43(10), 3826-3832 (2007). <https://doi.org/10.1109/tmag.2007.904708>
  - [31] R. Ravaut, G. Lemarquand, V. Lemarquand, C. Depollier. Analytical Calculation of the Magnetic Field Created by Permanent-Magnet Rings. *IEEE Transactions on Magnetics*, 44(8), 1982-1989 (2008). <https://doi.org/10.1109/tmag.2008.923096>
  - [32] R. Ravaut, G. Lemarquand. Comparison of the coulombian and amperian current models for calculating the magnetic field produced by radially magnetized arc-shaped permanent magnets. *Progress In Electromagnetics Research*, 95, 309-327 (2009). <https://doi.org/10.2528/pier09042105>
  - [33] R. Ravaut, G. Lemarquand, V. Lemarquand. Force and Stiffness of Passive Magnetic Bearings Using Permanent Magnets. Part 1: Axial Magnetization. *IEEE Transactions on Magnetics*, 45(7), 2996-3002 (2009). <https://doi.org/10.1109/tmag.2009.2016088>
  - [34] R. Ravaut, G. Lemarquand, V. Lemarquand. Force and Stiffness of Passive Magnetic Bearings Using Permanent Magnets. Part 2: Radial Magnetization. *IEEE Transactions on Magnetics*, 45(9), 3334-3342 (2009). <https://doi.org/10.1109/tmag.2009.2025315>
  - [35] R. Ravaut, G. Lemarquand, V. Lemarquand, C. Depollier. Permanent Magnet Couplings: Field and Torque Three-Dimensional Expressions Based on the Coulombian Model. *IEEE Transactions on Magnetics*, 45(4), 1950-1958 (2009). <https://doi.org/10.1109/tmag.2008.2010623>
  - [36] P. Samanta, H. Hirani. Magnetic Bearing Configurations: Theoretical and Experimental Studies. *IEEE Transactions on Magnetics*, 44(2), 292-300 (2008). <https://doi.org/10.1109/tmag.2007.912854>
  - [37] V. Lemarquand, G. Lemarquand. Passive Permanent Magnet Bearing for Rotating Shaft : Analytical Calculation. *Magnetic Bearings, Theory and Applications*, Page not available, (2010). <https://doi.org/10.5772/10085>
  - [38] S. I. Bekinal, T. R. Anil, S. Jana. Analysis of axially magnetized permanent magnet bearing characteristics. *Progress In Electromagnetics Research B*, 44, 327-343 (2012). <https://doi.org/10.2528/pierb12080910>
  - [39] S. I. Bekinal, T. R. Anil, S. Jana. Analysis of radial magnetized permanent magnet bearing characteristics. *Progress In Electromagnetics Research B*, 47, 87-105 (2013). <https://doi.org/10.2528/pierb12102005>
  - [40] S. I. Bekinal, T. R. Anil, S. Jana. Analysis of radial magnetized permanent magnet bearing characteristics for five degrees of freedom. *Progress In Electromagnetics Research B*, 52, 307-326 (2013). <https://doi.org/10.2528/pierb13032102>
  - [41] S. I. Bekinal et al. Permanent magnet thrust bearing: theoretical and experimental results. *Progress In Electromagnetics Research B*, 56, 269-287 (2013). <https://doi.org/10.2528/pierb13101602>

- [42] K. P. Lijesh, H. Hirani. Development of Analytical Equations for Design and Optimization of Axially Polarized Radial Passive Magnetic Bearing. *Journal of Tribology*, 137(1), (2014). <https://doi.org/10.1115/1.4028488>
- [43] J.L.G. Janssen, J.J.H. Paulides, E.A. Lomonova. Analytical Force and Stiffness Calculations for Magnetic Bearings and Vibration Isolation. in *Studies in Applied Electromagnetics and Mechanics*, vol. 34: Computer Field Models of Electromagnetic Devices, pp. 502-511, DOI: 10.3233/978-1-60750-604-1-502.
- [44] G. M. Wysin. Demagnetization Fields. Department of Physics. Kansas State University. Manhattan, KS 66506-2601, Written April 2012, Florianópolis, Brazil. <http://www.phys.ksu.edu/personal/wysin>.
- [45] R. Oser et al. Optimization of two-dimensional permanent magnet arrays for diamagnetic levitation. <https://pdfs.semanticscholar.org/ce20/4cb8b84bb981fa191770f69314baa461de79.pdf>, Accessed: Sep. 15, 2019.
- [46] R. K Nakum et al. An Experimental Comparison of Permanent Magnetic Bearing and Deep Groove Ball Bearing. *International Journal of Mechanical Engineering*, 4(6), 10-16 (2017). <https://doi.org/10.14445/23488360/ijme-v4i6p103>
- [47] T. Santra, D. Roy, S. Yamada. Calculation of force between two ring magnets using adaptive monte carlo technique with experimental verification. *Progress In Electromagnetics Research M*, 49, 181-193 (2016). <https://doi.org/10.2528/pierm16052101>
- [48] T. Santra, D. Roy, A. B. Choudhury. Calculation of passive magnetic force in a radial magnetic bearing using general division approach. *Progress In Electromagnetics Research M*, 54, 91-102 (2017). <https://doi.org/10.2528/pierm16120602>
- [49] T. Santra, D. Roy, A. B. Choudhury, S. Yamada. Experimental Verification of Force and Stiffness Between Two Ring Magnets Calculated by Monte Carlo Integration Technique. *Journal of The Institution of Engineers (India): Series B*, 100(2), 123-129 (2019). <https://doi.org/10.1007/s40031-019-00373-4>
- [50] P. B. Landecker, D. D. Villani, K. W. Yung. An Analytic Solution for the Torque Between Two Magnetic Dipoles. *Magnetic and Electrical Separation*, 10(1), 29-33 (1999). <https://doi.org/10.1155/1999/97902>
- [51] J. L. G. Janssen et al. Three-Dimensional Analytical Calculation of the Torque Between Permanent Magnets in Magnetic Bearings. *IEEE Transactions on Magnetics*, 46(6), 1748-1751 (2010). <https://doi.org/10.1109/tmag.2010.2043224>
- [52] J. R. M. van Dam et al. Analytical Surface Charge Method for Rotated Permanent Magnets: Boundary Element Method Comparison and Experimental Validation. *IEEE Transactions on Magnetics*, 52(7), 1-4 (2016). <https://doi.org/10.1109/tmag.2016.2517658>
- [53] M. Karmakar, S. Sarkar. Non dimensional analysis of axially polarized passive magnetic bearings. *SN Applied Sciences*, 2(5), (2020). <https://doi.org/10.1007/s42452-020-2809-x>

- [54] L. Zhang et al. Design, Analysis, and Experiment of Multiring Permanent Magnet Bearings by Means of Equally Distributed Sequences Based Monte Carlo Method. *Mathematical Problems in Engineering*, 2019, 1-17 (2019). <https://doi.org/10.1155/2019/4265698>
- [55] V. L. Van et al. A Magnetic Vector Potential Volume Integral Formulation for Nonlinear Magnetostatic Problems. *IEEE Transactions on Magnetics*, 52(3), 1-4 (2016). <https://doi.org/10.1109/tmag.2015.2490627>
- [56] M. Gyimesi, J.D. Lavers. Generalized potential formulation for 3-D magnetostatic problems. *IEEE Transactions on Magnetics*, 28(4), 1924-1929 (1992). <https://doi.org/10.1109/20.144749>
- [57] J. M. Camacho and V. Sosa. Alternative method to calculate the magnetic field of permanent magnets with azimuthal symmetry. *Rev. mex. fis.*, vol. 59, no. 1, pp. 8-17, 2013. <https://www.scienceopen.com/document?vid=f9ef0b8e-b6d2-4a2f-9d6f-abe2ebf1754a>
- [58] Roberto Bassani. Levitation of passive magnetic bearings and systems. *Tribology International*, 39(9), 963-970 (2006). <https://doi.org/10.1016/j.triboint.2005.10.003>
- [59] T. Azukizawa, S. Yamamoto, N. Matsuo. Feasibility Study of a Passive Magnetic Bearing Using the Ring Shaped Permanent Magnets. *IEEE Transactions on Magnetics*, 44(11), 4277-4280 (2008). <https://doi.org/10.1109/tmag.2008.2001490>
- [60] S. I. Bekinal, S. Jana. Generalized Three-Dimensional Mathematical Models for Force and Stiffness in Axially, Radially, and Perpendicularly Magnetized Passive Magnetic Bearings With “n” Number of Ring Pairs. *Journal of Tribology*, 138(3), (2016). <https://doi.org/10.1115/1.4032668>
- [61] S. I. Bekinal, M. Doddamani. Improvement in the design calculations of multi ring permanent magnet thrust bearing. *Progress In Electromagnetics Research M*, 94, 83-93 (2020). <https://doi.org/10.2528/pierm20052403>
- [62] R. Engel-Herbert, T. Hesjedal. Calculation of the magnetic stray field of a uniaxial magnetic domain. *Journal of Applied Physics*, 97(7), (2005). <https://doi.org/10.1063/1.1883308>
- [63] Y. S. Kim. Electromagnetic Force Calculation Method in Finite Element Analysis for Programmers. *Universal Journal of Electrical and Electronic Engineering*, 6(2B), 62-67 (2019). <https://doi.org/10.13189/ujeee.2019.061406>
- [64] T. Szolc, K. Falkowski, P. K. Mazurek. Design of a combined self-stabilizing electrodynamic passive magnetic bearing support for the automotive turbocharger rotor. *Journal of Vibration and Control*, 27(7-8), 815-826 (2020). <https://doi.org/10.1177/1077546320933486>
- [65] K. K. Nielsen et al. A Passive Permanent Magnetic Bearing With Increased Axial Lift Relative to Radial Stiffness. *IEEE Transactions on Magnetics*, 57(3), 1-8 (2021). <https://doi.org/10.1109/tmag.2020.3042957>
- [66] M. Lahdo, T. Strohla, S. Kovalev. Repulsive Magnetic Levitation Force Calculation For A High Precision 6-DoF Magnetic Levitation Positioning System. *IEEE Transactions on Magnetics*, 1-1, (2016).

<https://doi.org/10.1109/tmag.2016.2636124>

- [67] K. Kaphle, G. Karki, A. Panthi. Alternative Approach for the Calculation of Magnetic Field due to Magnet for Magnetic Field Visualization and Evaluation. *Journal of the Institute of Engineering*, 15(1), 150-160 (2020). <https://doi.org/10.3126/jie.v15i1.27724>
- [68] J. W. Beams and F. T. Holmes. Suspension of rotatable bodies. U.S. Patent US2256937A (1941).
- [69] W. Morales, R. Fusaro, A. Kascak. Permanent Magnetic Bearing for Spacecraft Applications. *Tribology Transactions*, 46(3), 460-464 (2003). <https://doi.org/10.1080/10402000308982651>
- [70] K. C. Lin et al. Magnetic bearing structure. U.S. Patent US6617732B1, (2003).
- [71] A. A. Hussien, S. Yamada, M. Iwahara, T. Okada, T. Ohji. Application of the repulsive-type magnetic bearing for manufacturing micromass measurement balance equipment. *IEEE Transactions on Magnetics*, 41(10), 3802-3804 (2005). <https://doi.org/10.1109/tmag.2005.854929>
- [72] T. Sugai, T. Inoue, Y. Ishida. Nonlinear vibration analysis of a rotating shaft supported by a repulsive magnetic bearing and vibration suppression using the axial control. 10th International Conference on Vibrations in Rotating Machinery, 427-439, (2012). <https://doi.org/10.1533/9780857094537.6.427>
- [73] G. Fillion, J. Ruel, M. Dubois. Reduced-Friction Passive Magnetic Bearing: Innovative Design and Novel Characterization Technique. *Machines*, 1(3), 98-115 (2013). <https://doi.org/10.3390/machines1030098>
- [74] V. G. Vijaykumar. Magnetic suspension system for automobiles. WIPO (PCT) Patent Application WO2017068601A1, (2017).
- [75] J. P. Yonnet et al. Stacked structures of passive magnetic bearings. *Journal of Applied Physics*, 70(10), 6633-6635 (1991). <https://doi.org/10.1063/1.349857>
- [76] C. Gutthedhar. Book Reviews: Dynamics of rotors and foundations Erwin Kramer Springer-Verlag Berlin, Heidelberg 1993, 383 pp, \$98.00 ISBN 0-387-55725-3. The Shock and Vibration Digest, 27(4), 17-17 (1995). <https://doi.org/10.1177/058310249502700408>
- [77] T. P. Indulekha, M. L. Joy, K. Prabhakaran Nair. Fluid flow and thermal analysis of a circular journal bearing. *Wärme- und Stoffübertragung*, 29(6), 367-371 (1994). <https://doi.org/10.1007/bf01878347>
- [78] H. Hirani et al. Rapid performance evaluation of journal bearings. *Tribology International*, 30(11), 825-834 (1997). [https://doi.org/10.1016/s0301-679x\(97\)00066-2](https://doi.org/10.1016/s0301-679x(97)00066-2)
- [79] T. V. V. L. N. Rao et al. An Analytical Approach to Evaluate Dynamic Coefficients and Nonlinear Transient Analysis of a Hydrodynamic Journal Bearing. *Tribology Transactions*, 43(1), 109-115 (2000). <https://doi.org/10.1080/10402000008982319>
- [80] J. T. Sawicki, T. V. V. L. N. Rao. Nonlinear Prediction of Rotordynamic Coefficients For a Hydrodynamic Journal Bearing. *Tribology Transactions*, 44(3), 367-374 (2001). <https://doi.org/10.1080/10402000108982469>
- [81] A. E. Fortier, R. F. Salant. Numerical Analysis of a Journal Bearing With a

- Heterogeneous Slip/No-Slip Surface. *Journal of Tribology*, 127(4), 820-825 (2005). <https://doi.org/10.1115/1.2033897>
- [82] S.X. Zhao et al. An experimental study of nonlinear oil-film forces of a journal bearing. *Journal of Sound and Vibration*, 287(4-5), 827-843 (2005). <https://doi.org/10.1016/j.jsv.2004.11.034>
- [83] V. Meruane, R. Pascual. Identification of nonlinear dynamic coefficients in plain journal bearings. *Tribology International*, 41(8), 743-754 (2008). <https://doi.org/10.1016/j.triboint.2008.01.002>
- [84] Y L Wang et al. Approximate analytical model for fluid film force of finite length plain journal bearing. *Proceedings of the Institution of Mechanical Engineers, Part C: Journal of Mechanical Engineering Science*, 226(5), 1345-1355 (2011). <https://doi.org/10.1177/0954406211418302>
- [85] J. R. Lin et al. Nonlinear stability boundary of journal bearing systems operating with non-Newtonian couple stress fluids. *Tribology International*, 71, 114-119 (2014). <https://doi.org/10.1016/j.triboint.2013.10.010>
- [86] M. T. C. Faria. On the Hydrodynamic Long Journal Bearing Theory. In *Proceedings of the World Congress on Engineering 2014*, vol. II, WCE 2014, London, U.K. ISBN: 978-988-19253-5-0, ISSN: 2078-0958 (Print); ISSN: 2078-0966 (Online).
- [87] Y. Zhang et al. An approximate solution of oil film forces of turbulent finite length journal bearing. *Tribology International*, 74, 110-120 (2014). <https://doi.org/10.1016/j.triboint.2014.02.015>
- [88] H. Feng, S. Jiang. Dynamics of a motorized spindle supported on water-lubricated bearings. *Proceedings of the Institution of Mechanical Engineers, Part C: Journal of Mechanical Engineering Science*, 231(3), 459-472 (2016). <https://doi.org/10.1177/0954406215616653>
- [89] R. Z. Gong et al. Analytical solution of Reynolds equation under dynamic conditions. *Proceedings of the Institution of Mechanical Engineers, Part J: Journal of Engineering Tribology*, 230(4), 416-427 (2015). <https://doi.org/10.1177/1350650115604654>
- [90] M. Trachsel, R. Pittini, J. Dual. Friction and 2D position measurements in small journal bearings. *Tribology International*, 102, 555-560 (2016). <https://doi.org/10.1016/j.triboint.2016.06.006>
- [91] I. F. Santos, P. K. Svendsen. Noninvasive Parameter Identification in Rotordynamics Via Fluid Film Bearings—Linking Active Lubrication and Operational Modal Analysis. *Journal of Engineering for Gas Turbines and Power*, 139(6), (2017). <https://doi.org/10.1115/1.4035447>
- [92] J. Wang et al. Mathematical model and algorithm of interface singular stress field of oil-film bearing. *Tribology International*, 116, 351-361 (2017). <https://doi.org/10.1016/j.triboint.2017.07.026>
- [93] Š. Dyk et al. Dynamic coefficients and stability analysis of finite-length journal bearings considering approximate analytical solutions of the Reynolds equation. *Tribology International*, 130, 229-244 (2019). <https://doi.org/10.1016/j.triboint.2018.09.011>

- [94] T. H. Machado, D. S. Alves, K. L. Cavalca. Discussion about nonlinear boundaries for hydrodynamic forces in journal bearing. *Nonlinear Dynamics*, 92(4), 2005-2022 (2018). <https://doi.org/10.1007/s11071-018-4177-2>
- [95] M. H. Hekmat, G. A. Biukpour. Numerical study of the oil whirl phenomenon in a hydrodynamic journal bearing. *Journal of the Brazilian Society of Mechanical Sciences and Engineering*, 41(5), (2019). <https://doi.org/10.1007/s40430-019-1724-9>
- [96] A. Singh, T. C. Gupta. Bifurcation analysis of turbocharger flexible rotor system supported on fluid film bearings. *AIP Conference Proceedings*, Page not available, (2020). <https://doi.org/10.1063/5.0001252>
- [97] C. Alberto et al. Experimental and Numerical Investigation about Small Clearance Journal Bearings under Static Load Conditions. *Advances in Tribology*, 2020, 1-13 (2020). <https://doi.org/10.1155/2020/8844879>
- [98] F. Concli. Journal Bearing: An Integrated CFD-Analytical Approach for the Estimation of the Trajectory and Equilibrium Position. *Applied Sciences*, 10(23), 8573 (2020). <https://doi.org/10.3390/app10238573>
- [99] N. Nikolic et al. An Analytical Method for the Determination of Temperature Distribution in Short Journal Bearing Oil Film. *Symmetry*, 12(4), 539 (2020). <https://doi.org/10.3390/sym12040539>
- [100] T. Qingchang, L. Wei, X. Xuejun. Investigation on a magnetic-hydrodynamic hybrid thrust bearing, *Tribology Letters*, 12(1), 61-66 (2002). <https://doi.org/10.1023/a:1013927606459>
- [101] H. Hirani, P. Samanta. Performance Evaluation of Magnetohydrodynamic Bearing. *World Tribology Congress III, Volume 2*, Page not available, (2005). <https://doi.org/10.1115/wtc2005-63608>
- [102] H Hirani, P Samanta. Hybrid (hydrodynamic + permanent magnetic) journal bearings. *Proceedings of the Institution of Mechanical Engineers, Part J: Journal of Engineering Tribology*, 221(8), 881-891 (2007). <https://doi.org/10.1243/13506501jet282>
- [103] K.P. Lijesh, H. Hirani, P. K. Samanta. Theoretical and Experimental Study for Hybrid Journal Bearing. *International Journal of Scientific and Engineering Research*, 6(2), 133-139 (2015). <https://doi.org/10.14299/ijser.2015.02.002>
- [104] M.G. Farmakopoulos, P.G. Nikolakopoulos, C.A. Papadopoulos. Design of an active hydromagnetic journal bearing. *Proceedings of the Institution of Mechanical Engineers, Part J: Journal of Engineering Tribology*, 227(7), 673-694 (2012). <https://doi.org/10.1177/1350650112466164>
- [105] R. Goraj. Theoretical study on a novel electromagnetically supported hydrodynamic bearing under static loads. *Tribology International*, 119, 775-785 (2018). <https://doi.org/10.1016/j.triboint.2017.09.021>
- [106] J. Fang, C. Wang, T. Wen. Design and Optimization of a Radial Hybrid Magnetic Bearing With Separate Poles for Magnetically Suspended Inertially Stabilized Platform. *IEEE Transactions on Magnetics*, 50(5), 1-11 (2014). <https://doi.org/10.1109/tmag.2013.2293482>
- [107] X. Liu et al. Design and Static Performance Analysis of a Novel Axial Hybrid

- Magnetic Bearing. *IEEE Transactions on Magnetics*, 50(11), 1-4 (2014).  
<https://doi.org/10.1109/tmag.2014.2327165>
- [108] S. Jinji et al. A novel integrated 4-DOF radial hybrid magnetic bearing for MSCMG. *Journal of Magnetism and Magnetic Materials*, 421, 86-97 (2017).  
<https://doi.org/10.1016/j.jmmm.2016.07.070>
- [109] T. Zhang et al. Modeling and Performance Analysis on Slice Hybrid Magnetic Bearing with Two Radial Air-gaps. 2018 IEEE International Conference on Applied Superconductivity and Electromagnetic Devices (ASEMD), (2018).  
<https://doi.org/10.1109/asemd.2018.8558918>
- [110] M. Stoiber et al. A Passive Magnetically and Hydrodynamically Suspended Rotary Blood Pump. *Artificial Organs*, 33(3), 250-257 (2009).  
<https://doi.org/10.1111/j.1525-1594.2009.00715.x>
- [111] R. Villaverde. Base isolation with sliding hydromagnetic bearings: concept and feasibility study. *Structure and Infrastructure Engineering*, 13(6), 709-721 (2016). <https://doi.org/10.1080/15732479.2016.1187634>
- [112] E. Krämer. *Dynamics of Rotors and Foundations*. illustrated ed. Springer Science & Business Media, 2013.
- [113] P. Huang. *Numerical Calculation of Lubrication: Methods and Programs*. John Wiley & Sons Inc, (2013). ISBN: 978-1-118-45122-9.
- [114] M. Karmakar, S. Tudu, S. Sarkar, S. C. Mondal. Comparison of errors in calculating the journal force of a short cylindrical oil film bearing. *Contemporary issues in computing*, (2020).  
<https://doi.org/10.26480/cic.01.2020.59.63>
- [115] S. Earnshaw. On the nature of the molecular forces which regulate the constitution of the lumiferous ether. *Trans. Camb. Philos. Soc.*, vol. 7, pp. 97–112, 1842.
- [116] E. Krämer. *Dynamics of Rotors and Foundations*. Journal not available, (1993).  
<https://doi.org/10.1007/978-3-662-02798-1>
- [117] M. Karmakar, S. Sarkar. Semi-Analytical Finite Element Approach for 6-DOF Characterizations of PMB Load. *IEEE Transactions on Magnetics*, 58(7), 1-10 (2022). <https://doi.org/10.1109/tmag.2022.3174449>
- [118] T. L. Schmitz, K. S. Smith. *Mechanical Vibrations*. Journal not available, (2012). <https://doi.org/10.1007/978-1-4614-0460-6>



# Appendix A

## A.1 Bearing force derivation

Relationship found from equation (27) and equation (29)

$$F_b = \int_0^{2\pi R} \int_0^L P dx dz \text{ where } x = R\theta, z = \bar{z}L$$

$$F_b = \int_0^{2\pi} \int_0^1 P R L d\theta d\bar{z}$$

There are other approach using uniform scaling just considering  $x = R\theta, z = R\bar{z}$

Hence, the equation (27) becomes,

$$F_b = \int_0^{2\pi} \int_0^{L/R} P R^2 d\theta d\bar{z}$$

$$\text{Or, } F_b = \int_0^{2\pi} \int_0^{2L/2R} P R^2 d\theta d\bar{z}$$

$$\text{Or, } F_b = P_a R^2 B_n \int_0^{2\pi} \int_0^{2L_d} \bar{P} d\theta d\bar{z} \text{ where, } L_d = \frac{L}{2R}, \bar{P} = \frac{P}{P_a B_n}, B_n = \frac{6\mu\omega R^2}{P_a \delta^2}$$

$$F_b = F_{bcoef} \bar{F}_{b0} \text{ where, coefficient force, } F_{bcoef} = P_a R^2 B_n \text{ and dimensionless force function, } \bar{F}_{b0} = \int_0^{2\pi} \int_0^{2L_d} \bar{P} d\theta d\bar{z}$$

$$\text{Now, } \bar{F}_b = \frac{F_b}{F_{cb}} \text{ where, } F_{cb} \text{ found from equation (100)}$$

$$\bar{F}_b = \frac{F_{bcoef} \bar{F}_{b0}}{F_{cb}}$$

$$\bar{F}_b = \frac{1.5 \times \bar{F}_{b0}}{L_d^3}$$

## A.2 Sommerfeld number relationship with journal bearing force

Relationship found from equation (25) and equation (100)

$$S = \left(\frac{1}{2\pi}\right) \times \frac{r^2}{(R-r)^2} \times \frac{\mu L \omega D}{F} \text{ and } F_{cb} = \frac{\mu \Omega R_b L^3}{2\delta^2}$$

If  $\bar{F}_b$  is non-dimensional force of fluid film journal bearing, following steps can be found in context of the above equations (25) and (100) as

$$F \text{ or } F_b = F_{cb} \times \bar{F}_b$$

$$S = \left(\frac{1}{2\pi}\right) \times \frac{r^2}{\delta^2} \times \frac{\mu L \omega D}{F_{cb} \times \bar{F}_b} \text{ as } \delta = R - r$$

$$S = \left(\frac{1}{2\pi}\right) \times \frac{r^2}{\delta^2} \times \frac{\mu L \omega D}{\frac{\mu \Omega R_b L^3}{2\delta^2} \times \bar{F}_b}$$

$$S = \frac{1}{2\pi L_d^2 \bar{F}_b} \text{ as mentioned in equation (30)}$$

$$\text{Or, } S = \frac{L_d}{3\pi \bar{F}_{b0}} \text{ as substituting } \bar{F}_b = \frac{1.5 \times \bar{F}_{b0}}{L_d^3} \text{ from Appendix A.1}$$



## Research Article

# Non dimensional analysis of axially polarized passive magnetic bearings



Mintu Karmakar<sup>1</sup>  · Susenjit Sarkar<sup>1</sup>

Received: 9 October 2019 / Accepted: 22 April 2020 / Published online: 29 April 2020  
© Springer Nature Switzerland AG 2020

## Abstract

Ranges of investigation on passive magnetic bearing exist where radial and axial forces and variations of a few coefficients of radial and axial stiffnesses are shown for a particular set of chosen parameters and dimensions. The paper presents a non-dimensional approach for the same with additional parameters like all coefficients of stiffnesses and natural frequency. The model is considered for static analysis of axially polarised ring shaped magnets for both stator and rotor part in three degrees of freedom with three linear translations in 3D Cartesian coordinate system. The significance of this non-dimensional method is more generalised to the designer where boundary parameters like maximum force on the rotor of passive magnetic bearing, natural frequency, etc. can be easily estimated by simple conversion without doing separate numerical simulation for different parameters every time. The analysis of additional parameters like non-dimensional natural frequency can be the input for non-dimensional dynamic analysis. This paper also provides a way for maximization of radial force with the optimized solution of physical dimensions of passive magnetic bearing as inner radius of stator and outer radius of rotor magnet while keeping others as input parameters. The proposed model is validated with data available for radial and axial forces as well as for radial and axial stiffnesses that found in existing literature for similar kind of problem.

**Keywords** Non-dimensional · Passive magnetic bearing · Radial force maximization · Natural frequency · Axially polarised

## Abbreviations

$F_{sr}$	Magnetic force between stator and rotor (N)	$Br_1$	Residual magnetism of rotor magnetic material (T)
$\mu_0$	Absolute permeability $\left(4\pi \times 10^{-7} \frac{N}{A^2} \text{ or } \frac{H}{m} \text{ or } \frac{Tm}{A}\right)$	$Br_2$	Residual magnetism of stator magnetic material (T)
$\pi$	3.1415926535 (Non-dimensional)	$r_1$	Radial distance of rotor small elemental area $dS_r$ from rotor axis (m)
$q_s$	Magnetic pole strength of stator magnet (Wb or Am)	$r_2$	Radial distance of stator small elemental area $dS_s$ from stator axis (m)
$q_r$	Magnetic pole strength of rotor magnet (Wb or Am)	$\alpha$	Angular displacement of stator small elemental area $dS_s$ about stator axis measured from x axis (radian)
$r_{sr}$	Distance between stator and rotor magnetic pole (m)	$\beta$	Angular displacement of rotor small elemental area $dS_r$ about rotor axis measured from x axis (radian)
$\sigma_s$	Stator magnetic surface charge density (T)		
$\sigma_r$	Rotor magnetic surface charge density (T)		
$S_s$	Stator magnetic pole surface area per pole ( $m^2$ )		
$S_r$	Rotor magnetic pole surface area per pole ( $m^2$ )		

✉ Mintu Karmakar, mintukarmakar@gmail.com; Susenjit Sarkar, susenjit\_s@rediffmail.com | <sup>1</sup>Department of Mechanical Engineering, Jadavpur University, Kolkata, West Bengal 700032, India.



SN Applied Sciences (2020) 2:987 | <https://doi.org/10.1007/s42452-020-2809-x>

SN Applied Sciences  
A SPRINGER NATURE journal



# Semi-Analytical Finite Element Approach for 6-DOF Characterizations of PMB Load

M. Karmakar<sup>1</sup> and S. Sarkar<sup>2</sup>

Department of Mechanical Engineering, Jadavpur University, Kolkata, West Bengal 700032, India

A typically new semi-analytical finite element approach has been used to calculate the force and moment of permanent magnet bearing (PMB) in this article. PMB stator and rotor consist of ring-type cylindrical magnets having an axial magnetization. This article focuses on the characterization of magnetic moment, stiffness matrix, model validation, and comparisons of the moment with other simulating software. This article also explains how angular stiffness or resisting magnetic moment of PMB improves with the change of rotor magnet length and positional shift of the rotor.

**Index Terms**—Angular stiffness, magnetic moment, permanent magnet bearing (PMB), semi-analytic finite element, six degrees of freedom (6-DOF).

## I. INTRODUCTION

THE bearing is one of the essential machine elements for supporting rotary parts. A magnetic bearing is beneficial not only for its contactless operation but for its wide range of operational rotating speeds. Magnetic bearings used in industry are mostly active control magnetic bearings. Passive magnetic bearing using ferromagnetic material has less application due to failing of stability together in all degrees of freedom. Earnshaw theorem [1] always censures its stability simultaneously in all translation axes. Hence, passive magnetic bearing is generally used with other supporting systems or electromagnets [2]–[12]. Some permanent magnet bearing (PMB) designs with such support also got patents [2], [4], [5], [12]. Various optimization of the PMB design requires a faster and more accurate calculation of magnetic load like force, moment, stiffness, etc. Past researchers have done numerous works on load calculation considering various methods and models or different combinations of both. These are mainly analytical integral [13]–[22], statistical Riemann sum and Monte Carlo integration [23]–[25], general division approach [26], magnetic scalar and vector potential volume integral [27], [28], magnetic dipole method [7], [13], [14], Taylor's expansion [13], power series expansion [29], surface current model [30]–[32], surface charge model or Coulomb model [31], [33]–[37], Gauss and Maxwell stress tensor model [38]–[41], finite element method (FEM) [39], semi-analytical [42]–[45], and considering cuboid structure [19], [38], [45], [46], etc. Most of the above-mentioned approaches have validations among themselves. Some of these papers also have shown practical validation of force only.

There are very few articles on the theoretical moment calculation of ring-shaped axially magnetized PMB. Also, no validation plot of PMB moment with the experimental data or other simulation models is found in the literature. However, partly similar work [43] is carried out by Bekinal *et al.* to

Manuscript received April 3, 2022; revised April 29, 2022; accepted May 1, 2022. Date of publication May 11, 2022; date of current version June 29, 2022. Corresponding author: M. Karmakar (e-mail: mintukarmakar@gmail.com).

Color versions of one or more figures in this article are available at <https://doi.org/10.1109/TMAG.2022.3174449>.

Digital Object Identifier 10.1109/TMAG.2022.3174449

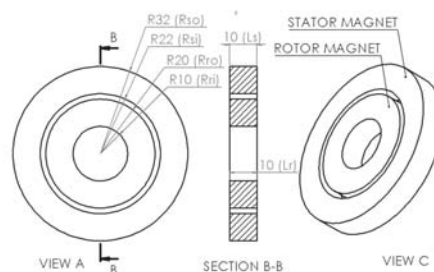


Fig. 1. Schematic of PMB rotor and stator magnet.

characterize magnetic moments without showing validation or comparing results. Ansys Maxwell software is used in this study to validate the model for calculating the PMB magnetic moment experienced at the rotor part of the magnetic bearing. The article presents an innovative semi-analytical finite element approach to estimate the force and moment for a single pair of axially magnetized ring-type PMB. A sensitivity study with this method and algorithm handles the accuracy and computation performance of the calculation. Further, a designer can adopt any optimization algorithm in the following explained model of the repulsive type PMB to characterize according to application requirements. Moreover, scripting of the proposed algorithm allows to couple with any physical interface around the spatial boundary of the bearing so that analysis may be carried out to study stability in the presence of active or passive interaction due to viscous damping.

All six degrees of freedom (6-DOF) are considered to extend [22]. Here, the complete 6-DOF means three orthogonal axes  $X$ ,  $Y$ , and  $Z$  translation orientations and three tilting orientations about those three axes.

## II. DETAILS OF THE PROPOSED MODEL

### A. Schematic of Passive Magnetic Bearing

A single pair of cylindrical permanent magnets (see Fig. 1) is considered for the analysis. Both magnets of the stator





ISBN: 978-1-948012-16-4

## Contemporary Issues in Computing (CIC)

DOI: <http://doi.org/10.26480/cic.01.2020.59.63>

# COMPARISON OF ERRORS IN CALCULATING THE JOURNAL FORCE OF A SHORT CYLINDRICAL OIL FILM BEARING

Mintu Karmakar, Suplal Tudu, Susenjit Sarkar\*, Samar Chandra Mondal

Department of Mechanical Engineering, Jadavpur University, Kolkata -700032, West Bengal, INDIA

\*Corresponding Author e-mail: [susenjit\\_s@rediffmail.com](mailto:susenjit_s@rediffmail.com)

This is an open access article distributed under the Creative Commons Attribution License CC BY 4.0, which permits unrestricted use, distribution, and reproduction in any medium, provided the original work is properly cited.

## ARTICLE DETAILS

### Article History:

Received 26 October 2020  
Accepted 27 November 2020  
Available online 03 December 2020

## ABSTRACT

In the present paper, a new model is developed for analysis of the errors for calculating journal force of a short cylindrical oil film journal bearing. The pressure distribution in oil film short journal bearing has been determined with the help of Reynold's equation. Fluid is assumed incompressible and steady. In this paper three different computation methods FDM conventional, FDM matrix formation and FEM using MATLAB PDE solver are investigated for calculating journal force. From the results it has been observed that the absolute error percentage for force calculation in short cylindrical bearing is minimum by using the FEM MATLAB PDE solver compared to other two methods. Also a vivid statistical analysis is carried with the help of ANOVA tool to understand the dependency of method, step or element size and eccentricity on computational time and errors.

## KEYWORDS

FDM, sparse matrix, FEM, MATLAB PDE, error, computational cost, ANOVA.

## 1. INTRODUCTION

Kramer presented the derivation of classical Reynolds equation in a very clear and distinct manner (Kramer, 1993). The short bearing approximation for solving Reynolds equation was clearly reported with the formulation and calculation of damping and stiffness coefficients for various types of short cylindrical bearings. The procedure to calculate the static equilibrium position was also clearly mentioned. The Somerfield's solutions and boundary conditions were also investigated. The empirical relation between the attitude angle and the eccentricity was studied. Sahoo presented the derivation of Navier stokes equation and reduced it to Reynolds equation using certain assumptions (Sahoo, 2005). Different types of bearings such as hydrostatic bearing, squeeze film bearing, elasto hydrodynamic bearing were studied with different boundary conditions. By finite difference method Machado and Calva presented the solution of Reynolds equation for pressure field using finite difference method (Machado and Calva, 2009). They reported pressure distribution for different types of bearings such as cylindrical bearing, elliptical bearing, 3 lobed bearing etc. They also found the locus of shaft journal center in the bearing and the dynamic coefficients in different types of bearings. Squeeze effects were also investigated in the above all bearings. Faria presented the application of finite element method in the development of computer procedures for hydrodynamic elliptical journal bearing (Faria, 2015). The finite element formulation for the classical Reynolds equation was made and the pressure field was calculated. The method used here for

the calculation of load capacity and the stability formulation were a bit unique. The procedure for finding the static equilibrium position was not clearly stated. How discretization affects the solution of Reynolds equation was also analyzed which was called mesh sensitivity analysis. The results obtained for finite element method was validated with other researchers. In the last step performance analysis of elliptical journal bearing was made. Rowe and Chang used finite difference method for calculating pressure field from Reynolds equation based on non-dimensional linearized dynamic coefficients (Rowe and Chong, 1986). Two techniques, Finite difference and perturbation technique were used for prediction of dynamic coefficients. This paper gave a clear picture of dynamic coefficients and detailed flowchart of the same, but the determination of static equilibrium position was not clearly mentioned.

From different literatures stated above the basic idea about the solution of the Reynolds equation was gained. Different numerical methods like FDM, FEM, and analytical methods were understood. It was evident from the literature that for finding pressure distribution, solving of the Reynolds equation is necessary.

A rotor system is always supported by bearings that may be sliding or ball or roller bearing. To study the pressure and force characteristics, a general idea about the bearings is of utmost importance. In most of the heavy duty works the sliding bearings are used of which fluid film bearing is of the most important category.

Quick Response Code	This paper was presented at	Access this article online	
	International Conference on Contemporary Issues in Computing (ICIC-2020) - Virtual IETE Sector V, Salt Lake, Kolkata From 25th-26th July 2020	Website: <a href="http://www.intelcomp-design.com">www.intelcomp-design.com</a>	DOI: 10.26480/cic.01.2020.59.63

Cite The Article: Mintu Karmakar, Suplal Tudu, Susenjit Sarkar, Samar Chandra Mondal (2020). Comparison of Errors in Calculating The Journal Force of A Short Cylindrical Oil Film Bearing. *Topics in Intelligent Computing and Industry Design*, 2(1): 59-63.

Mintu Karmakar  
19.03.2024